Summer 8-15-2017

Mechanobiology of Epithelial Clusters in ECMs of Diverse Mechanical Properties

Samila Nasrollahi
Washington University in St. Louis

WASHINGTON UNIVERSITY IN ST. LOUIS

School of Engineering and Applied Science

Department of Mechanical Engineering & Materials Science

Dissertation Examination Committee:
Dr. Amit Pathak, Chair
Dr. Philip Bayly
Dr. Elliot Elson
Dr. Spencer Lake
Dr. Lori Setton

Mechanobiology of Epithelial Clusters in ECMs of Diverse Mechanical Properties

by

Samila Nasrollahi

A dissertation presented to
The Graduate School
of Washington University in
partial fulfillment of the
requirements for the degree
of Doctor of Philosophy

August 2017
Saint Louis, Missouri

Contents

List of Figures

Acknowledgments

First and foremost I want to thank my advisor Dr. Amit Pathak. It has been an honor to be his first Ph.D. student. I appreciate all his contributions of time, ideas, and funding to make my Ph.D. experience productive and enjoyable. His dedication and enthusiasm for doing a good science were inspiring for me, even during the hard times of my Ph.D. pursuit. Amit has supported me not only by providing a research mentorship over the past four years but also academically and emotionally through the rough road to finish my Ph.D. I could not have imagined having a better and friendlier advisor and mentor for my Ph.D. I would also like to thank my thesis committee members: Dr. Philip Bayly, Dr. Lori Setton, Dr. Eliot Elson, Dr. Spence lake. for their encouragement, insightful comments, and great questions.

Lastly, I would like to thank my lovely family and especially my parents Susan Naghdi and Samad Nasrollahi for all their love and encouragement throughout my life. Their support has been unconditional all these years; they have given up many things so that I can pursue my education in the US; even from the long-distance their continuous support and positive energy inspired me to move forward along the way of my Ph.D. journey. And most of all for the love of my life Mehdi who can't be more patient, supportive, and encouraging throughout the ups and downs of this enjoyable, and yet rough journey. His endless passion for learning new things and dedication to science has always been inspiring for me. I am impatiently

looking forward to the next chapters of our lives together. I thank my fellow lab mates in cellular mechanobiology laboratory for the stimulating discussions and comments and for all the fun we have had in the last four years.

Samila Nasrollahi

Washington University in Saint Louis

August 2017

ABSTRACT OF THE DISSERTATION

Mechanobiology of Epithelial Clusters in ECMs of Diverse Mechanical Properties

by

Samila Nasrollahi

Doctor of Philosophy in Mechanical Engineering

Washington University in St. Louis, August 2017

Research Advisor: Professor Amit Pathak

Cell clusters reside in complex extracellular matrices (ECMs) of varying mechanical properties. Epithelial cells sense and translate the mechanical cues presented by the surrounding ECM into biochemical signals through a process called 'mechanotransduction', which controls fundamental aspects of disease and development. During the course of metastasis, mechanical changes in the tumor microenvironment can lead to declustering of epithelial cells through a process called epithelial-to-mesenchymal transition (EMT). Throughout different steps of metastasis, escaped epithelial clusters encounter heterogeneous tissues of varying mechanical properties that ultimately influence their behavior in distant locations within the body. This dissertation investigates the mechanobiology of epithelial clusters inside mechanically heterogeneous tissue microenvironments. Chapter 1 provides an introduction for the mechanobiology of epithelial clusters and describes how mechanical properties of the microenvironment mediates behavior of epithelial cells. Chapter 2 addresses the mechano-regulated epithelial to mesenchymal transition inside matrices of varying stiffness and confinement. Growing evidence suggests that high extracellular matrix (ECM) stiffness induces

EMT. Yet, very little is known about how various geometrical parameters of the ECM might influence EMT. To this end, we develop polyacrylamide (PA)-microchannels based matrix platform to culture mammary epithelial cell clusters in ECMs of tunable stiffness and confinement. Our results demonstrate that ECM confinement alone is able to induce EMT in epithelial clusters surrounded by a soft matrix, which otherwise protects against EMT in unconfined environments. Also, we demonstrate that stiffness- and confinement-induced EMT work through cell-matrix adhesions and cytoskeletal polarization, respectively. In chapter 3, we examined the combinatorial effect of phenotypic heterogeneity and matrix heterogeneity in determining the overall migration of the migrating clusters and the motion of individual cells in the cluster. These findings may provide insights into the effect of cellular heterogeneity on the epithelial dynamics during the early stage of cancer progression. In chapter 4, we examined the collective migration of epithelial cells across physically diverse matrices. Although the influence of matrix stiffness on cell migration is well-recognized, it remains unknown whether these matrix-dependent cellular features persist even after cells move to a new microenvironment. We have discovered that epithelial cells primed on a stiff matrix migrate faster, generate higher actomyosin expression, and retain nuclear YAP even after arriving on a soft matrix, as compared to their control behavior on a homogeneously soft matrix. Our results have uncovered a mechanical memory of past matrix stiffness in collective migration of normal and cancer epithelial cells. The depletion of YAP dramatically reduces this memory-dependent migration. These revelations imply that, during metastasis, changes in tumor microenvironment stiffness may influence the future invasion of escaping tumor cells.

Chapter 1

Introduction: Mechanobiology of epithelial clusters in heterogeneous matrices

Over the past decade, the topic of cellular mechanobiology has seen a surge in activity, particularly in the area of cellular mechano-response to a range of matrix parameters. Cell behaviors, such as migration, differentiation, proliferation, and fate decisions, are now known to depend on matrix stiffness. In fact, cells are turning out to be such exquisite sensors of matrix stiffness that changes of the order of tens of kilo-pascals can entirely shift their response. For example, the biphasic dependence of cell migration speed on matrix stiffness has shown that cells only migrate fast in an intermediate regime of stiffness. However, in most of these studies, the cell behavior is studied in homogeneous matrix environments, either 2D or 3D, either stiff or soft, all of which are strikingly different from what the cells experience in reality. This lack of heterogeneity in existing systems become particularly important given

that cells are turning out to be such sophisticated and delicate sensors of their environment. Thus, slight changes in their surroundings, in terms of topography, dimensionality, and stiffness, may fundamentally alter their macroscopic behavior as well as the gene expression profile. There is a dire need to capture these cell-matrix interactions. Through a collection of projects, this thesis attempts to make novel contributions in understanding how epithelial cells, singly or collectively, respond to spatially heterogeneous matrix stiffness, confinement, and dimensionality.

Epithelial cell clusters reside in complex extracellular matrices (ECMs) of varying mechanical properties. Through mechanotransduction, epithelial cells sense and translate the mechanical cues presented by the surrounding ECM into biochemical signals, which control fundamental aspects of cell behavior, including migration and clustering. During metastasis, mechanical changes in the tumor microenvironment lead to declustering of epithelial cells and dissolution of cell-cell contacts, which triggers an epithelial-to-mesenchymal transition (EMT) in clustered cells. The EMT has been implicated in progression of various types of cancers. Moreover, the occurrence of EMT allows benign cancer cells to acquire a capacity to infiltrate into surrounding tissues and ultimately metastasize to distant locations within the body. After breaking away from the primary tumor, escaped cell clusters encounter heterogeneous tissues and adapt to microenvironments of varying mechanical properties that ultimately influence their behavior throughout their invasion trajectory in distant tissue locations.

The stiffening of the tumor microenvironment has been implicated in this EMT-enabled dissemination of tumor cells. However, it remains unclear how topography and confinement of the matrix might influence EMT. This represents an important gap in knowledge given that tissue environments often vary in topography and confinement without significant variation in stiffness. To this aim, we fabricated an in vitro platform that mimics the growth of epithelial

clusters in microenvironments of varying stiffness and topography. In this system, we used photolithography techniques to fabricate silicon-based scaffolds of defined geometry, where channel width is prescribed in the mask design. We polymerized PA solutions of specified monomer-cross linker ratios against these masters, which yielded PA substrates of defined stiffness and topography. Epithelial colony is cultured inside the central chamber surrounded by channels of various sizes. Subsequently, we study EMT for epithelial clusters emanate from the initial colony and trapped inside the channels of varying elasticity and topography. Using this platform, we report a previously unidentified mechanism of EMT induction due to ECM confinement. We found that E-cad membrane localization of MCF10A cells inside soft channels decreased with channel width, and vimentin expression increased in more confined ECMS, which indicated a rise in EMT due to confinement. Our results demonstrate that ECM confinement alone can induce EMT in epithelial clusters surrounded by a soft matrix, which otherwise protects against EMT in unconfined environments. Further, we demonstrate that stiffness-induced and confinement-induced EMT work through cell-matrix adhesions and cytoskeletal polarization, respectively. These findings highlight that both the structure and the stiffness of the ECM can independently regulate EMT, which brings a fresh perspective to the existing paradigm of matrix stiffness-dependent dissemination and invasion of tumor cells.

After undergoing EMT, cancer cells are expected to become motile and invade the surrounding matrix either singly or collectively. Although single cell motility has been extensively studied, there is little known about collective migration within topographically controlled surfaces. Presented experimental framework of epithelial clusters in ECMs of defined stiffness and topography could serve as a novel platform to understand the relative contributions of micro-scale ECM properties in dictating various modes of cell motility.

Throughout their migration trajectory, cells adapt to tissue microenvironments of differing mechanical properties. Although the influence of immediate matrix stiffness on cellular mechanosensitivity and motility are now well-recognized, it remains unknown whether these matrix-dependent cellular features persist even after cells move to a new microenvironment. This is mainly due to the absence of matrix platforms that allow the measurement of collective migration of epithelial cells across contiguous ECMs of diverse mechanical properties. In this project, we have recently begun to address this challenge by developing a modular polyacrylamide hydrogel platform comprising contiguous primary and secondary ECM regions of independently defined stiffness, in which the stiffness of each region can be controlled by changing the PA composition. Using this platform, we interrogate whether preconditioning of epithelial cells by a given matrix stiffness influences their future collective migration on a different matrix – a property we refer to as the 'mechanical memory' of migratory cells. To precondition cells on a primary matrix and track their collective migration onto an adjoining, contiguous secondary matrix of dissimilar stiffness, we develop a modular polyacrylamide (mPA) substrate through step-by-step polymerization of different PA compositions. We report that both normal (MCF10A) and cancer (MCF7 and A431) epithelial cells preconditioned on a stiff primary matrix migrate faster and display higher actomyosin expression even after arriving onto a soft secondary matrix, as compared to their control behavior on a homogeneously soft matrix. We show that nuclear localization of Yes-associated-protein (YAP) due to preconditioning on a stiff primary matrix persists even after cells migrate to a soft secondary matrix. The depletion of YAP dramatically reduces the dependence of collective cell migration on past ECM stiffness. Thus, mechanosensitive YAP activity is a key mechanism for storing mechanical memory in migratory epithelial cells. Our results present a previously unidentified regulation of mechanosensitive collective cell migration by past matrix stiffness, in which mechanical memory depends on YAP activity.

Scope of the dissertation. The primary goal of this dissertation is to improve our understanding of the mechanobiology of epithelial clusters in diverse microenvironments and to dissect the role of different ECM parameters including topography and stiffness in dictating different single collective phenotypes of epithelial cells. In particular, various modes of scattering and migration of epithelial cells in tunable engineered matrix platforms are studied.

Chapter 2 addresses the roles of ECM stiffness and topography in regulating the epithelial to mesenchymal transformation (EMT) of cells. The EMT progression was examined by measuring the expressions of E-cad and B-cat in the cell-cell contacts as well as morphological polarization and vimentin expression to identify the degree of mesenchymal transformation. The findings presented in this chapter resulted in the following publication:

Samila Nasrollahi, and Amit Pathak. "Topographic confinement of epithelial clusters induces epithelial-to-mesenchymal transition in compliant matrices." Scientific reports 6 (2016): 18831-18831.

Chapter 3 addresses three fundamental questions regarding cell behavior in confinement:

1. How do matrix stiffness and confinement together regulate the mechano-activated state of the clustered cells?
2. How do macro and micro-scale matrix properties independently regulate cell motility in confinement of defined stiffness?
3. How do the co-cultured populations of epithelial cells sense confined environments and generate new modes of collective cell migration?

This chapter resulted into three manuscripts listed below:

Samila Nasrollahi, and Amit Pathak. "Hydrogel-based microchannels to measure confinement- and stiffness-sensitive YAP activity in epithelial clusters," in Press, MRS communication (2017).

Chapter 4 examines the role of past matrix properties in dictating the future collective behavior of epithelial cells when these cells traverse through diverse matrices of dissimilar stiffness. Although the influence of immediate matrix stiffness on cell migration is well-recognized, it remains unknown whether these matrix-dependent cellular features persist even after cells move to a new microenvironment. Our finding demonstrate that epithelial cells primed on a stiff matrix migrate faster, display higher actomyosin expression, and retain nuclear YAP even after arriving on a soft matrix, as compared to their control behavior on a homogeneously soft matrix. A manuscript based on the results presented in this chapter is under review.

Samila Nasrollahi, Christopher Walter, Gregory V. Schimizzi, Andrew J. Loza, Gregory D. Longmore, and Amit Pathak. "Past matrix stiffness primes epithelial cells and regulates their future collective migration through a mechanical memory," under review.

Chapter 2

Epithelial-mesenchymal transition in matrices of varying stiffness and confinement

2.1 Summary

Several recent studies have converged on the idea that the mechanical stiffness of extracellular matrices (ECM) strongly regulates the ability of epithelial cells to undergo epithelial-mesenchymal transition (EMT) and detach from their native clusters. In reality, these processes occur in heterogeneous microenvironments whose mechanical properties vary not only in terms of stiffness, but also topography, dimensionality, and confinement. However, it remains unknown whether ECM confinement influences EMT. In this study, using a novel microchannel-based scaffold of defined stiffness and geometry to culture epithelial clusters,

we report for the first time that EMT occurs more readily in confined environments. Notably, increased ECM confinement around epithelial clusters enhances EMT even in soft ECMs. This is a surprising revelation given the fact that soft ECMs are known to protect against EMT in unconstrained environments. We also demonstrate that confinement and stiffness induce EMT through cytoskeletal polarization and cell-ECM adhesions, respectively. Taken together, these findings highlight the influence of tissue microstructure on EMT regulation and bring a fresh perspective to the current paradigm of matrix stiffness dependent EMT.

2.2 Introduction

Epithelial-to-mesenchymal transition (EMT) enables epithelial cells to escape their native colony, attain motile phenotypes, and migrate through complex tissue barriers. While a co-ordinated form of EMT is essential during embryonic development, its dysfunctional versions can cause tissue fibrosis and cancer progression [1, 2]. The clusters and colonies of epithelial cells reside in complex microenvironments of varying mechanical properties, such as stiffness, topography, porosity, and dimensionality. There is growing evidence that mechanical cues present in the extracellular matrix (ECM), including stiffness and topography, regulate mechanosensitive subcellular pathways and influence cellular functions such as motility, differentiation, and fate decisions[3–9]. In particular, cells on stiffer ECMs generate higher actomyosin forces and form stronger adhesions, both of which are known to weaken cell-cell junctions [10, 11]. Several recent studies have demonstrated a direct relationship between ECM stiffness and the induction of EMT in various cell types and matrices. On stiff collagen-based matrices, mammary epithelial cells undergo EMT and attain an invasive phenotype

[10, 12, 13]. On stiff fibronectin substrates, alveolar epithelial cells become increasingly contractile and activate transforming growth factor (TGF-β), which leads to fibrosis-associated EMT [14,15]. Thus, it is likely that EMT might be sensitive to various mechanical properties that define the surrounding ECM. While the field has made great strides in understanding stiffness-dependent EMT [12, 15–17], the effects of topographical properties of the ECM on EMT remain largely unknown. This represents an important gap in knowledge given that tissue environments often vary in topography and confinement without significant variation in stiffness. For example, at the onset of carcinoma invasion, cell clusters being released from a tumor encounter discontinuities in the surrounding tissue, which results in varying degrees of ECM confinement around these epithelial clusters of tumor cells [18, 19]. Given the mechanical complexity of microenvironments surrounding the tumor cell clusters, it is of critical importance to understand how ECM topography combines with stiffness to induce EMT. In this work, we ask whether ECM stiffness and confinement can independently induce EMT. We also assess how subcellular mechanisms of force generation and adhesion formation influence this ECM-dependent mesenchymal transition. To conduct these studies, we employ a device that allows the culture of epithelial colonies in polyacrylamide (PA) channels of tunable stiffness and confinement. We cultured MCF10A mammary epithelial cells in this matrix platform and observed greater EMT inside narrower channels. Surprisingly, increased confinement leads to enhanced mesenchymal transition even in soft ECMs, which otherwise maintain an epithelial phenotype in unconfined (wide) channels. In narrow channels, cells adopt an elongated morphology, which might be indicative of their ability to sense ECM confinement by rearranging their cytoskeleton. Indeed, after the disruption of the cytoskeletal structure by pharmacological inhibition of microtubules and nonmuscle myosin II, cells lost their ability to undergo EMT in a confinement-dependent manner. We

also found that inhibition of focal adhesion kinase (FAK) disabled the effect of ECM stiffness on EMT. Our results suggest two different cellular mechanisms for confinement- and stiffness-sensitive EMT. First, the ability of cells to generate active actomyosin forces, maintain cytoskeletal structure through microtubules, and attain elongated shapes might play a central role in enabling confinement-sensitive EMT. Second, cell-ECM adhesions might be key mediators for triggering a mechano-transductive signaling cascade that weakens cell-cell adhesions and induces EMT. Taken together, these results bring a fresh perspective to the existing paradigm of matrix stiffness-dependent EMT and highlight that ECM confinement alone can disrupt the integrity of epithelial entities.

2.3 Results

2.3.1 Fabrication of a matrix platform with topographic confinement around epithelial clusters.

To mimic the growth of epithelial clusters in microenvironments of varying stiffness and topography, we fabricated an in vitro matrix platform as a polyacrylamide microchannels-based scaffold [4,20]. In this system, we used photolithography techniques to fabricate silicone masters of defined topography, as shown in Fig. 2.1, where channel width is prescribed in the mask design and the depth is dictated by the thickness of the photoresist layer. We polymerized PA solutions of specified monomer-crosslinker ratios against these masters, which yielded PA substrates of defined stiffness and topography. We estimated average channel height to be approximately 16 μm, measured by mixing fluorescent beads in the PA solution and performing confocal microscopy on polymerized PA gels Fig. 2.2. After seeding the

colony, we sealed the device by a PA layer of matching stiffness on top. In this system, as the epithelial colony grows beyond the center chamber, its branches are constrained within the channels that surround the chamber. Thus, we were able to create a defined level of topographic confinement around epithelial clusters with independently tunable ECM stiffness. To better understand how ECM confinement and stiffness might influence EMT in the context of breast cancer, where malignancies commonly develop from epithelial origin [21, 22] , we cultured mammary epithelial MCF10A cells in our PA-channels platform. We chose PA composition, as calibrated previously [4, 20, 23], corresponding to elastic moduli 1, 20, or 120 kPa.

2.3.2 Enhanced EMT signatures in stiffer and narrower channels.

To examine the progression of EMT in epithelial clusters confined inside channels of defined properties, we performed confocal microscopy to image the distributions of E-cadherin (E-cad), an epithelial marker [1, 24], after day 3, 4, and 5 of cell seeding Fig. 2.4. From these images, we quantified E-cad localization near the cell membrane (Fig. 2.3 and Fig. 2.4) because this molecule delocalizes from the membrane upon weakening of cell-cell junctions and induction of EMT. In wide channels made of soft (1 kPa) ECM, E-cad localization levels were the highest and the differences between day 3 and 5 were negligible. Thus, soft unconfined ECMs protect against EMT, consistent with previous studies [12,15,17], regardless of culture duration. Inside narrower channels made of soft ECM, the E-cad localization on day 3 was generally higher than that on day 5, which indicates a progression of EMT over time in confined environment even with low ECM stiffness. On stiff (120 kPa) ECM, E-cad localization on day 5 was consistently lower than that on day 3, regardless of channel width. Since the E-cad localization and the associated EMT induction appears to reach a steady

state at day 5, we decided to analyze EMT markers only after day 5 for all studies presented henceforth.

In soft (1 kPa) channels, we found that E-cad membrane localization decreased with channel width, which indicated a rise in EMT in more confined ECMs (Fig. 2.4, Fig. 2.5a). To confirm these findings with a mesenchymal marker, we quantified vimentin distribution for cell clusters in all channel widths. We found that vimentin expression increased with decreasing channel width (Figs. 2.5b,c), which corresponds to enhanced EMT in narrower channels. Taken together, E-cad and vimentin comparisons across channel widths in soft ECMs presented strong evidence for confinement-dependent EMT. Next, to examine the effect of ECM stiffness on EMT regulation in confinement, we repeated these experiments in channels made of 20 and 120 kPa PA gels. In these stiffer channels, we found that membrane localization of E-cad decreased and vimentin expression increased for higher ECM stiffness in all channel widths (Figs. 2.4, 2.5a-c, and 2.6), both of which indicate enhanced EMT in stiffer ECMs.Our results revealed that stiffness-dependent EMT previously observed on two-dimensional matrices [10, 15, 17] also holds true in confined ECM settings. While the effect of confinement on EMT induction was more pronounced in soft (1 kPa) ECMs, it persisted in stiffer (20 and 120 kPa) ECMs. Given this direct dependence of EMT markers on channel width, we hypothesized that topographic confinement of epithelial clusters might force the cells to attain elongated morphology and weaken cell-cell junctions. To pursue this hypothesis, we first quantified elongation of individual cells in epithelial clusters inside channels in terms of aspect ratio. As shown in Fig. 2.5d, we found that cells in narrower channels were more elongated for 1 and 20 kPa stiffness conditions. However, cells were maximally elongated in channels of 120 kPa stiffness regardless of channel width. Thus, the elongation of epithelial cells in narrow channels correlated with confinement-dependent induction of EMT.

2.3.3 Disruption of cytoskeletal structure blunts confinement-sensitive EMT.

To test the connection between elongated cell morphology (Fig. 2.5d) and enhanced EMT in narrow channels (Figs. 2.4, 2.5a-c, and 2.6), we sought to disrupt the ability of cells to rearrange their cytoskeletal structure and elongate in a coordinated manner. We hypothesized that elongation of cells along channel walls might aid their ability to sense ECM confinement. We approached this goal in two different ways. First, we inhibited non-muscle myosin II (Myo) by blebbistatin treatment, which is known to abrogate the generation of active actomyosin forces in cells. While Myo-inhibited cells were more elongated compared to the control cells, they showed no significant differences across channel widths (Fig. 2.7a). Thus, Myo-inhibition rendered the cells unable to elongate differently in channels of varying confinement. Second, through nocodazole treatment, we inhibited microtubules (MTb) that support the cytoskeletal structure, help stabilize cellular protrusions [25, 26], and allow the cells to attain elongated shapes. We found that the elongation of MTb-inhibited cells declined dramatically across all ECM conditions (Fig. 2.7b). Importantly, even in the narrowest channels (20 μm width) MTb-inhibited cells were unable to exploit confinement and elongate along channel walls.

To examine the respective effects of Myo and MTb inhibition on confinement-sensitive EMT, we imaged E-cad and vimentin distributions for each condition. In stiff ECM, membrane localization of E-cad in Myo-inhibited cells did not vary with channel width (Figs. 2.7c,e), indicating a confinement-independent EMT. However, in soft ECM, E-cad localization in narrower channels (20 and 40 μm) was lower than that in wider channels (80 and 200 μm), which is similar to the confinement-sensitive trend in control conditions (Fig. 2.5a). While

Myo-inhibition disabled confinement-sensitive EMT in stiff ECMs, it did not have the same effect in soft ECMs (Fig. 2.7c,e).

Next, to assess the role of passive structural properties of the cytoskeleton and MTb-based protrusions in regulating confinement-sensitive EMT, we repeated E-cad measurements after nocodazole treatment. In stiff channels, E-cad expression became insensitive to confinement (Fig. 2.7d,f). In soft channels, MTb-inhibition was far more effective than Myo-inhibition in reducing the effect of confinement on E-cad localization. Notably, since E-cad expression in soft channels of 20, 40, and 80 μm widths was not significantly different (Fig. 2.7f), these results indicated that microtubules are essential for epithelial clusters to sense ECM confinement. In other words, after MTb-inhibition, cells in epithelial clusters neither elongated in narrow channels (Fig. 2.7b), nor underwent confinement-sensitive EMT (Fig. 2.7d,f). We confirmed these findings of stiffness and confinement sensitive EMT after Myo- or MTb-inhibition by measuring vimentin expression under the same ECM conditions (Fig. 2.8).

2.3.4 Inhibition of cell-ECM adhesions reduces the effect of ECM stiffness on EMT.

While the disruption of cytoskeletal structure blunted confinement-sensitive cell behavior, stiffness-dependent differences in EMT markers persisted, especially in wide channels (Figs. 2.7e,f and 2.8c,d). Given that cell-ECM adhesions are key mediators of cellular mechanotransduction [27, 28], we hypothesized that the inhibition of focal adhesion kinase (FAK) might disable the cell's ability to sense ECM stiffness and in turn prevent stiffness-sensitive EMT in channels. To test this hypothesis, we measured the expressions of E-cad (Fig. 2.9a) in PA channels after pharmacological inhibition of FAK (by treating the cells with PF228).

We found that E-cad localization was statistically similar in both soft and stiff ECMs in all channel widths (Fig. 2.9c). The visualization and quantification of vimentin expression confirmed this trend of stiffness-independent EMT (Fig. 2.9b,d). Thus, inhibition of cell-ECM adhesions rendered epithelial clusters unable to sense ECM stiffness and undergo EMT in stiffer ECMs. Notably, the E-cad and vimentin expressions varied with channel width in both soft and stiff ECMs, which indicates that the confinement-sensitive EMT persisted even after the disruption of cell-ECM adhesions.

2.3.5 Relative contributions of subcellular and extracellular inputs in mechanosensitive regulation of EMT.

To further clarify relative contributions of extracellular inputs to the mechanosensitive regulation of EMT, we calculated "sensitivity" indices corresponding to each ECM property as the percentage change in E-cad localization compared to a reference condition (1kPa for 'stiffness sensitivity' and 200 μm for 'confinement sensitivity'). First, we calculated 'stiffness sensitivity', defined as the percentage change in E-cad localization in stiff ECMs relative to its value in soft ECMs, for any given channel width or knockdown state (Fig. 2.10a). We found that E-cad localization was most sensitive to stiffness in wide channels across all knockdown (control, –Myo, –MTb, and –FAK) conditions. Interpreted another way, the ability of epithelial clusters to undergo stiffness-dependent EMT went down in confined ECM settings. As noted earlier and confirmed here, the stiffness-sensitivity was highest for control cells and lowest for FAK-knockdown across all channel widths. Next, we computed 'confinement sensitivity', defined as the percentage change in E-cad localization in narrow (20 μm) channels relative to its value in wide (200 μm) channels, for any given PA stiffness or knockdown state (Fig. 2.10b). In both soft and stiff ECMs, control cells were the most

confinement sensitive, followed by FAK- and Myo-knockdown states, with MTb-knockdown cells as the least confinement-sensitive. We also noted that epithelial clusters were more confinement sensitive in softer ECM for all knockdown states.

2.4 Discussion

Epithelial clusters of cells emanate from a tumor and interact with the surrounding microenvironment of varying elasticity and geometry. During this interaction with mechanically heterogeneous ECMs, tumor cells in epithelial clusters attain an invasive phenotype by undergoing EMT. While recent studies on different cell types and ECMs have shown that stiffening of the microenvironment can enhance EMT [12, 15–17], the influence of matrix topography and confinement on EMT has remained largely unexplored. This gap in knowledge exists mainly due to a marked absence of cell culture platforms that allow independent control over stiffness and confinement of the ECM surrounding the epithelial clusters. In this work, we addressed this challenge by designing a matrix platform for culturing cell clusters in PA channels of varying width and stiffness. Using this device, we have uncovered a previously unidentified confinement-dependent EMT phenotype in soft ECM. While previous studies have indicated that the mechanosensitive EMT remains inactive on soft 2D substrates [15, 16], our findings reveal that confined topography of the environment alone can induce EMT even on soft ECMs. On stiffer ECM (120 kPa), mesenchymal transition accelerates regardless of channel width, consistent with previous studies [12, 15–17]. While it is known that cancer cell clusters of different shapes and sizes can invade tissue microenvironments of different stiffness and topography [18, 19], our current understanding of EMT is derived mainly from experiments of epithelial colonies on flat surfaces. Our experimental framework

of epithelial clusters in ECMs of defined stiffness and topography can potentially serve as a new platform for studying how groups of cells respond to ECMs that more closely mimic the tissue microenvironments in vivo. Through the presented work, we have initiated this effort by identifying that morphological adaptation of cells to the topography of their surrounding environment and the communication of intracellular forces through cell-ECM adhesions are likely central mechanisms by which ECM properties influence the state of cell-cell junctions in epithelial clusters.

Our findings provide a fresh perspective to the emerging body of work on the regulation of mechanosensitive EMT by the mechanical properties of the ECM [12, 14, 16, 17, 29–31]. In particular, on stiff ECMs, increased cell contractility results in mechano-activation of TGF-β, which in turn leads to dissociation of cell-cell junctions and a down regulation of epithelial markers. It has also been shown that epithelial clusters seeded on topographically aligned fibers experience a elongation of cell shape along the fibers, which leads to increased cell tension, upregulation of TGF-β, and the associated mesenchymal transition [29, 32]. However, it has been unclear whether the macro-scale confinement of clusters can induce mechanosensitive EMT similar to the phenotypes noted above. Our results fill this important gap in knowledge by revealing that ECM confinement alone is able to induce EMT in epithelial clusters seeded inside narrow channels. Our measurements of E-cad localization over time demonstrate that the mechano-regulation of EMT, either by ECM stiffness or by confinement, benefits from longer duration of culture in stiffer or more confined ECMs. We hypothesized that the ability of epithelial cells to adapt to confined environments by elongating their shape might play an important role in the regulation of confinement-sensitive mesenchymal transition. To test this hypothesis, we targeted microtubules because of their ability to extend protrusions and simultaneously provide compressive mechanical properties to the cytoskeleton during cellular shape changes [33]. Pharmacological inhibition of

microtubules abrogated the ability of cells to elongate in confined channels, which led to statistically similar EMT markers across channel width. These results indicate that cells sense and respond to confined environments through adaptive morphological polarization, leading to force alignment in the cell and weakening of cell-cell junctions. However, cell elongation is not the necessary and sufficient condition for creating a friendly environment for EMT induction. The elongated cells also require a stable intracellular force generation machinery to exploit the concentration of forces on cell-cell junctions. We tested this hypothesis by blebbistatin-treatment, which is known to abrogate actomyosin forces and increase cell elongation [34, 35]. Here, despite increased elongation, blebbistatin-treated cells in confined channels were unable to exert forces required to break cell-cell junctions and induce EMT. These results support the framework in which cells in epithelial clusters require both the actomyosin forces and the ability to elongate in confined ECMs; and, disruption of either one of these mechanisms blunts confinement-sensitive EMT. Surprisingly, cells continued to display different EMT markers on soft and stiff ECMs even in the absence of actomyosin forces and the ability to sense confinement. Since the communication of mechanotransductive signaling between the cell and the ECM occurs through focal adhesions, we performed FAK-inhibition and found that epithelial clusters in soft and stiff channels exhibited similar EMT markers. Thus, the stiffness-sensitive EMT requires stable cell-ECM adhesions, which in turn allow actomyosin forces to rise and weaken cell-cell junctions. While actomyosin contractility and focal adhesions are known to cooperatively regulate stiffness sensing in cells [36,37], respective effects of myosin-inhibition on cytoskeletal structure and FAK-inhi12,15bition on adhesions alone might lead to different kinds of disruption of stiffness-sensing. Thus, despite their common link of abrogated stiffness sensing, the disrupted cytoskeletal structure of -Myo cells is expected to have different effect on EMT induction than the –FAK cells. In the proposed

paradigm of ECM-dependent EMT, while ECM stiffness regulates mechanotransductive signaling and force generation within cells, ECM confinement alters the spatial organization of forces through morphological polarization of cells. Overall, these findings highlight that topographical structure and mechanical stiffness of the tissue microenvironment can both independently regulate EMT, which challenges the current view of matrix stiffness-dependent dissemination of cells from tumor sites.

2.5 Methods

2.5.1 Fabrication of Polyacrylamide (PA) Device.

Silicon master of defined topographical feature was fabricated using a standard photolithography technique. A silicon wafer was cleaned ultrasonically, a layer of SU-8 2015 photoresist (MicroChem) was spin-coated to a thickness of 30 μm, and exposed to 365 nm UV light through a photo-mask of defined geometry. The patterns on the mask are in the form of a well (5 mm diameter), surrounded by channels of widths between 20-200 μm. After dissolving the undeveloped photoresist from the wafer using a SU-8 developer solution (MicroChem), uniformity in channel depth was verified by optical profilometry. Next, the wafer was immersed in Sigmacoat (Sigma Aldrich) for 1 h, washed thoroughly with deionized (DI) water, and dried on the hot plate for 30mins, which yielded a hydrophobic silicon master. A PA solution, enough to achieve a 100 μm thick gel, was sandwiched between the microchannels master and a reactive coverslip, treated according to an established protocol [4, 20]. The PA precursor solutions were mixed by choosing monomer:crosslinker ratios based on previous stiffness characterizations of PA gels – acrylamide:bisacrylamide (A:B) percentages of

5%A:0.2%B, 8%A:0.6%B, and 15%A:1.2%B corresponding to PA elastic moduli of 1, 20, and 120 kPa [4, 23]. Following polymerization of the PA solution, coverslips containing the polymerized PA gels were carefully peeled off from the wafer, which resulted in molded PA gels relative to the topographic features on the master. These PA devices with wells and channels were immersed in PBS and stored at 4℃ before use. The PA devices were UV sterilized for 1hr and functionalized with extracellular protein by pipetting 1ml of 0.1mg/ml type I collagen (rat tail collagen, Santa Cruz Technologies) on to the PA surface and incubated overnight at 4℃. To measure channel height, fluorescent latex micro-beads (Sigma Aldrich) of 0.5μm diameter were mixed with the PA solution (1:250 ratio) and confocal microscopy was performed after polymerization (Fig. 2.21). Using this method, the average channel height was estimated to be approximately 16 μm with a standard deviation of 2.4 μm, from N>14 across at least 5 samples for all four channel widths.

2.5.2 Cell Culture and Immunofluorescence.

MCF-10A mammary epithelial cells were grown, as previously described [38], in DMEM/F12 (Invitrogen), with 5% (v/v) horse serum (Invitrogen), 20 ng/mL epidermal growth factor (EGF, Miltenyi Biotec Inc), 0.5 mg/mL hydrocortisone (Sigma-Aldrich), 100 ng/mL cholera toxin (Sigma-Aldrich), 10 ug/mL insulin (Sigma-Aldrich), and 1% (v/v) penicillin-streptomycin (Sigma-Aldrich). To create an epithelial cell colony, 15,000 cells were seeded in the central chamber of the PA devices, growth media was added, and these cell-laden devices were incubated at 37℃ and 5% CO2 for 5days. On day 3 of the assay period, media was replenished for control conditions. For nonmuscle myosin II inhibition, blebbestatin (Sigma-Aldrich; 10μM) was added on day 4. For microtubules inhibition, nocodozole (Sigma-Aldrich; 5μm) was added on day 4. For FAK inhibition, PF573228 (Tocris Bioscience; 5 μM) was

added on day 3. All samples were fixed on day 5. For vimentin staining, cells were fixed with 4% paraformaldehyde (Santa Cruz Technologies) in PBS, followed by permeabilization of cell membrane with 0.5% Triton-X 100 (Sigma-Aldrich) and blocking with 1% bovine albumin serum (BSA) (EMD milipore). For E-cad staining, cells were fixed in ice-cold methanol (99.5%, Sigma-Aldrich) and blocked with 1% BSA. The following antibodies were used for immunofluorescence: mouse monoclonal E-cadherin (BD Biosciences; diluted 1:500), rabbit monoclonal vimentin (Cell Signaling; diluted 1:200), and Alexa Fluor 488-labeled goat anti-mouse and Alexa Fluor 647-labeled goat anti-rabbit (Invitrogen; diluted 1:500).

2.5.3 Confocal Microscopy and Image Analysis.

Confocal microscopy was conducted using a Zeiss LSM 710 laser-scanning confocal microscope (Carl Zeiss Microscopy), where confocal stacks were acquired at 1μm interval and combined using the Z-projection tool in ImageJ (NIH). All image acquisition parameters including laser power, scan speed, pixel resolution were kept constant to ensure quantitative image analysis. Using the Z-projected E-cad images, the membrane localized E-cad was computed by first subtracting the average cytosolic expression of E-cad in any given cluster of cells (Fig. 2.3b), which were chosen by drawing a region of interest (ROI) around the clusters embedded inside microchannels of defined width. Here, the cytosolic (non-membrane) E-cad expression was computed by measuring pixel values in small regions within individual cells and averaging over at least 7 cells for each ROI. To quantify membrane localized E-cad, the sum of pixel values in any given ROI was normalized by cell density. To ensure the efficacy of this method for quantifying E-cad membrane localization, a second method was employed where E-cad expression was plotted along a line through two adjoining cells and

the ratio between cytoplasmic and junctional E-cad expression was noted as " normalized E-cad junctional localization", as illustrated in Fig. 2.3d,e. These calculations were performed for the control case, in all channels widths of both soft and stiff ECMs, and the trends were compared with the first method (Fig. 2.3b,c). Based on a general agreement between the calculations from these two methods (compare Fig. 2.3c and 2.3e), the first method of average E-cad localization (Fig. 2.3b,c) is adopted due its high throughput nature for all measurements presented in the main manuscript. For vimentin expression quantification, the Z-projected vimentin images were analyzed using a custom-built macro in ImageJ to measure the area occupied by the vimentin-expressing intermediate filaments. First, each image was processed by subtracting the background and converting the image to black and white through the binary settings tool in ImageJ. Subsequently, the expression level of vimentin was computed by totaling the number of pixels with a non-zero value and normalizing by cell density in the ROI. For morphological analysis, the shape analysis tool in ImageJ was employed to measure aspect ratios, defined as the ratio of the major axis/minor axis length.

2.5.4 Statistical Analysis.

Data are expressed as the mean standard deviation. Statistical significance between means was determined by two-way ANOVA followed by Tukey-Kramer HSD (honestly significant difference) for pairwise comparisons in MATLAB (Mathworks). Means were calculated from N>8 clusters of numerous cells, corresponding to images acquired from at least three separate experiments. The size of the cell cluster varied with channel width: n>10 cells/cluster in a 20 μm channel, n>25 cells/cluster in a 40 μm channel, n>45 cells/cluster in a 80 μm channel, and n>90 cells/cluster in a 200 μm channel. For E-cad sensitivity indices (Fig. 2.10, defined as the percentage difference in means between conditions x and y, standard deviation was

calculated as $\sigma_z = \mu\sqrt{\sigma_x^2 + \sigma_y^2}$, where μ is the ratio of means μ_x and μ_y , σ_x^2 is variance of x, and σ_y^2 is variance of y [39].

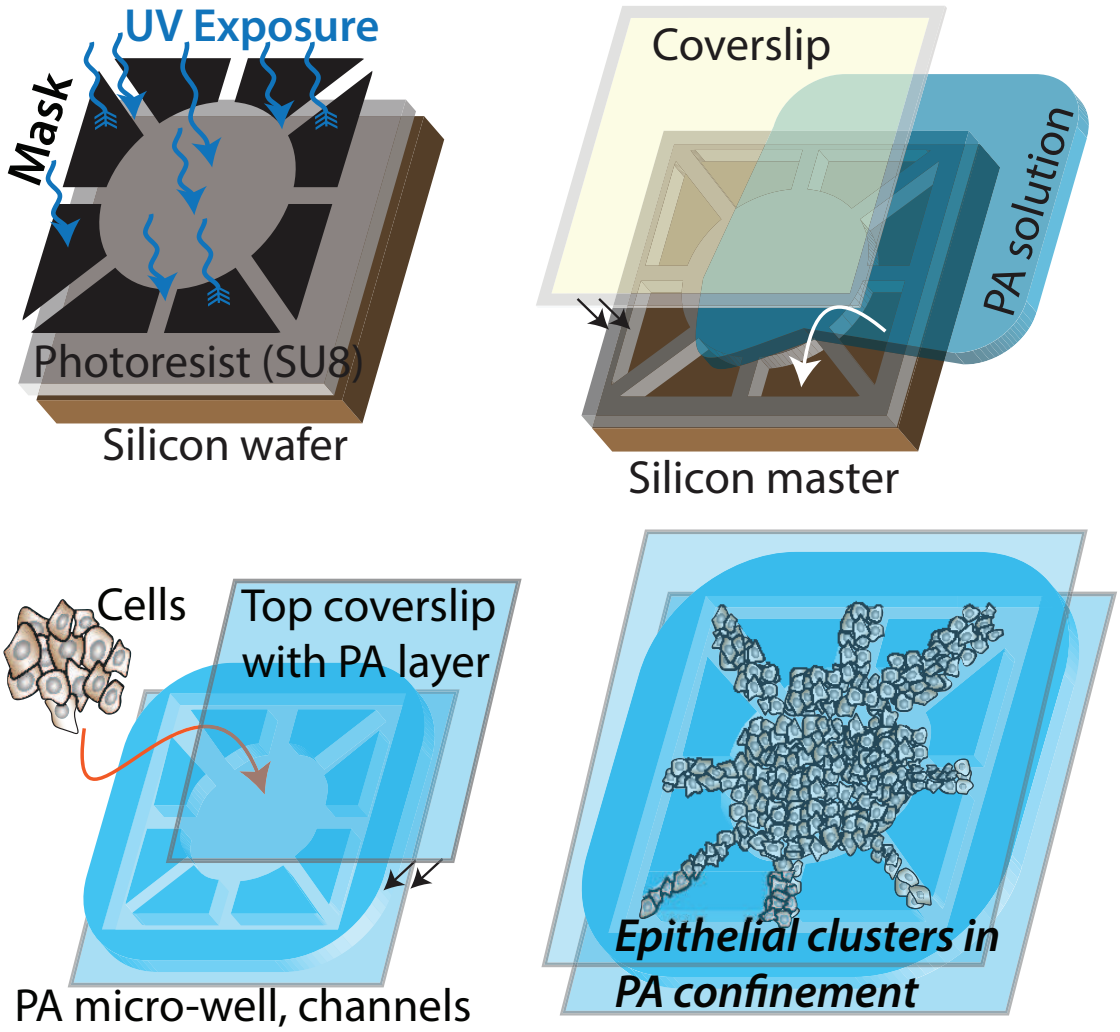

Figure 2.1: **Fabrication of microchannel-based culture platform for epithelial clusters.** Schematic describing the fabrication steps for molding polyacrylamide (PA) hydrogels of prescribed stiffness against photolithographically fabricated masters of defined topography. The device is designed such that an epithelial colony of MCF10A cells can be seeded in the center well and allowed to grow into peripheral PA-channels of defined stiffness and confinement.

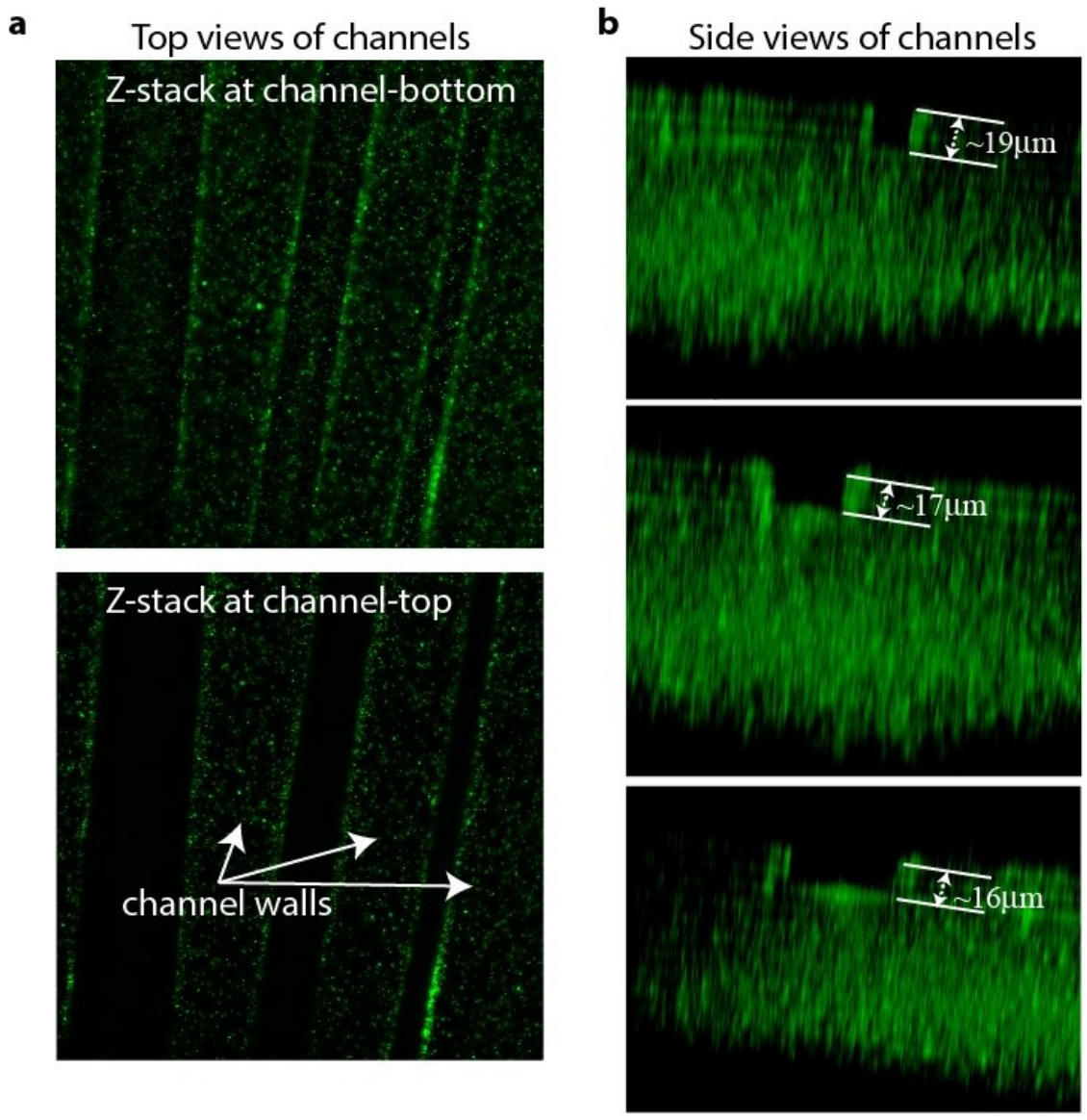

Figure 2.2: **Estimation of channel heights.** (a) Confocal images of fluorescent micro-beads mixed in PA gels showing Z-stacks at the top and the bottom surfaces of the channels. (b) Visualizing channel height through lateral views of channels, obtained by 3D volume construction of the confocal Z-stack images of fluorescent micro-beads embedded in PA gels..

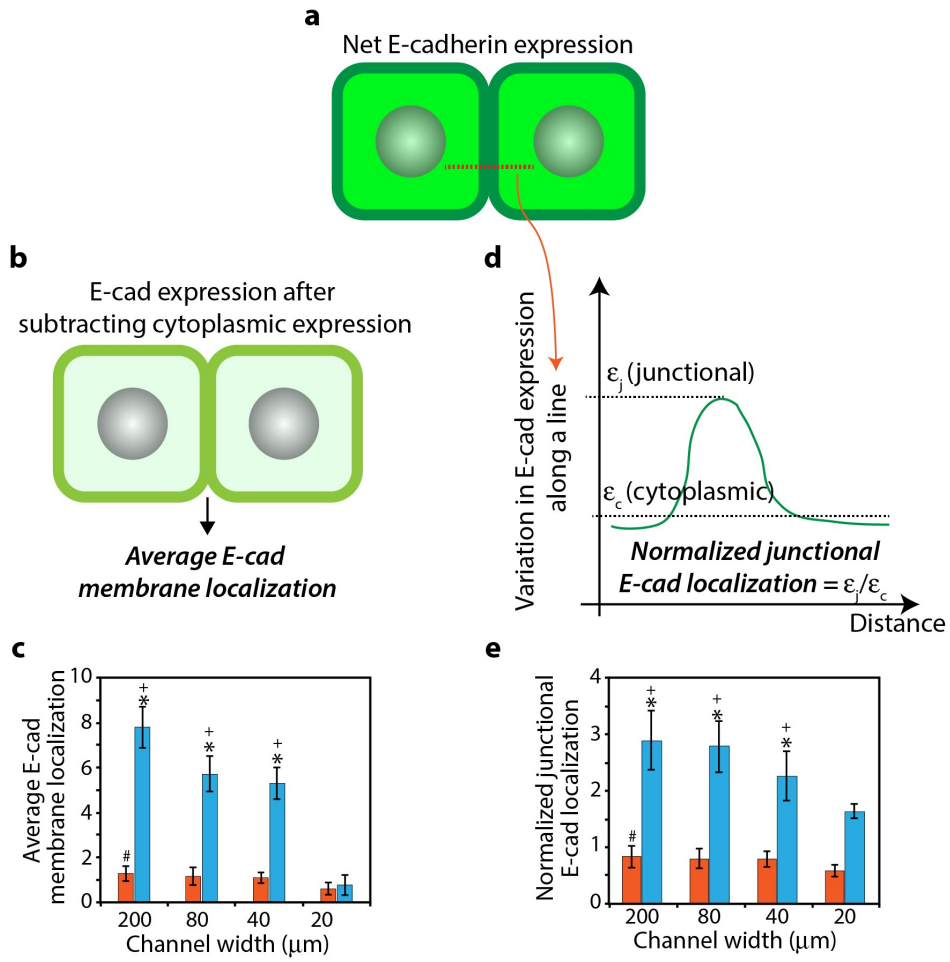

Figure 2.3: **Comparison of two methods for quantifying E-cad localization.** (a) Schematic describing a typical image of E-cad expression in both the cytoplasm and at intercellular membrane junctions. (b) Schematic describing E-cad junctional expression obtained after subtracting the cytoplasmic E-cad expression. (c) Average E-cad membrane localization calculated by summing pixel intensity in the subtracted image and normalizing by cell density, for channels of varying width and stiffness. N>8 clusters of numerous cells, from at least three separate experiments (see details in Methods). (d) Schematic describing a second method of quantifying E-cad junctional localization where E-cad expression along a line drawn between two cells varies such that it reaches a peak value at the intercellular boundary. Here, normalized E-cad junctional localization is computed as the ratio of the junctional E-cad expression, ϵ_j, and the cytoplasmic E-cad expression, ϵ_c. (e) Normalized E-cad junctional localization (ϵ_j/ϵ_c) calculated by drawing lines between cells inside channels of varying width and stiffness. N>15 pairs of cells per condition, from at least three separate experiments. The general agreement of trends in (c) and (e) demonstrates that the two methods are equivalent. *p<0.05 with respect to stiff ECM. $^{+}$p<0.05 with respect to narrow (20 μm) channels for 1 kPa stiffness. $^{\#}$p<0.05 with respect to narrow channels for 120 kPa stiffness.

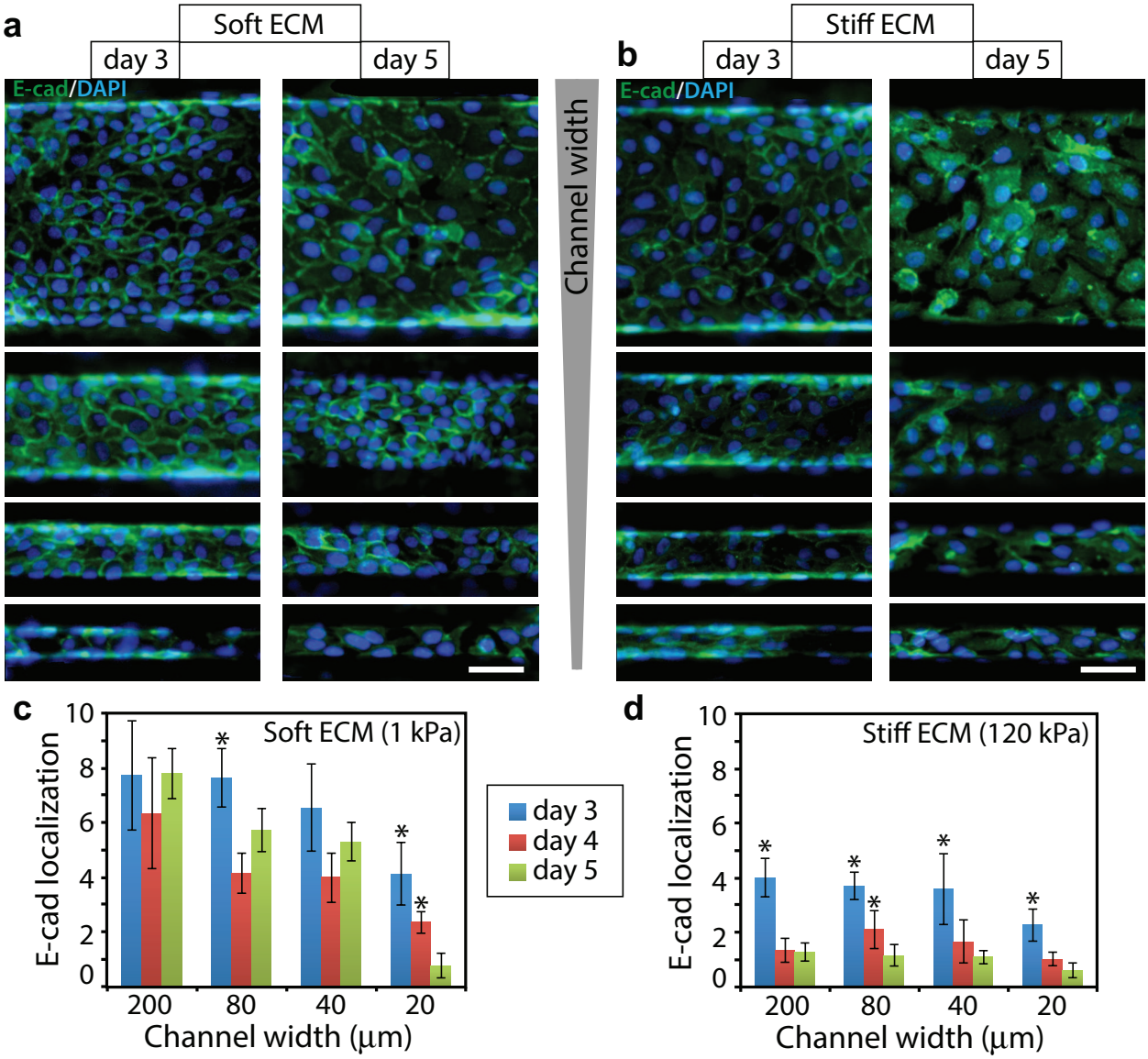

Figure 2.4: **Change in E-cad expression over time in ECMs of varying stiffness and confinement.** Change in E-cad expression over time in ECMs of varying stiffness and confinement. Representative immunofluorescence images of E-cad (green) expression with DAPI (blue) in MCF10A cell clusters cultured for either 3 or 5 days inside channels made of (a) soft, 1 kPa, and (b) stiff, 120 kPa, PA gels, with channel widths ranging between 20-200 μm; Scale bar = μm. Average fluorescence intensity of membrane localized E-cad in epithelial clusters seeded for 3, 4, or 5 days, inside (c) soft and (d) stiff PA channels of varying widths. $^{*}p<0.05$ with respect to day 5 values for any given channel condition. N>7 clusters of numerous cells, from at least two separate experiments (see details in Methods).

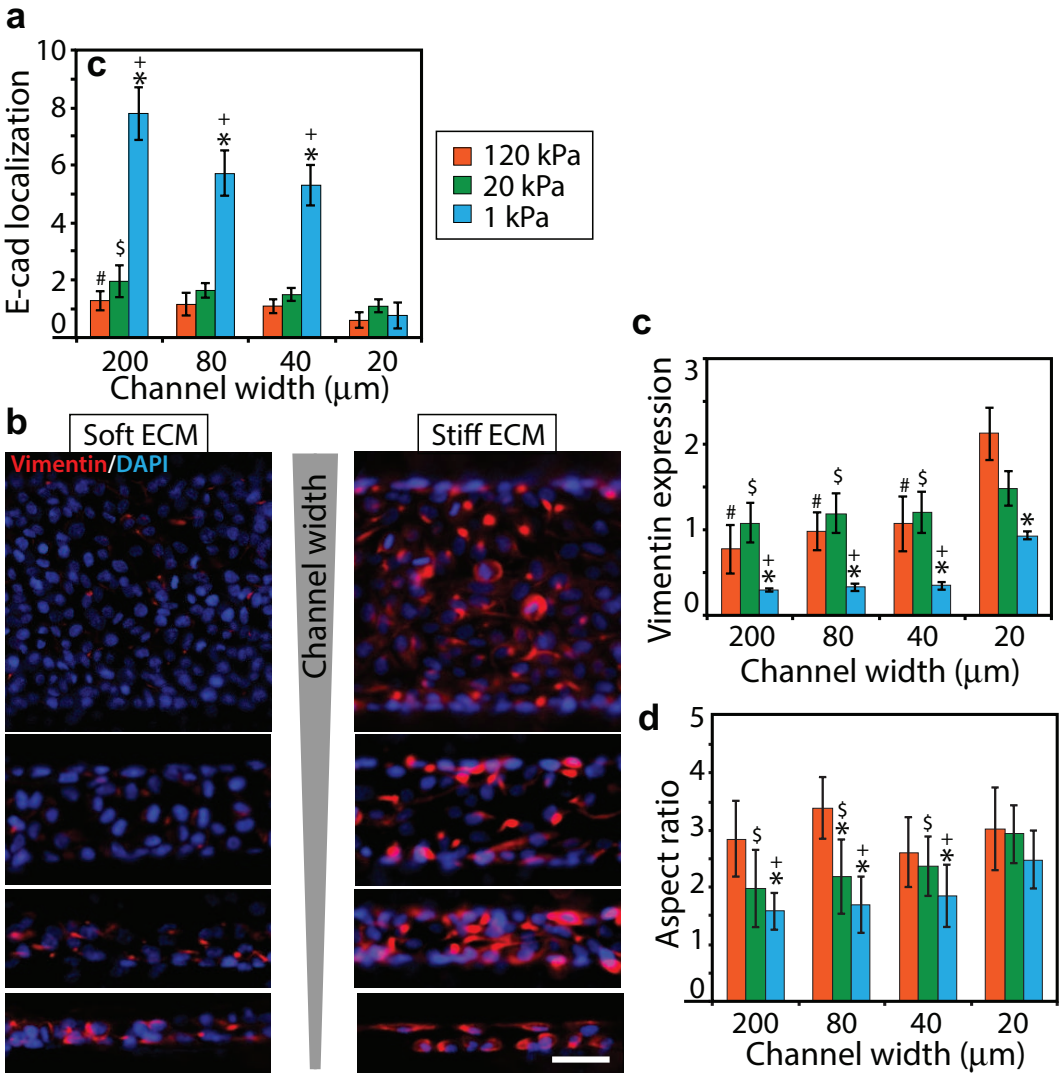

Figure 2.5: **Regulation of EMT by ECM confinement and stiffness.** (a) Average fluorescence intensity of membrane localized E-cad in epithelial clusters after 5 days of culture inside PA channels of varying widths and stiffness between 1-120 kPa. (b) Representative immunofluorescence images of vimentin (red) expressions with DAPI (blue) in MCF10A cell clusters cultured inside channels made of soft (1 kPa) and stiff (120 kPa) PA gels after day 5, with channel widths ranging between 20-200 μm; see split DAPI and vimentin images in Fig. 2.13. Scale bar = 50 μm. (c) Average fluorescence intensity of vimentin expression in epithelial clusters after 5 days of culture inside PA channels of varying widths and stiffness between 1-120 kPa. (d) Elongation of cells in the clusters confined inside PA channels measured as aspect ratio. $^{*}p<0.05$ with respect to stiff ECM. $^{+}p<0.05$ with respect to narrow (20 μm) channels for 1 kPa stiffness. $^{\$}p<0.05$ with respect to narrow channels for 20 kPa stiffness. $^{\#}p<0.05$ with respect to narrow channels for 120 kPa stiffness. N>8 clusters of numerous cells, from at least three separate experiments.

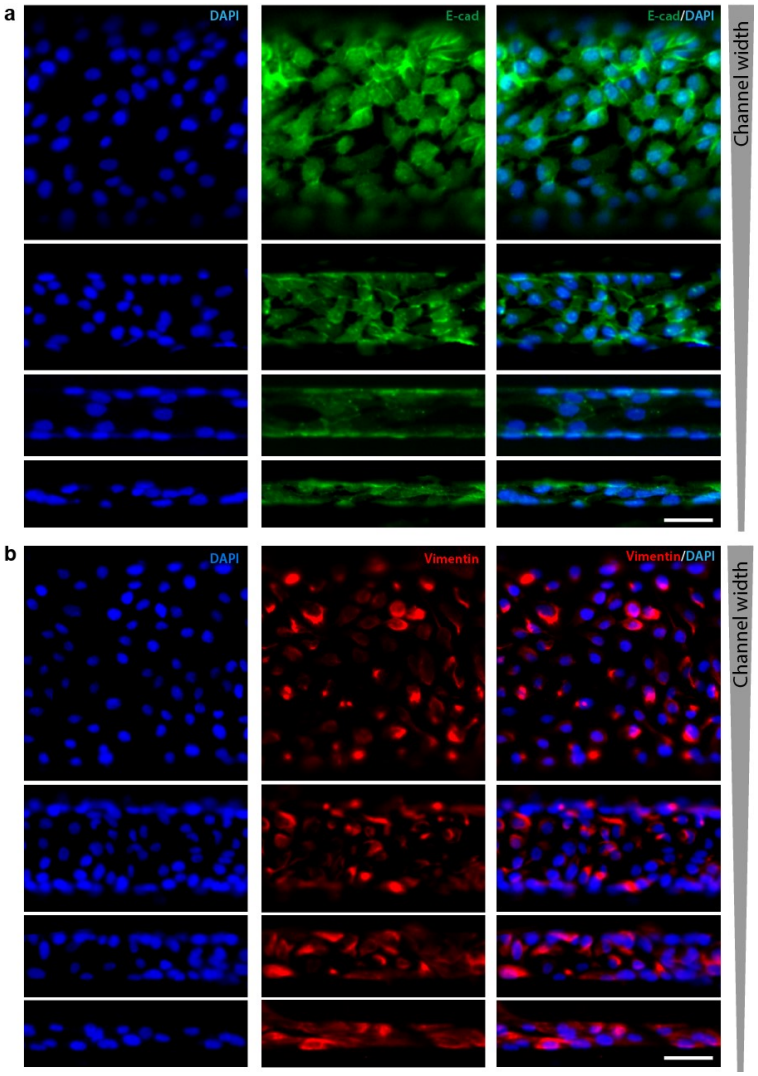

Figure 2.6: **Split images of E-cad, vimentin and DAPI distributions for ECM stiffness of 20 kPa.** Immunofluorescence images of DAPI, (a) E-cad, and (b) vimentin distributions after 5 days of culture inside channels made of PA gels of 20 kPa stiffness, with channel widths between 20-200 μm. Scale bar = 50 μm.

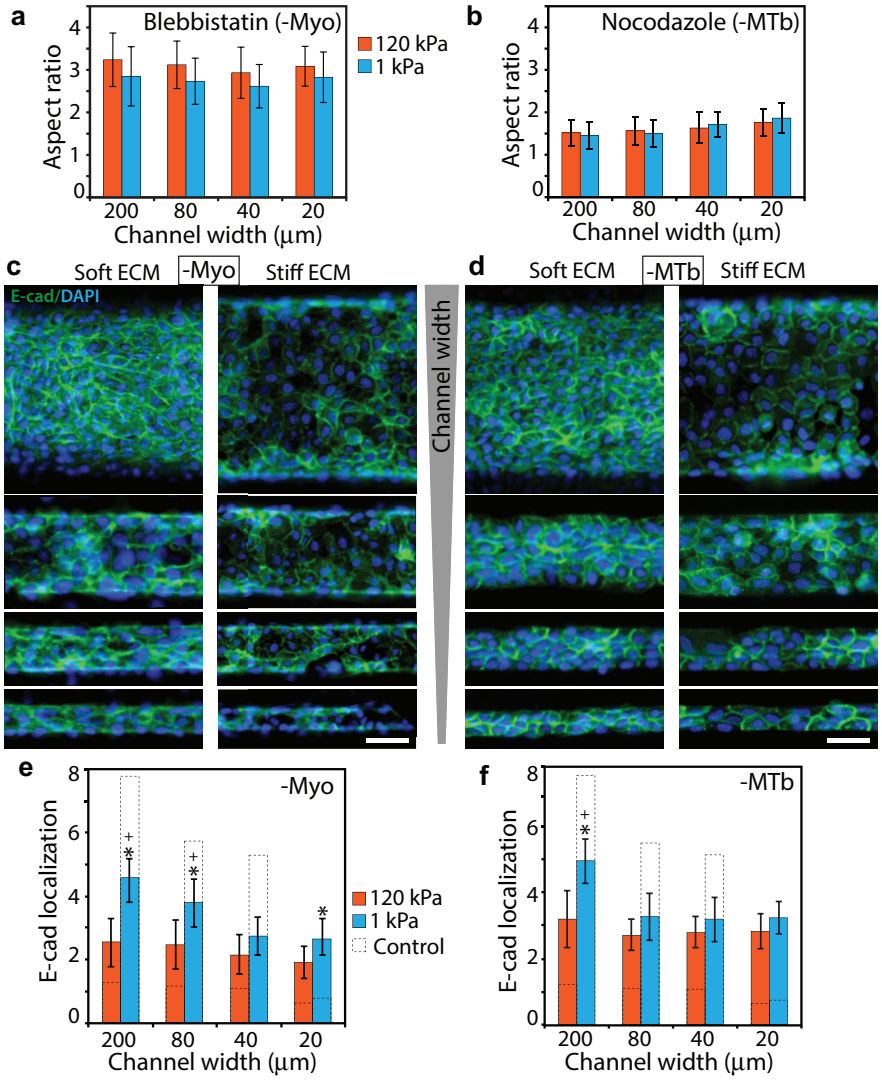

Figure 2.7: **Effects of myosin II and microtubules inhibition on epithelial clusters in confinement.** Elongation of cells in the clusters confined inside PA channels, measured as aspect ratio, after (a) blebbistatin or (b) nocodazole treatment. Representative immunofluorescence images of E-cad (green) expression with DAPI (blue) in (c) blebbistatin- and (d) nocodazole-treated cells cultured inside channels made of soft and stiff PA gels, with widths between 20-200 μm; see split DAPI and E-cad images in Figs. 2.15,2.16. Scale bar = 50 μm. Average fluorescence intensity of membrane localized E-cad in (e) blebbistatin- and (f) nocodazole-treated cells cultured in PA channels of varying width and stiffness. $^{*}p<0.05$ with respect to stiff ECM. $^{+}p<0.05$ with respect to narrow (20 μm) channels for 1 kPa stiffness. No significant difference across channel widths for 120 kPa stiffness. N>8 clusters of numerous cells, from at least three separate experiments (see details in Methods).

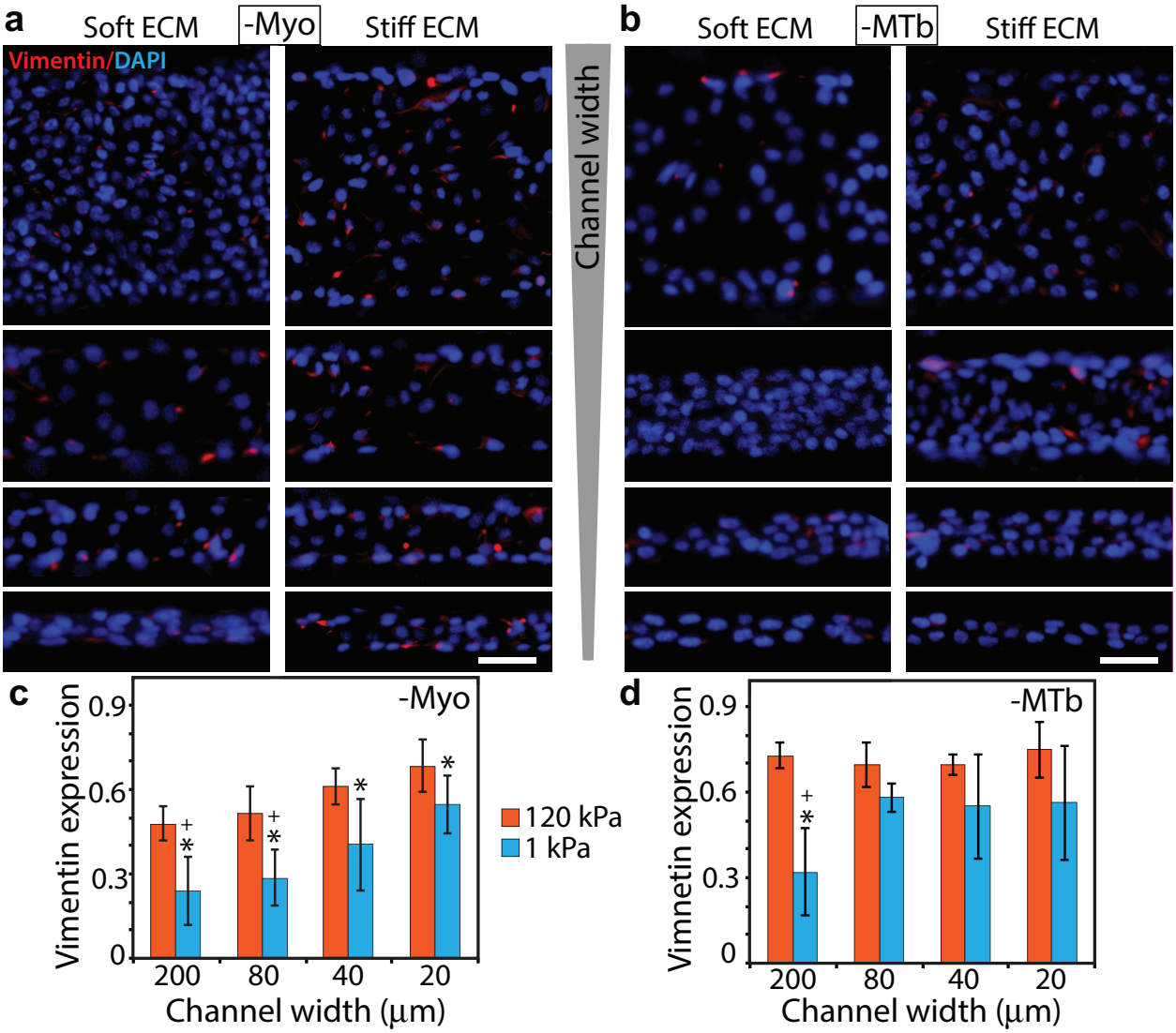

Figure 2.8: **Effects of Myo- and MTb-inhibition on vimentin expression in channel-confined epithelial clusters.** Representative immunofluorescence images of vimentin (red) expression with DAPI (blue) in (a) blebbistatin- and (b) nocodazole-treated cells cultured inside channels made of soft and stiff PA gels, with widths between 20-200 μm; see split DAPI and vimentin images in Figs. 2.17,2.18. Scale bar = 50 μm. Average fluorescence intensity of vimentin in (c) blebbistatin- and (d) nocodazole-treated cells cultured in PA channels of varying width and stiffness. $^{*}p<0.05$ with respect to stiff ECM. $^{+}p<0.05$ with respect to narrow (20 μm) channels for 1 kPa stiffness. No significant difference across channel widths for 120 kPa stiffness. N>8 clusters of numerous cells, from at least three separate experiments (see details in Methods).

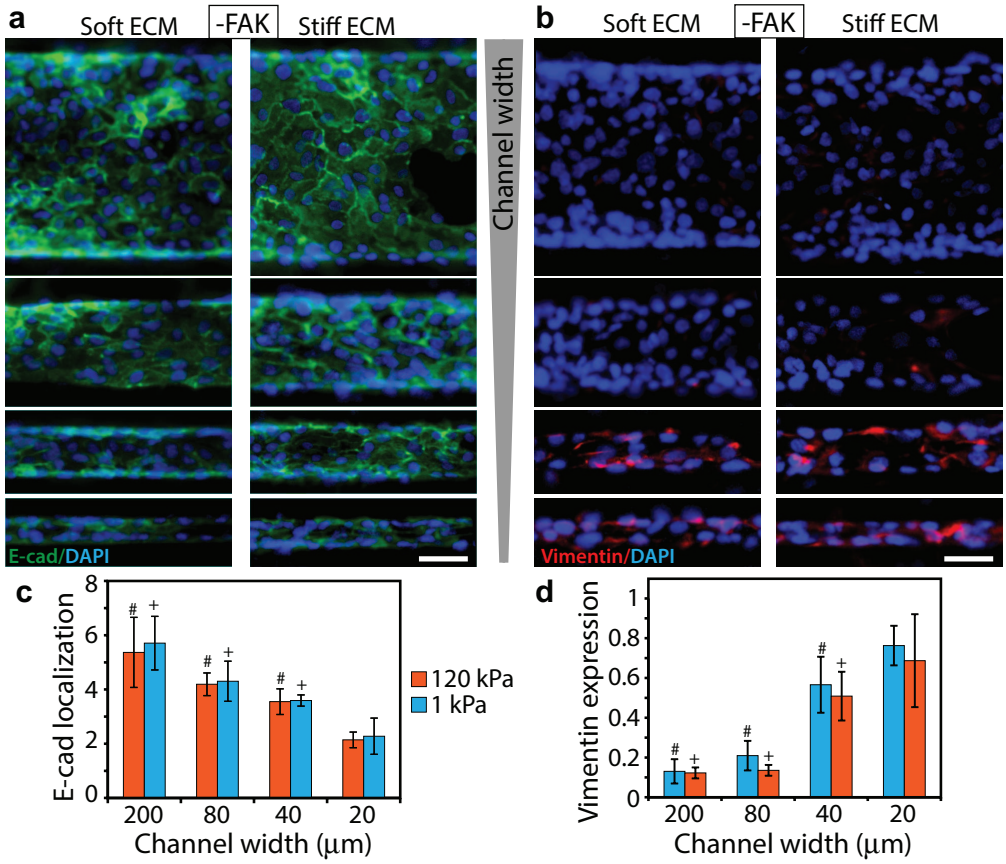

Figure 2.9: **Effect of FAK inhibition on ECM-dependent EMT.** Representative immunofluorescence images of (a) E-cad (green) and (b) vimentin (red) expressions with DAPI (blue) in cells treated with FAK inhibitor PF228 in channels made of soft and stiff PA gels, with widths between 20-200 μm; see split DAPI, E-cad, and vimentin images in Figs. 2.19,2.20. Scale bar = 50 μm. Average fluorescence intensity of (c) membrane localized E-cad and (d) vimentin expression in FAK-inhibited cells cultured in PA channels of varying width and stiffness. $^{+}p<0.05$ with respect to narrow (20 μm) channels for 1 kPa stiffness. $^{\#}p<0.05$ with respect to narrow channels for 120 kPa stiffness. No significant difference between soft and stiff ECMs for any channel width. N>8 clusters of numerous cells, from at least three separate experiments (see details in Methods).

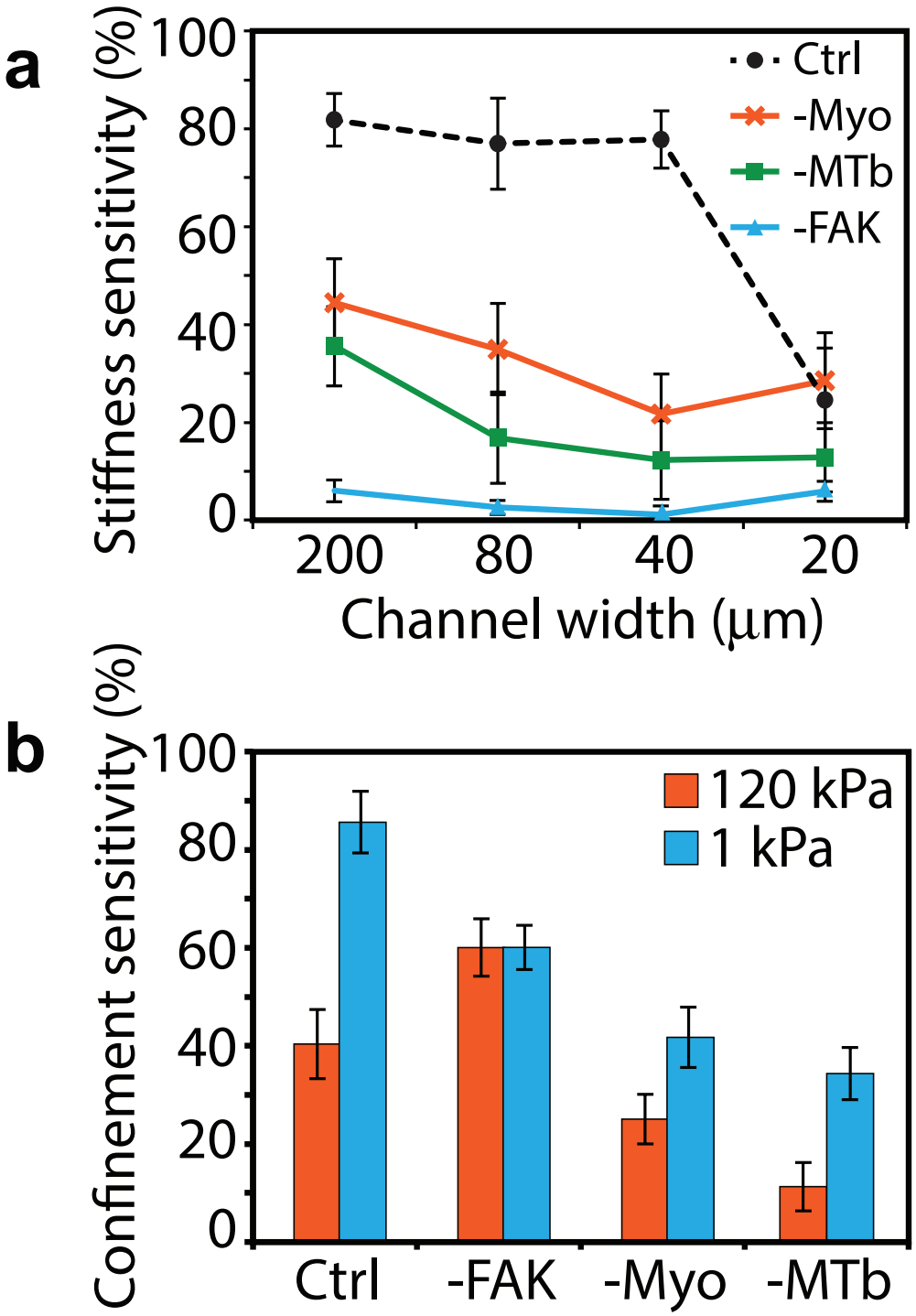

Figure 2.10: **Sensitivity of E-cad localization to extracellular inputs.** (a) Stiffness sensitivity, calculated as the percentage difference in E-cad localization in stiff and soft ECMs, for any given channel width or knockdown state. (b) Confinement sensitivity, calculated as the percentage difference in E-cad localization in wide and narrow channels, for any given stiffness or knockdown state.

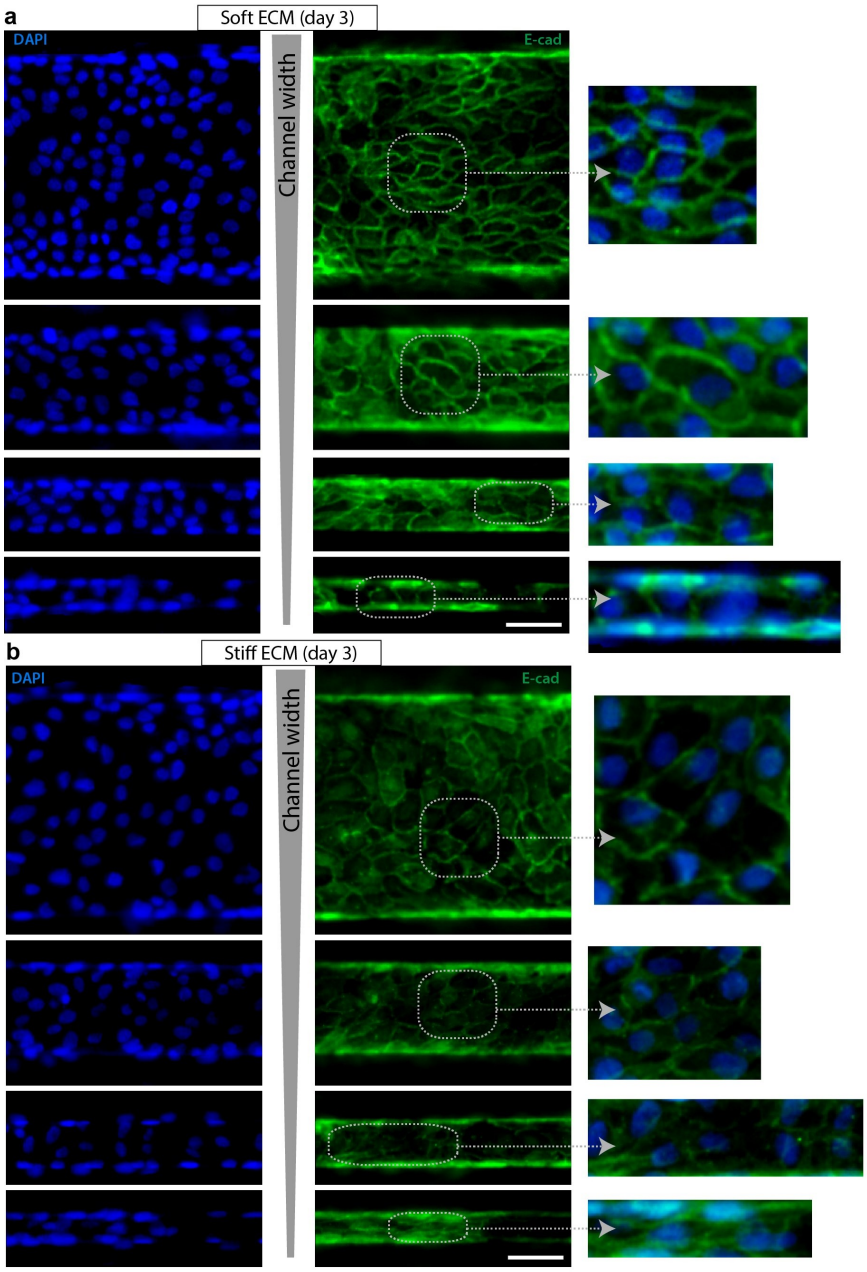

Figure 2.11: **Split images of E-cad and DAPI distributions after day 3.** Immunofluorescence images of E-cad and DAPI distributions, corresponding to the merged images in Fig. 2.4, after 3 days of culture inside channels made of (a) soft and (b) stiff PA gels, with channel widths between 20-200 μm. Scale bar = 50 μm.

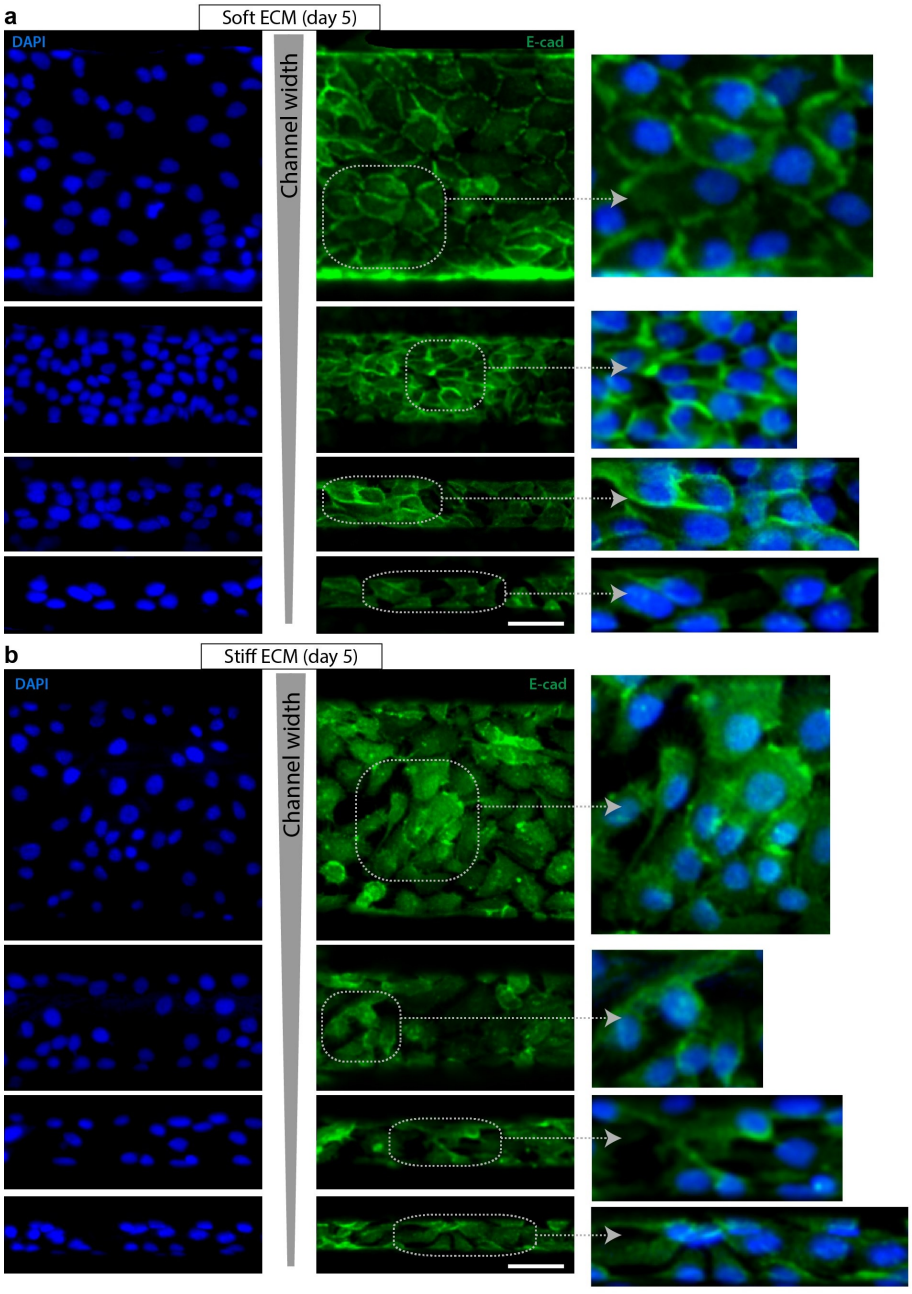

Figure 2.12: **Split images of E-cad and DAPI distributions after day 5.** Immunofluorescence images of E-cad and DAPI distributions, corresponding to the merged images in Fig. 2.4, after 5 days of culture inside channels made of (a) soft and (b) stiff PA gels, with channel widths between 20-200 μm. Scale bar = 50 μm.

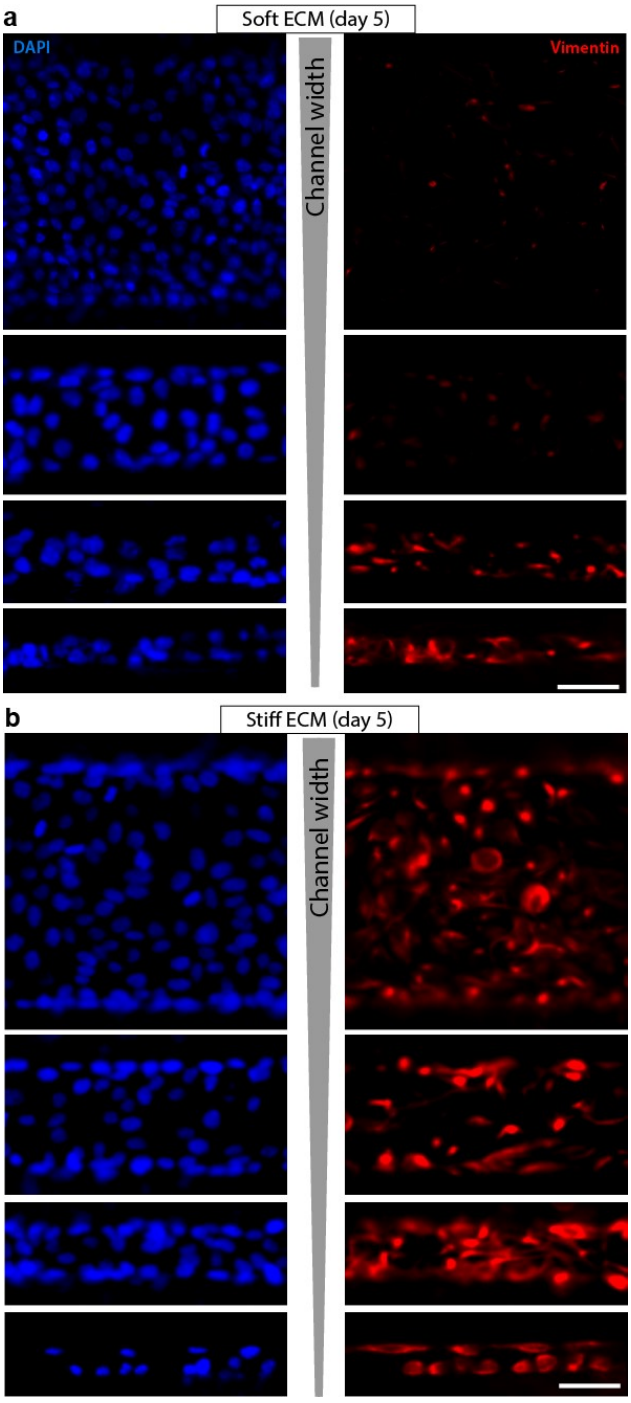

Figure 2.13: **Split images of vimentin and DAPI distributions after day 5.** Immunofluorescence images of vimentin and DAPI distributions, corresponding to the merged images in Fig. 2.5, after 5 days of culture inside channels made of (a) soft and (b) stiff PA gels, with channel widths between 20-200 μm. Scale bar = 50 μm.

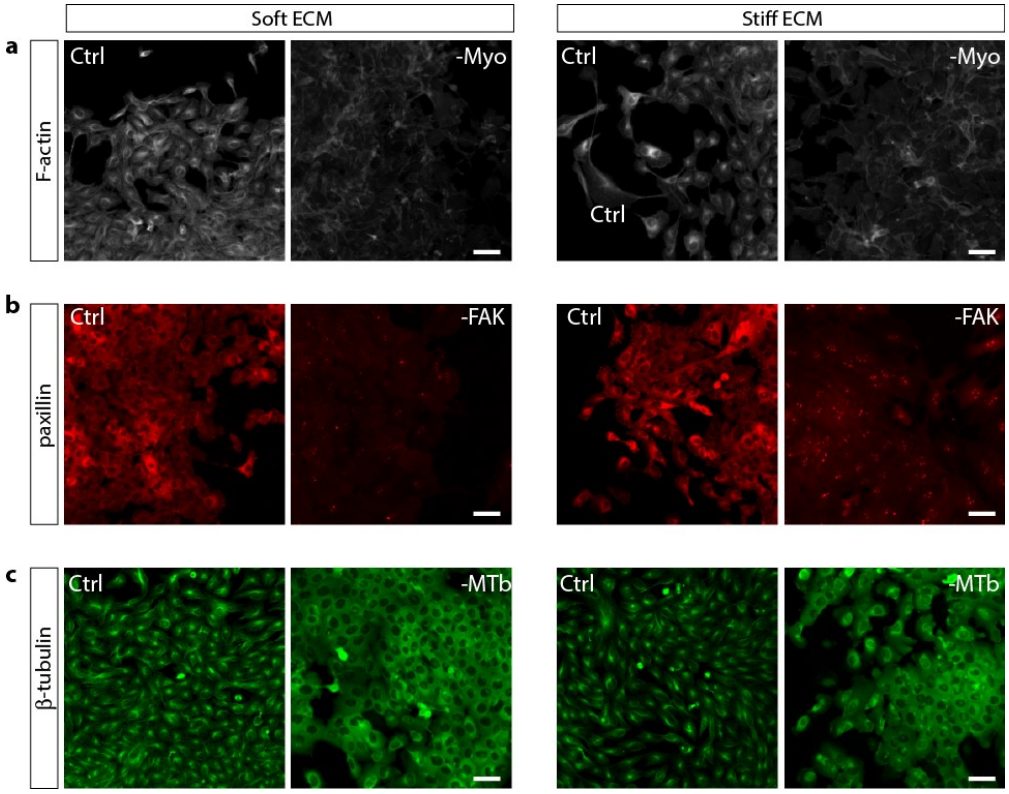

Figure 2.14: **Effects of myosin, microtubule, or FAK inhibition.** Immunofluorescence images of (a) F-actin for control and myosin-inhibited cells, (b) paxillin for control and FAK-inhibited cell, and (c) μ-tubulin for control and microtubule-inhibited cells seeded on soft (1 kPa) and stiff (120 kPa) PA gel substrates. Scale bar = 50 μm.

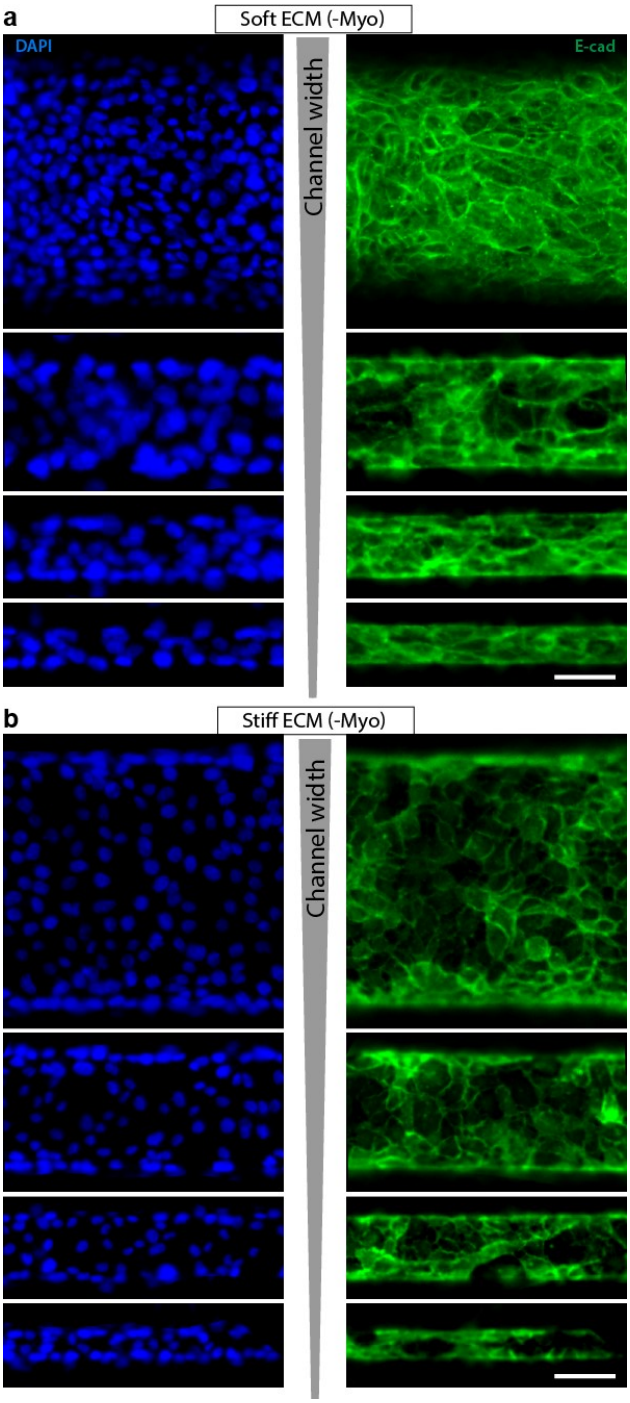

Figure 2.15: **Split E-cad and DAPI images after myosin inhibition.** Immunofluorescence images of E-cad and DAPI distributions, corresponding to the merged images in Fig. 2.7, after myosin inhibition inside channels made of (a) soft and (b) stiff PA gels, with channel widths between 20-200 μm. Scale bar = 50 μm.

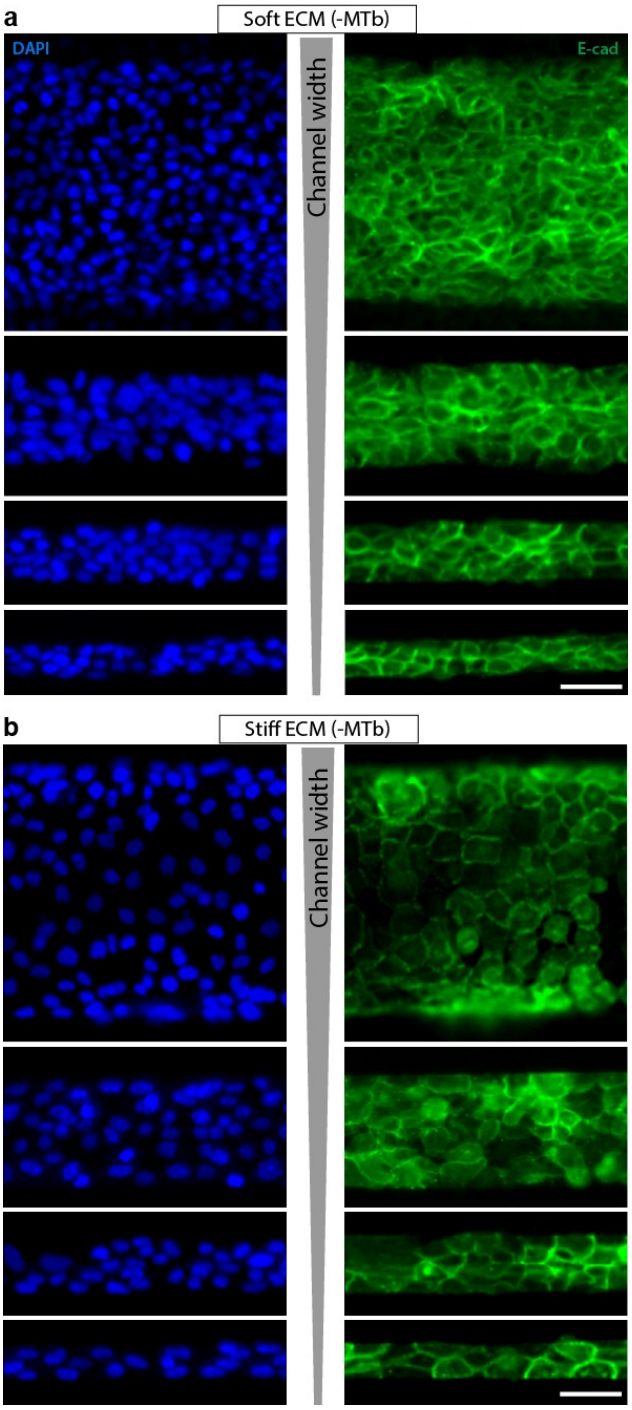

Figure 2.16: **Split E-cad and DAPI images after microtubule inhibition.** Immunofluorescence images of E-cad and DAPI distributions, corresponding to the merged images in Fig. 2.7, after microtubule inhibition inside channels made of (a) soft and (b) stiff PA gels, with channel widths between 20-200 μm. Scale bar = 50 μm.

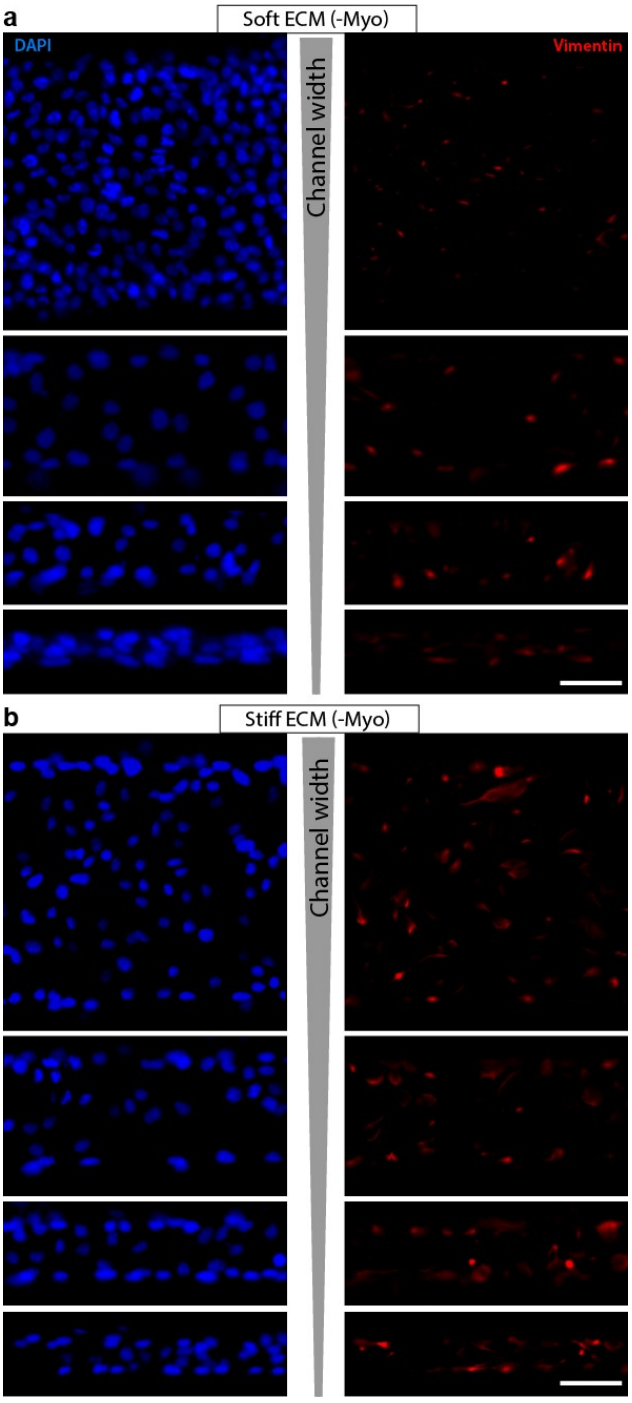

Figure 2.17: **Split vimentin and DAPI images after myosin inhibition.** Immunofluorescence images of vimentin and DAPI distributions, corresponding to the merged images in Fig. 2.8, after myosin inhibition inside channels made of (a) soft and (b) stiff PA gels, with channel widths between 20-200 μm. Scale bar = 50 μm.

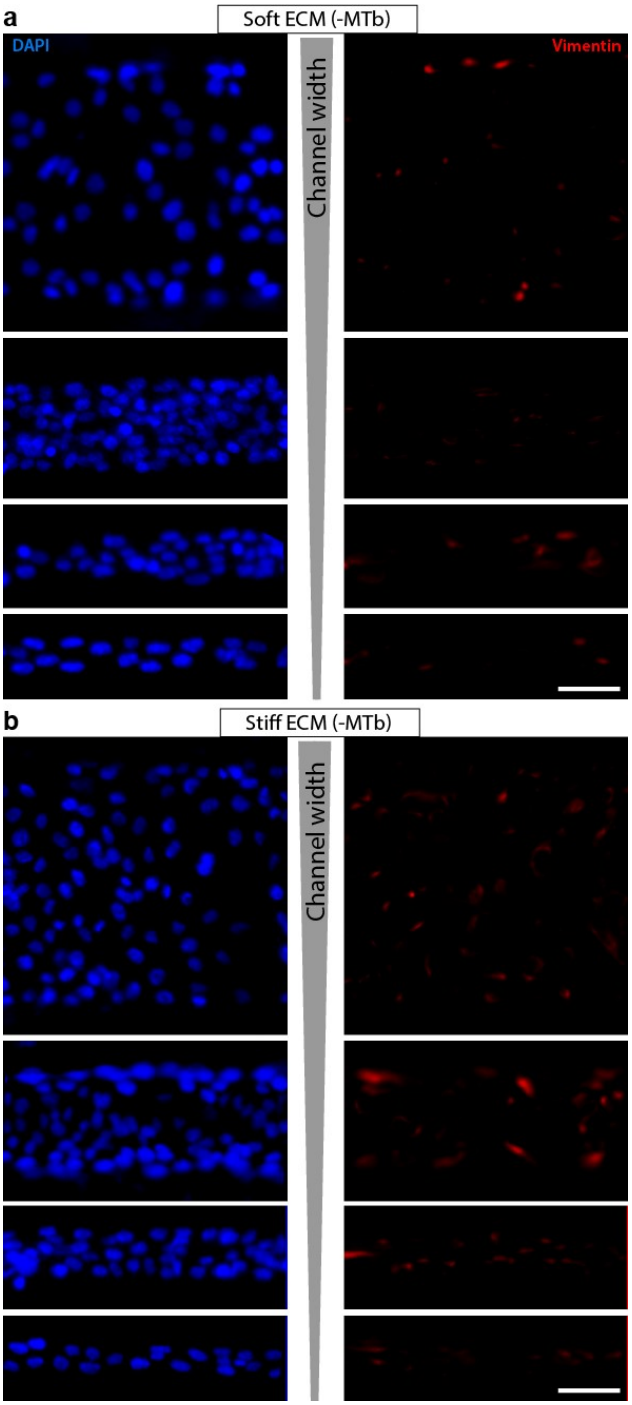

Figure 2.18: **Split vimentin and DAPI images after microtubule inhibition.** Immunofluorescence images of vimentin and DAPI distributions, corresponding to the merged images in Fig. 2.8, after microtubule inhibition inside channels made of (a) soft and (b) stiff PA gels, with channel widths between 20-200 μm. Scale bar = 50 μm.

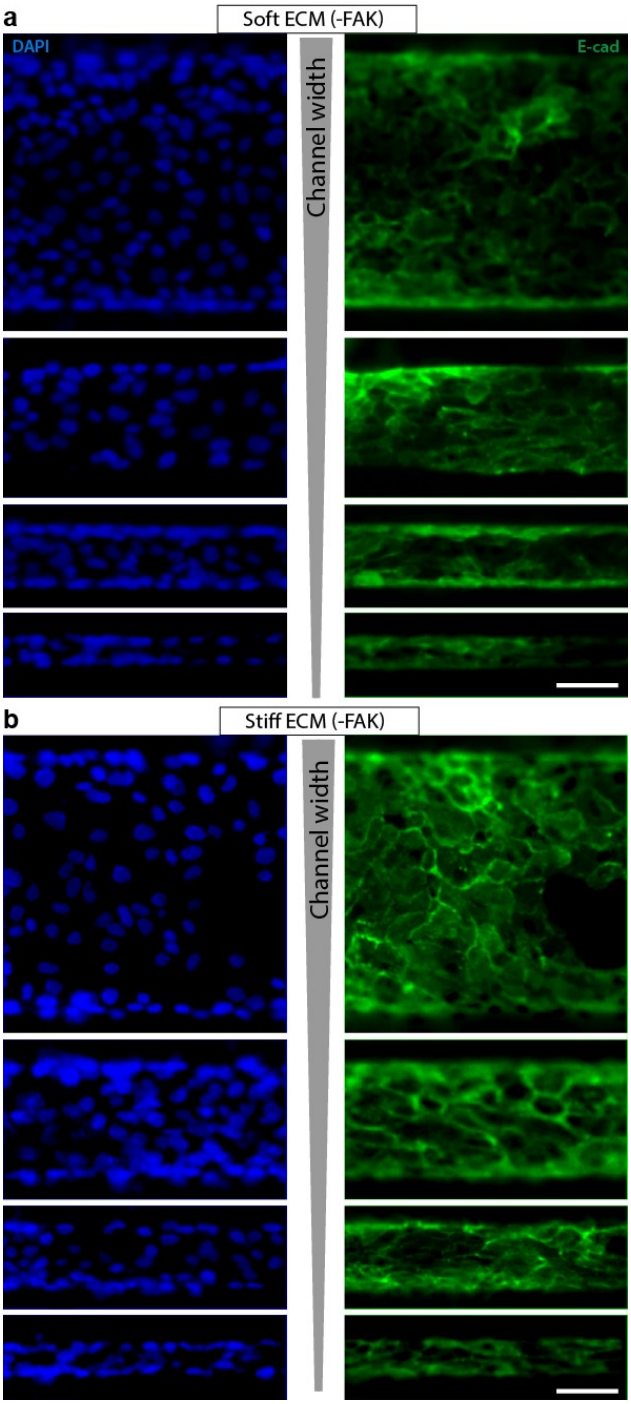

Figure 2.19: **Split E-cad and DAPI images after FAK inhibition.** Immunofluorescence images of E-cad and DAPI distributions, corresponding to the merged images in Fig. 2.9, after FAK inhibition inside channels made of (a) soft and (b) stiff PA gels, with channel widths between 20-200 μm. Scale bar = 50 μm.

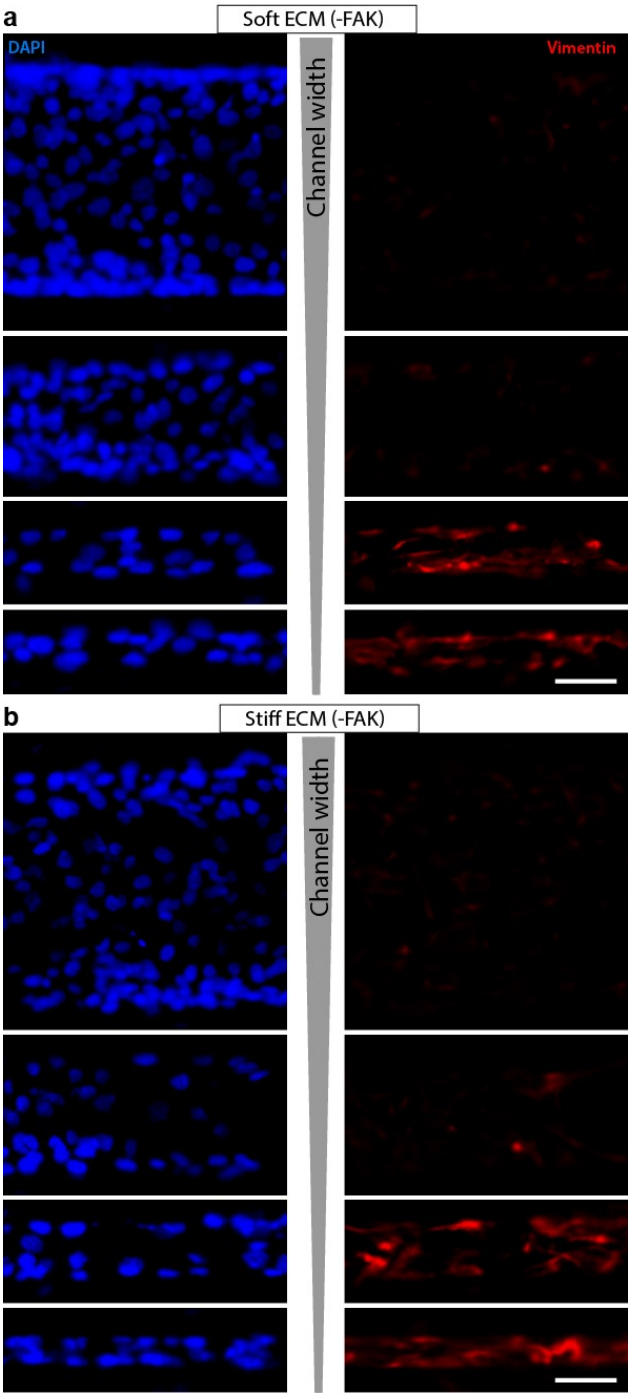

Figure 2.20: **Split vimentin and DAPI images after FAK inhibition.** Immunofluorescence images of vimentin and DAPI distributions, corresponding to the merged images in Fig. 2.9, after FAK inhibition inside channels made of (a) soft and (b) stiff PA gels, with channel widths between 20-200 μm. Scale bar = 50 μm.

Chapter 3

Cellular mechanosensing and migration in confinement

3.1 Summary

Physical interactions of living cells with their microenvironment mediate crucial biological processes, including cell motility, growth, differentiation, and tissue organization. At the interface of the cell and the extracellular matrix (ECM), numerous parameters that define three-dimensional ECMs (e.g. stiffness, porosity, and fibrous microstructure) all interactively affect cell behavior through a variety of sub-cellular mechanisms. This meshwork of cells and ECMs is further complicated by spatial heterogeneity of the ECM across scales, where biomechanical features of the microenvironment in the immediate proximity of the cells are distinct from those governing bulk-scale tissue mechanics. While a wealth of knowledge about cell matrix interaction inside 3D matrices has been generated in recent years,

there exists a gap in our understanding of how specific ECM conditions regulate mechanosensitive cell response because existing studies utilize matrix systems that concurrently alter several matrix properties at once. Furthermore, it is unclear how cell behavior is regulated by ECM biomechanics that varies differentially at macro and micro-scopic length scales. These limitations in existing 3D material scaffolds have also prevented us from gaining a clear understanding of how subcellular molecular signaling pathways contribute to processing mechanical and microstructural cues in the 'multiscale' ECM. For systematic dissection of this intricate coupling among various ECM properties and subcellular machinery, novel material scaffolds are needed that permit orthogonal and well-controlled manipulation of ECM biomechanics and microstructure on both macro and micro scales. Understanding the intricate mechanosensitive cell-matrix interactions inside complex 3D settings represents an important problem for the field of cell mechanics, and development of such experimental frameworks would advance our understanding of both the fundamental aspects of cell motility in 3D-like environments and the biophysical regulation of crucial problems of disease and development. The results presented in the previous chapter have shown that epithelial cell colonies can respond to both matrix stiffness and confinement in an orthogonal manner and undergo EMT and scattering. These findings point to a sophisticated mechanism of cellular sensitivity to matrix topography, which may be relevant in overall mechanosensation and cell migration. To dig deeper into these unexplored ideas, we pose three specific questions in this chapter:

1. Part A: How do matrix stiffness and confinement regulate the mechano-activation of cells?

2. Part B: How do macro and micro-scale matrix properties independently regulate cell motility in confinement?

3. Part C: Can matrix confinement reveal new modes of collective migration of mixed populations of epithelial cells?

3.2 Part A: Matrix stiffness and confinement influence YAP localization in clustered epithelial cells

3.2.1 Introduction

Cells sense their microenvironment not only through biochemical signals, but also through physical and mechanical cues present in the extracellular matrix (ECM). These mechanical cues are mainly attributed to ECM stiffness, topography, dimensionality, and porosity [3,37], all of which are known to regulate fundamental cellular functions such as proliferation, migration, and differentiation [4, 8, 20, 40–42]. In recent years, growing evidence suggests that there is a direct link between various nuclear transcription factors and mechano-regulated cell activities [43, 44]. In particular, Yes-associated-protein (YAP) is recognized as the classical sensor that transduces mechanical signals, including ECM stiffness and cell shape, into biological outcomes [36]. These mechanosensitive functions of subcellular YAP localization are processed through the Hippo signaling pathway, which acts upstream of YAP. Upon activation of the Hippo pathway, large tumor suppressor homologue (LATS) gets phosphorylated, resulting into YAP phosphorylation [45]. The inactivated (phosphorylated) YAP is excluded from the nucleus and aggregated within the cytoplasm [46]. However, the inactivated form of Hippo pathway leads to de-phosphorylation of YAP and re-localization to nucleus to induce gene expression [47,48]. Therefore, the shuttling of YAP between the nucleus and cytoplasm

serves as a key mechanism through which mechanical cues are transduced to gene expression [49].

Several recent studies have demonstrated a direct relationship between ECM stiffness and the nuclear YAP activation in various cells types when cultured singly on substrates of variable stiffness [50–53]. On stiff fibronectin-coated polyacrylamide (PA) gels, mammary epithelial cells (MECs) and human mesenchymal stem cells (hMSCs) showed predominantly nuclear YAP localization. However, on soft substrates, the cytoplasmic localization was the dominant phenotype [36]. The YAP activation is also associated with osteogenic differentiation of hMSCs on stiff substrates [36, 53]. In fibrosis, higher matrix stiffness activates fibroblasts to enhance the rate of matrix synthesis, where YAP is known to be the key mediator of stiffness-dependent fibroblast activation in pulmonary fibrosis [54, 55]. Moreover, the enhanced YAP localization on stiff substrates is correlated with the higher cell spreading area [36]. Strikingly, the restriction of cell spreading led to more cytoplasmic YAP localization [56]. Although a direct correlation between substrate stiffness and cell shape with YAP activation has been identified for single cells, there is not enough evidence regarding the mechano-regulated YAP localization in epithelial clusters. In this study, we investigate three key questions regarding YAP activity in epithelial cell clusters (1) How does the ECM stiffness influence YAP distribution in epithelial clusters? (2) How does the cell density in epithelial clusters affect YAP activation on 2D soft and stiff matrices? (3) How does ECM confinement regulate YAP activity in epithelial clusters in soft and stiff matrices? Given that epithelial cell clusters of irregular densities often reside in ECMs that vary in both stiffness and topography, it is crucial to understand how mechanosensitive YAP activity varies with the degree of confinement surrounding such cell clusters.

To understand how matrix stiffness regulates YAP localization in clustered epithelial cells, we cultured MCF-10A human mammary epithelial cells on collagen-coated flat PA gels of variable stiffness. Our results demonstrate for the first time that stiffness-dependent YAP activation holds true for epithelial cell clusters, similar to the effects previously observed for single cells [36]. While cell density is known to influence YAP activation, it is not clear how cell density affects the stiffness-dependent YAP localization in epithelial clusters. Our results indicate that the density of epithelial cells minimally affects YAP localization on soft ECMs. However, on stiff ECMs, the nuclear YAP localization rises with lower cell density. Next, to investigate the role of ECM confinement in regulating YAP activation in epithelial clusters, we need a device that permits independent control over matrix stiffness and topography. Here, we employed a microchannels-based matrix scaffold with tunable stiffness and confinement. We examined subcellular YAP localization for epithelial clusters trapped inside the channels of varying width and stiffness. We found that the nuclear YAP localization increased in narrower channels. Our results indicate that reduced cell roundness, due to increased confinement, accompanies YAP activation in narrower channels. Surprisingly, the enhanced nuclear YAP in more confined environments persisted even in soft ECMs, which were previously shown to have inhibitory effect on YAP activation. Taken together, our findings expand the understanding of ECM stiffness-dependent and cell-shape dependent YAP activation in the context of clustered epithelial cells.

3.2.2 Results

ECM stiffness regulates nuclear YAP localization in epithelial cell clusters

To test if YAP activity in clustered epithelial cells is regulated by ECM stiffness, we measured nuclear localization of YAP in MCF-10A cells grown on collagen-coated PA gels of either 1kPa or 120kPa elastic modulus. Following 3 days of culture in these substrates, substrates were stained for the YAP antibody. Through the analysis of immunofluorescence images, we measured nuclear/cytoplasmic ratio of YAP expression for individual cells within epithelial cell sheets grown on soft or stiff substrates (Fig. 3.1B). We found that the average nuclear localization of YAP, calculated as mentioned above, in the case of soft ECM was less than 1/5th of the value calculated for stiff ECM. These results indicate that ECM stiffness-dependent nuclear translocation of YAP that has been observed for single cells also holds true for multi-cellular epithelial sheets.

Stiffness-dependent YAP activity depends on the cell density of epithelial clusters

Cell density is known to regulate Hippo signaling and nuclear YAP accumulation [56]. At low cell densities, weak Hippo signaling allows nuclear YAP accumulation, whereas culturing cells at high density induces strong Hippo signaling and the inhibition of nuclear YAP accumulation [56]. However, it remains unknown whether such cell density dependent YAP activity differs on soft and stiff matrices. To answer this question, we seeded MCF10A cell colonies at either low density of 25,000 $cells/cm^2$ or high density of 75,000 $cells/cm^2$ on both soft and stiff PA gels and imaged YAP expression (Fig. 3.2B). Subsequently, we measured

nuclear YAP localization in terms of the nuclear/cytoplasmic ratio of YAP expression, as described earlier. On soft substrates (Fig. 3.2A,B), the difference in nuclear YAP localization between low (2.5×10^5 $cells/cm^2$) and high (8.5×10^5 $cells/cm^2$) cell density conditions was small and statistically insignificant. However, on stiff ECMs (Fig. 3.2C,D), we observed an approximately 80% reduction in nuclear YAP localization in densely packed cells (5.5×10^5 $cells/cm^2$) compared to the cell clusters with lower density (1.5×10^5 $cells/cm^2$). On gels of an intermediate stiffness, 55kPa, the YAP activity was similar to that observed on the stiff, 120kPa, substrates (Fig. 3.7). Going forward, all measurements for 'stiff' ECMs are conducted on the 120kPa gels. In all measurements, the numbers corresponding to cell densities are average densities evaluated by counting the number of cells from the DAPI images for each condition. In both soft and stiff cases, the final 'high' cell density is at least three-times the 'low' density. Note that the final cell densities on soft and stiff ECMs are different because we found a sparser distribution of cells on the stiffer ECM, which could be due to increased mechano-sensitive spreading and EMT [57–59]. These results indicate that the density of cells in an epithelial cluster significantly influenced the mechanosensitive YAP localization when epithelial cells were grown on stiff substrates.

Matrix confinement regulates YAP localization through changes in cell morphology

To study the independent roles of stiffness and confinement on YAP activation in epithelial clusters, we fabricated a polyacrylamide microchannel-based matrix platform for cell culture (Fig. 3.3A), as we have done previously [57]. Briefly, we combined photolithography techniques and PA hydrogel synthesis to construct microchannels of varying width, embedded

in PA gels of specified stiffness. In this system, an epithelial colony is seeded in the central chamber and allowed to grow beyond the central chamber to facilitate the entry of cell clusters into channels of widths ranging between 20-200 μm. Thus, our platform allows independent control over confinement and stiffness around epithelial clusters. Cells with flat and spread morphology have been shown to exhibit nuclear YAP localization, while rounded cell morphology favors YAP cytoplasmic localization [56]. Given that cell morphology is associated with the subcellular YAP localization, we hypothesized that morphological adaptation of epithelial cells to confinement might also influence YAP distribution. First, to measure the effect of confinement on cell morphology, we quantified roundness of individual cells in epithelial clusters in channels of varying confinement and stiffness. As Fig. 3.3B shows, the roundness parameter is decreased with increasing confinement (decreasing channel width). We also found that the cells on soft substrate were rounder compared to the ones on stiff substrate regardless of the channel width. These results demonstrate that confining of epithelial clusters within narrow channels reduces the roundedness of individual cell that make up the epithelial cluster (Fig. 3.3B).

Next, we asked whether this change in the cell morphology accompanies a confinement-regulated YAP distribution in epithelial clusters. We examined YAP activation in epithelial clusters confined inside channels of defined properties by performing confocal microscopy and quantifying the percentage of cells with nuclear YAP localization after 5 days of cell seeding. In the widest channels (channel width of 200 μm), which are essentially the same as flat gels except with the side walls that restrict the cluster size (Fig. 3.3C), we compared nuclear YAP localization for clusters located in the proximity of the channel walls with those located inside the channels (Fig. 3.3C). We saw more nuclear YAP localization close to the channel walls in both soft and stiff substrates. Therefore, presence of confinement changes YAP distribution even in the wide channels compared to flat substrates. In both 80 and 200

μm soft channels, cell clusters showed $\sim$25% increase in nuclear YAP along the channel wall compared to the clusters farther away from the walls (Fig. 3.3C). In the channels made of soft ECM, the difference in YAP activation between near and away from channel walls was even higher as compared to the difference measured in stiff channels.

Greater nuclear YAP localization in stiffer and more confined ECMs

Given the previously described dependence of YAP localization on cell morphology [56] and our measurements of the influence of channel width on cell morphology (Fig. 3.3B), we examined the effect of confinement on YAP distribution inside the channels made of soft or stiff ECMs. Since cell density influenced mechanosensitive YAP activity on flat 2D substrates (Fig. 3.2), we first posited whether a similar density-dependence could occur in confined ECMs. Surprisingly, we found that nuclear YAP localization did not change significantly between low and high cell density conditions for any given channel width or ECM stiffness (Fig. 3.4). These results indicate that YAP activity in epithelial clusters in confinement is less sensitive to cell density as compared to the epithelial colonies on flat substrates (compare Figs. 3.2 and 3.4).

Inside soft channels, we found that nuclear YAP localization increased with decreasing channel width (for either cell density), which indicated a rise in YAP activation in more confined ECMs (Figs. 3.4, 3.5B). The epithelial clusters confined inside narrow (20 μm) channels showed an approximately three-fold increase in nuclear YAP localization compared to ones located in the wide (200 μm) channels (Fig. 3.4). Next, to examine the effect of ECM stiffness on YAP activation in confinement, we repeated these experiments in channels made of stiff (120 kPa) PA gels. As expected, the cell clusters inside the stiff channels showed relatively high nuclear localization regardless of the channel width (Figs. 3.4, 3.5A). Overall,

in stiffer channels, we found higher nuclear YAP compared to soft substrates for any given channel width. Thus, our results demonstrate that higher matrix elasticity regulates nuclear YAP localization even for epithelial clusters trapped inside channels, which is in agreement with earlier observations on flat PA gels [36]. YAP-regulated mechanosensation is mediated through the actin cytoskeleton, which determines cell morphology [10, 36]. Therefore, we hypothesized that disruption of the integrity of the actin fibers may hinder the morphological adaptation of clustered epithelial cells and consequently inhibit a confinement-induced nuclear YAP localization. We treated MCF10A cells with LatA, which is a known inhibitor of actin polymerization. Analysis of YAP subcellular localization demonstrated that such pharmacological disruption of F-actin polymerization significantly reduces nuclear YAP localization in epithelial clusters, regardless of the ECM stiffness and confinement (Fig. 3.6), compared to untreated cells (Fig. 3.5). After F-actin inhibition, the YAP activity in cells did not show any sensitivity to ECM confinement or stiffness (Fig. 3.6C).

3.2.3 Discussion

Mechanical signals are abundantly present in the microenvironment that surrounds the living cells. In recent years, there has been an increasing appreciation that the mechanical properties of the ECM, such as stiffness and matrix topography, impact fundamental cellular functions through cell-ECM interactions. In cancer metastasis, epithelial clusters escape from the primary tumor and pass through ECMs of varying mechanical properties before arriving at the secondary sites. It is now known that the elasticity and microstructure of the ECM surrounding the epithelial clusters can independently prepare these cells for malignant transformation [10, 12, 29, 57]. Specifically, on stiffer substrates, higher actomyosin contractility and stronger cell-ECM adhesions lead to the dissolution of cell-cell adhesions,

resulting in epithelial-to-mesenchymal transition (EMT) [10]. Recent studies, including our work, have shown that MCF10A mammary epithelial cells cultured on stiff collagen-coated PA gels undergo EMT and attain invasive phenotype [12, 57]. Additionally, we have shown that ECM topography can perpetuate mesenchymal transformation independently of matrix stiffness [57], which was consistent with previous findings [29]. We also found that the elongated cell morphology in narrower channels was associated with a confinement-sensitive induction of EMT, even in softer ECMs [57].

In this study, we hypothesized that the ECM-dependent response of clustered epithelial cells [57] due to the mechanical cues presented by the ECM are processed by signaling pathways transmitted through the nucleus. Since YAP is known as the classical transducer of ECM stiffness [36, 56], we shortlisted it as a potential candidate for instructing ECM-sensitive responses in epithelial clusters. While it is known that ECM stiffness and cells shape can regulate YAP distribution in single cells, it is not yet clear how these parameters might affect YAP localization in epithelial cells that typically grow in clusters with intact cell-cell junctions. Given that the disassembly of tight junctions is known to enable ZO2-mediated translocation of YAP to the nucleus, it would be important to understand the regulation of YAP activity during ECM-dependent EMT [60]. Current understanding of stiffness-dependent YAP activation has mainly been derived from experiments of cells cultured on flat surfaces. This gap in knowledge persists mainly because of an absence of matrix platforms that permit an orthogonal control over confinement and stiffness of the ECM around the epithelial clusters. In this work, we addressed this challenge by utilizing a matrix platform for culturing cell clusters in PA channels of varying width and stiffness [57]. Our soft microchannels-based platform allows new measurements of YAP distribution in epithelial clusters in ECMs of defined stiffness and confinement.

We have shown for the first time that matrix confinement alters the dependence of YAP activation on ECM stiffness. Although previous studies have indicated that YAP remains inactive on soft substrates [36, 55], our results demonstrate that confining the epithelial clusters inside the narrow channels can lead to nuclear YAP localization even on soft ECMs. On stiff substrates, most cells in the cluster showed maximal YAP activation regardless of the channel width. Here, cells confined within narrow channels were forced to become less round, which was similar to the cellular elongation and simultaneous nuclear YAP localization observed on flat stiff substrates [56]. Even in wide channels, cells near the channel walls showed higher nuclear YAP localization than those in the interior of the epithelial cluster. It is possible that cells near the channel walls intimately interact with the wall surface and align themselves along the walls. This rise in spreading and elongation along the channel walls may enhance cellular mechano-activation, as we have argued in previous studies [4,20,57,59], and thus lead to higher YAP activation. Thus, increased YAP activity may arise due to either stiffer or more confined ECM, both of which are also associated with increased cell elongation. The results presented in this study, along with our previous findings [57, 59], have revealed that both ECM stiffness and confinement can independently induce EMT and enhance YAP activity in epithelial clusters.

We have also shown that nuclear YAP localization increases in sparser epithelial clusters cultured on 2D substrates, which is in agreement with another recent study [58]. Notably, we report that denser epithelial clusters exhibit lower YAP activity even on stiff ECM. However, our measurements for epithelial clusters inside channels of varying width show that the density-dependent YAP activity does not hold true in confined ECM settings. It should be noted that the presented framework of ECM- and density-dependent YAP activity in epithelial clusters has only been tested for an immortalized epithelial cell line (MCF-10A) and could potentially differ in other cell lines and primary cultures. It is likely that the

influence of ECM confinement on YAP activity in clustered cells might also regulate cellular behaviors other than EMT, such as migration and differentiation, for a variety of cell types and matrices that have not been covered thus far.

3.2.4 Materials and Methods

Polyacrylamide gels – flat and microchannels

To prepare flat hydrogels, 18mm glass coverslips were plasma cleaned, treated with Bind-Silane (GE Healthcare), rinsed with ethanol, and air-dried. The PA precursor solutions were mixed by choosing monomer:crosslinker ratios based on previous stiffness characterizations of PA gels – acrylamide:bisacrylamide (A:B) percentages of 5%A:0.2%B and 15%A:1.2%B, corresponding to PA elastic moduli of 1 and 120 kPa [4]. To make flat PA gels, the precursor solution was sandwiched between a reactive coverslip and a glass slide coated with Sigma-cote (Sigma-Aldrich), and let to polymerize for 30 min. To fabricate hydrogel-microchannel PA gels, a mixed solution was polymerized against the silicon wafers, made using a photolithography technique described previously [57]. Polymerized gels and microchannels were soaked in PBS and stored at 4°C until use. Gels surfaces were functionalized with 0.5mgml-1 Sulfo-SANPAH (Thermo Scientific Pierce) in HEPES buffer under 365 nm ultraviolet light for 10 min, and incubated at 4 ℃ overnight with 0.05mg/ml of rat tail collagen I (Santa Cruz Biotechnologies).

Cell culture

Human mammary gland epithelial (MCF-10A) cells were cultured, in DMEM/F12 (Invitrogen), with 5% (v/v) horse serum (Invitrogen), 20 ng/mL epidermal growth factor (EGF, Miltenyi Biotec Inc), 0.5 mg/mL hydrocortisone (Sigma-Aldrich), 100 ng/mL cholera toxin (Sigma-Aldrich), 10 μg/mL insulin (Sigma-Aldrich), and 1% (v/v) penicillin-streptomycin (Sigma-Aldrich). A colony of MCF10A cells was seeded inside the central chamber of a PA hydrogel -microchannel device, as described previously [57], and allowed to grow out of the chamber and enter into the channels. To culture cells on flat gels, media containing enough MCF-10A cells to generate low and high density of epithelial cells was added to each well and incubated for 3 days at 37 ℃ and 5% CO2. Samples were fixed with 4% paraformaldehyde (Santa Cruz Technologies) in PBS, followed by permeabilization of cell membrane with 0.5% Triton-X 100 (Sigma-Aldrich) and blocking with 1% bovine albumin serum (BSA) (EMD milipore). Samples were incubated with mouse monoclonal YAP antibody (Santa Cruz Biotechnology; diluted 1:100) overnight followed by incubation with Alexa Fluor 488-labeled goat anti-mouse antibody (Invitrogen; diluted 1:500) for 1 hour. After thoroughly rinsing the substrates with PBS, 1:250 10mg/mL DAPI (Santa Cruz) was added for 30 min at RT. Finally, samples were rinsed again with PBS and stored at 4 ℃ before imaging.

Confocal microscopy and quantification of YAP localization

Images were taken using a laser-scanning confocal microscope (Zeiss LSM 730; Carl Zeiss MicroImaging, Germany) at 20X objective, and confocal stacks were obtained. Captured z-stacks were imported to ImageJ (NIH), and the stacks were projected with the maximum intensity. To quantify the subcellular YAP activity, the average fluorescence intensity was

measured in the nucleus and the cytoplasm. Next, the nuclear/cytoplasmic ratio of YAP expression was plotted. As an alternative method, cells were examined for the nuclear inclusion/exclusion and the percentage of each type of YAP localization calculated by finding the number of cells representing the corresponding YAP localization category (nuclear or cytoplasmic) [61].

Statistical analysis

Images used for analysis were selected randomly from at least three different experiments for each condition. Results are reported as the mean + standard error (SE), unless stated otherwise. To identify the significant differences between experimental conditions, we used two-way ANOVA followed by Tukey-Kramer HSD (honestly significant difference) for pair-wise comparisons in MATLAB (Mathworks). Differences were considered to be significant for $P<0.05$.

3.3 Part B: Dissecting the regulatory roles of micro- and macro-scale matrix parameters on cell motility in confinement

3.3.1 Introduction

It is becoming increasingly evident that the biomechanics of the extracellular microenvironment strongly regulates cell behavior [4, 37]. While significant efforts are being made to

understand how the microenvironment affects cell behavior, in reality, cells are surrounded by layers of cell-ECM meshwork that significantly vary in mechanical properties over different length scales. As depicted in Fig. 3.8, mesenchymal cells migrating through connective tissue tend to be embedded in a fibrous ECM and supported in bulk by a different matrix of larger length scales, where the macro-structural context is provided by the epithelium, basement membrane and aligned ECM fibers [62]. Among other examples of cell migration through heterogeneous tissue, glioblastoma brain tumor cells are known to metastasize to distant sites within the brain by migrating along highly aligned white matter tracts or lymphatic vessels whilst simultaneously remodeling and deforming their surrounding microenvironment [63–65]. Thus, both micro-scale ECM of the brain and the macro-scale properties of the aligned tracts would influence glioma cell invasion, and it would be highly insightful to further dissect the roles that individual ECM properties play across length scales in regulating this ECM-dependent tumor invasion. On cellular scale, the interaction between ECM fibers and cell surface receptors allows the cells to sense and support mechanical cues present in the ECM [66], while the macro-scale ECM provides another level of structure to support this micro-scale cell-ECM interaction. The bulk matrix dictates material properties such as bulk pores for entire cell body and bulk deformability of the ECM. On the other hand, the microscale ECM immediately surrounding the cells governs subcellular porosity, adhesivity and local ECM deformability in various regions of the cell. This multiscale heterogeneity of the ECM may fundamentally influence how cells navigate complex tissue barriers and move to distant sites. While most existing in vitro cell culture scaffolds effectively mimic micro-scale ECM properties in 3D, the stiffer components of the bulk matrix are generally left out. For example, when cell invasion through 3D collagen gels is studied in vitro, the tissue equivalent of the matrix layers surrounding the fibrous collagen mesh is missing from the mechanical make up of existing collagen-based in vitro systems. As we strive to gain

a comprehensive understanding of ECM-dependent cell motility in 3D, it is crucial to delineate the importance of matrix length scales in how specific ECM properties regulate cell migration. As cells navigate tissue barriers, microscale mechanical cues present in the fibrous ECM surrounding the cells profoundly regulate cell behavior. While micro-scale biophysical properties of ECM fibers regulate crucial cellular and subcellular mechanisms relating to adhesion, contractility, proteolysis and overall cell motility, the macroscale matrix surrounding the cell provides higher order of ECM stiffness and porosity. Thus, in a multiscale setting, the scope of studied biophysical properties of the ECM should not only be limited to the 'type' of ECM properties (stiffness and confinement) but also to the applicable length 'scale' (micro or macroscopic) for each applicable property. To address this challenge, we adopted our previously developed PA-microchannel hydrogel platform with independent control over matrix stiffness and confinement defining the macro-scale ECM properties. Subsequently we inject a solution of collagen I of defined concentration into the microchannels to control the microscale ECM properties. This will provide a 'tissue-like' microenvironment which is known to be fibrous and collagen rich, in the immediate vicinity of the cells. Thus, layers of collagen and PA matrices of distinct material properties around the cells emulate heterogeneous extracellular environment present in vivo, which in turn allow us to interrogate the roles of 'multiscale' ECM parameters on cell motility. Our findings demonstrate that NIH3T3 fibroblast embedded with higher concentration of collagen are less sensitive to the surrounding macroscale ECM properties. However, in the vicinity of less concentrated collagen network, cells respond to properties of the underlying matrix stiffness and channel size. Cell migrated significantly slower and demonstrated less directional migration when seeded within soft PA channels filled with low concentration of collagen I.

3.3.2 Results and Discussion

Fabrication of material scaffolds enabling independent manipulation of microchannel properties in both micro and macroscale

To mimic migration of cells in layered confinement, we fabricated an in vitro matrix platform as a collagen-filled polyacrylamide microchannels-based platform. We modulated the bulk matrix around cells as PA channel arrays analogous to the ones described in chapter 2, in which channel stiffness is determined by the PA formulation and channel geometry is determined by the dimensions of silicon masters used to topographically template the PA. We systematically varied channel specifications at discrete values ranging from 0.4–40 kPa in elasticity and 20–200 μm in channel diameter. To study the role of micro-scale stiffness and the architecture of the fibrous 'tissue-like' ECM, we filled the microchannels, fabricated in the Chapter 2, with varying concentration of collagen I and allowed it to polymerize. This yields a layered collagen-PA gels of both controlled micro and macroscale properties, as depicted in Figs. 3.8. In this system, cells are surrounded by a layered matrix comprising ECM fibers of varying architecture and density, and bulk matrix of varying geometry and stiffness. Here, collagen and PA matrices of distinct material properties around the cells will emulate heterogeneous extracellular environment present in vivo, which in turn will allow us to interrogate the roles of 'multiscale' ECM parameters on cell motility.

Cells surrounded by dense collagen lose the sensitivity to bulk confinement and stiffness.

To investigate the quantitative relationship between cell migration and 'multiscale' ECM stiffness and microstructure on cell migration, we mixed human fibroblast cells (NIH3T3) with collagen solutions of varying concentrations, and injected into the PA channels of defined stiffness and geometry. To isolate the effect of microscale ECM properties on cell motility, we designed two experimental settings. First, cells were mixed with high concentration of collagen I (1.3mg/ml) to emulated the dense collagen architecture. Second, we mixed the cells with low collagen concentration (0.4mg/ml) to measure the effect of bulk ECM stiffness, when cells are embedded in a sparse collagen network. To study cell migration, we performed time-lapse microscopy of cell movement through these collagen-filled PA microchannels for at least 24 hours. Afterwards, we tracked the migration of individual cells to measure the migration speed and persistency. Migration analysis of NIH3T3 cells inside the dense collagen network revealed that when cells are surrounded by higher concentration of collagen network, they showed minimal response to the channel stiffness and confinement. Migration tracks of singles cells are shown in Fig. 3.9, and each track was color-coded according to the migration speed. Specially, we did not see higher migration speed on stiff substrates, compared to soft, as others and we observed in the previous studies, as demonstrated in Fig. 3.10. When cells were embedded in dense collagen network, they are unable to communicate with the bulk matrix as it may be harder for the cell-generated forces to be transmitted to the distant channel walls. Similarly, there was no difference in migration speed relative to channel width, i.e., cells migrated with approximately the same migration speed in all channels sizes (Figs. 3.9,3.10). We also analyzed the persistence of migration of NIH3T3

cells in dense collagen-filled channels. Similar to migration speed, directionality of cells was also independent of the bulk channel stiffness and confinement (Figs. 3.9,3.10).

Enhanced influence of channel stiffness and confinement on cell motility in lower concentration of collagen

When the collagen concentration was reduced to 0.4mg/ml, we observed a rise in the influence of microscale ECM properties on cell behavior. In general, cell embedded in lower density collagen migrated slower when collagen was attached to soft PA gels, regardless of the channel width. In case of soft PA gels, there was an increase in migration speed as the channel width decreased; cells in 20 μm and 40 μm migrated faster compared to 80 and 200 μm channels. Also, cells in narrower channels demonstrated more directional movement compared to those in wide channels, as demonstrated by angle distribution in, Fig. 3.11, and the average directionality, in Fig. 3.12. However, inside stiff channels, we observed faster cell migration and more directional movement compared to soft ECMs regardless of the channel width (Figs. 3.11, 3.12). These results demonstrated that cells embedded in lower density collagen matrix are more responsive to the bulk properties of the ECM (channels in this case) and their response is mostly dictated by the properties of the bulk matrix. In fact, our measurements of cell motility in channels filled with low collagen concentration are analogous to recent observations of fast and highly persistent migration in stiff and narrow channels [4, 20].

3.3.3 Materials and Methods

Cell culture on collagen-filled PA-channels.

NIH 3T3 fibroblasts were cultured in growth media containing low-glucose DMEM (Invitrogen) supplemented with 1% L-glutamin, 1% penicillin/streptomycin, and 10% fetal bovine serum (Invitrogen), and maintained at 37℃ and 5% CO2 during culture. For single cell analysis, NIH 3T3 cells were mixed with the neutralized collagen gel solution before adding to PA-channels. Cell were cultured for up to 3 days in the collagen-filled PA-channels.

Fabrication of collagen-filled PA-channels.

PA-channels were fabricated according to method described in chapter 2. Briefly, Silicon master of defined topographical feature was fabricated using a standard photolithography technique and a PA solution, enough to achieve a 100 μm thick gel, was sandwiched between the microchannels master and a reactive coverslip. The PA precursor solutions were mixed by choosing monomer:crosslinker ratios based on previous stiffness characterizations of PA gels – acrylamide:bisacrylamide (A:B) percentages of 5%A:0.2%B, and 12%A:0.6%B corresponding to PA elastic moduli of 1 and 40 kPa [4, 23]. To ensure binding of the collagen gels to underlaying PA-channels, we functionalized the surface of PA-channels with 1mg/ml of Sulfo-SANPAH (Thermo Fisher Scientific) prepared in 50mM HEPES buffer solution (Santa Cruz Technologies) and crosslinked to the PA-channel surface upon activation with 365nm UV for 10 minutes. After extensive washing with 50mM HEPES buffer, we added collagen-cell mixed solution to each device. Collagen solutions were prepared at two different concentrations, 0.4mg/ml and 1.3mg/ml, refereed to as sparse and dense collagen network in the text. PH of

collagen gel was adjusted by adding sufficient amount of 0.5N NaOH. We added the collagen solution directly on top of the PA-channels and subsequently seal with flat PA gels with the same stiffness as the underlying PA-channels. We incubated the collagen-filled devices at 37℃ in a humidified incubator for 2 hours to allow sufficient gel polymerization and cell attachment. We verified Verify the formation of fibrillar collagen matrix using an optical microscope equipped with 10x objective and phase contrast.

Time-lapse microscopy of live cells.

For time-lapse analysis of cell movement, NIH 3T3 were cultured on the collagen-filled PA-channels which was previously glued to the bottom surface of individual well of 12-multiwell plates. Live cell imaging was conducted using Zeiss microscope equipped with an incubator chamber for controlled temperature, humidity, and CO_2, and a motorized, programmable stage. To obtain time-lapse movies, phase contrast images of NIH 3T3 cells were automatically acquired, at 10X magnification, for 24 hours with 30 mins intervals. For cells migration analysis, individual movies were imported to ImageJ software (National Institutes of Health), and cell migration tracks were extracted using manual tracking plugin. Migratory tracks were subsequently analyzed to obtain migration speed and directionality.

Statistical analysis.

Results are reported as the mean ± Standard Error (SE), unless stated otherwise. A Student's t test was used to identify the significant differences between experimental conditions. A P value of 0.05 or smaller was used to identify the statistical significance difference.

3.4 Part C: Collective migration of co-cultured cell populations in confinement

3.4.1 Introduction

Collective cell migration is a fundamental phenomenon for many normal and pathological processes and is commonly regulated by chemical or physical cues and organization of the the extracellular matrix (ECM) [67–69]. In particular, the regulatory roles of ECM architecture of the tumor microenvironment on cell motility during invasion and metastatic dissemination of cancer cells have already been identified[4, 20, 70]. For instance, during mammary gland development, aligned collagen fibers branches from the terminal end bud concomitant with invasion of epithelial cells into the mammary fat pad. Similarly, during focal and local cancer invasion, ECM orientation plays a critical role in regulating cell migration [71, 72]. Recent studies demonstrate that alignment of the stromal collagen matrix in murine mammary and human breast carcinomas drive invasion and predict poor outcome for human breast cancer patients. In the context of dissemination of cancerous cells from the primary tumor, clusters of cells undergo collective invasion and interact with collagen fibers that provide microscale cues mediating their collective migration phenotype inside these fibers[73]. Thus, in order to understand how such organizational cues direct migration of normal and malignant epithelial cells, we engineered a biomimetic cell migration platform that allows precise control over these architectural parameters. Using photolithography techniques, silicon wafers of defined geometry were fabricated [57] that was subsequently used as a mold to fabricate PDMS microchannels with different geometries to guide and promote cell migration. Using image processing methods, we analyzed overall migration of the monolayer inside the channels and dynamics of individual cells within the monolayer with respect to the channel size. In order

to understand the combined effects of subcellular and extracellular factors on regulation of collective migration, we utilized a mutant cell line of increased contractile forces to emulate the phenotypic heterogeneity present in tumor microenvironment. Specifically, we examined the effect of matrix confinement on the collective migration of MCF10A wild type (WT) cells, MCF10A-CA-RhoA cells with upregulated cell contractility, and mixed population of WT and CA-RhoA cells. Our results reveal that human breast epithelial cells and their genetic derivatives collectively sense and respond to the geometry of the matrix. We find that introducing a small percentage of contractile cells in the culture impacts the migration phenotype of the entire monolayer. Presence of only 5% of the contractile cells in the monolayer leads to formation of large discontinuity inside the monolayer that disturbs the large-range cell-cell communication inside the cells. Further investigations on the role of multiscale cues would stimulate new understanding of the underlying mechanisms of tumor metastasis and assist possible therapeutics development.

3.4.2 Results

Epithelial collective cell migration in confinement.

We used a combination of multiple experimental techniques including photolithography, soft lithography and particle image velocimetry (PIV) to study the migration of an epithelial cell sheet under geometrical confinement. We designed a microchannel matrix platform that includes a large central reservoir connected to channels of different widths ranging from $\sim$20 to 200 μm. A confluent monolayer was grown inside the reservoir and allowed the cell sheet to migrate into the surrounding channels of different sizes. After allowing the cell sheet to migrate for at least 12 hours, we analyzed cell movements within the different channels. We

first studied how this channel-based confinement influences the overall migration velocity of cell sheets by computing the average leading-edge migration of the monolayer as a function of channel width (Fig. 3.13A,E). For WT cells, we observed that the average velocity of the leading front varied with the size of the channel increasing from 20 μm/hr for 200 μm channel width to 35 μm/hr for the 40 μm channel width. However, for CA-RhoA cells, we observed a confinement-independent collective migration, i.e, migration speed did not vary with channel width.(Fig. 3.13E)

Influence of Matrix Confinement on the Velocity Fields of Migrating Epithelial Cell Sheets.

Next, we asked whether the geometric confinement induces a change in local velocity fields within the epithelial cell sheets. Utilizing PIV, we analyzed the migration of individual cells occupying the epithelial monolayer. For WT cells, velocity vectors of smaller magnitude (more blue regions) were observed in 200μm channels. In narrow channels, however, regions of higher velocity magnitude were observed (Fig. 3.13 A). Therefore, confinement mediates both the overall migration of the monolayer and the migration behavior of individual cells inside the monolayer. We then sought to determine whether the confinement would alter the migration of cells with upregulated contractility. For the case of CA-RhoA cells, we did not see notable difference in the velocity magnitude with channel width, i.e., similar velocity distribution was observed for CA-RhoA migrated in wide and narrow channels (Fig. 3.13B). Therefore these results demonstrate that increasing the contractility of the cells make them less sensitive to confinement. Moreover, CA-RhoA cells were found to be faster than the wild type cells in all channel types (Figs.3.13A,B). Further examination of the monolayer dynamics sheds light on the emergence of different modes of collective cell migration. In

wide channels, we observed more of a swirling motion and formation of vortices inside the monolayer. To quantify the swirling in the monolayer, we calculated the vorticity and the heatmap of vorticity demonstrated in Figs.3.13C,D. The strength of the vorticity was higher in wide channels and decreased with the channel size. Consistent with our previous findings in wide channels, cells exhibited more of a swirling motions with stronger vortices [74]. Conversely, in narrow channels, directed cell migration decreased the possibility of vortex formation (Figs.3.13C). Cell with upregulated contractility demonstrated stronger vortices compared to the WT cells and it remained high in all channel widths (Figs.3.13D).

3.4.3 Conclusion

Confining the cells inside the 3D channels of defined geometry is a critical challenge so that fundamental questions about cell-cell and/or cell-ECM interactions in response to the local environment can be investigated. To this end, we have developed an engineered biomimetic cell culture platform that allows for the integrative study of phenotypic heterogeneity and complex stimuli, including matrix confinement and mixed cell populations. This system permits independent control over the roles of critical extracellular and intracellular factors and their interrelationship in the regulation of collective cell migration. Using this platform, we examined the independent and combinatorial effect of subcellular and extracellular cues on collective migration of epithelial cells. We have also show how specific mutations that target cell contractility, which is frequently observed in cancerous cells, influence how cells collectively interact with the mechanical cues present in geometrically complex tumor microenvironments.

3.4.4 Materials and Methods

Fabrication of PDMS mirochannels.

Polydimethylsiloxane (PDMS) microchannels were prepared using soft lithography technique as described before (1). Silcon wafers including the design of the channels were prepared using standard photolitopraphy techiques explained in details in previous chapters. Subsequently, PDMS (Sylgard 184; Dow Corning) was prepared by mixing the base and curing agent in a ratio of 1:20 (wt/wt) and degassed. Then PDMS mixture was poured over the mold, degassed, and cured at 70℃ for 1 h. PDMS channels were seterlized under UV for 1 hours and plasma cleaned for 3 mins to make their surface hydrophilic. A solution of 0.1mg/ml of collagen was added to channels to cover the whole surface. The mixture was allowed to be adsorbed for overnight at 4℃ after which the collagen solution was removed and PDMS devices were washed with PBS.

Cell culture.

MCF-10A mammary epithelial cells were grown, as previously described [38], in DMEM/F12 (Invitrogen), with 5% (v/v) horse serum (Invitrogen), 20 ng/mL epidermal growth factor (EGF, Miltenyi Biotec Inc), 0.5 mg/mL hydrocortisone (Sigma-Aldrich), 100 ng/mL cholera toxin (Sigma-Aldrich), 10 ug/mL insulin (Sigma-Aldrich), and 1% (v/v) penicillin-streptomycin (Sigma-Aldrich). CA-RhoA cells maintained in culture media supplemented with puromycin. To culture mixed populations of the MCF10A and CA-RhoA cells, two different percentage of CA-RhoA cells (50% and 5%) were mixed with MCF-10A cells. Cell suspension containing 15,000 cells , of the mixed cells suspension, were seeded in the central

chamber of the PA devices. After attachment of the cells to the substrate, growth media was added, and these cell-laden devices were incubated at 37℃ and 5% CO2 3days before starting the time-lapse imaging.

Time lapse imaging and migration analysis

Time-lapse microscopy was initiated 3 days after cells seeding and when the monolayer start to enter into the mirochannels. Time-lapse imaging was carried out in the phase contrast on an inverted microscope (Zeiss Cell Observer) equipped with an incubator capable of maintaining an environment with 37℃ temperature and 5% CO_2 level. Images were acquired with a 10× objective. Two successive images of the same field were taken at 30 minutes time interval. To obtain the average leading edge migration speed of the epithelial sheet, the Motion of the leading edge of the cell monolayer was manually tracked by recording the position of cell border using a homemade macro in ImageJ. Subsequently, coordinates of the leading edge were imported into a custom-made program in MATLAB and its advancement was calculated. Leading edge speed was defined as the ratio of the leading edge advanced distance and the time course of migration. To analyze the dynamic of cells inside the monolayer, we performed PIV as described in detail in chapter 4.

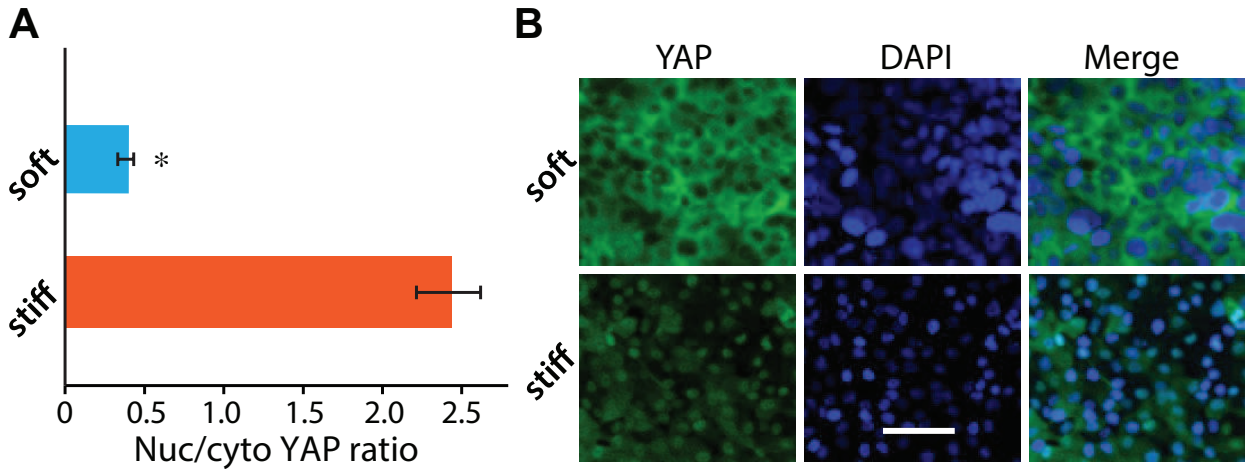

Figure 3.1: **YAP activity in clustered cells on flat gels of varying stiffness.** (A) Quantification of nuclear YAP localization in terms of nuclear/cytoplasmic ratio of YAP expression on soft and stiff flat PA gels. $^{*}p<0.05$ with respect to stiff ECM. N>30 cells per condition, from at least three separate experiments. (B) Representative immunofluorescence images of YAP (green) and DAPI (blue) in MCF-10A epithelial sheet cultured on soft (top) and stiff (bottom) ECMs. Scale bar = 50 μm.

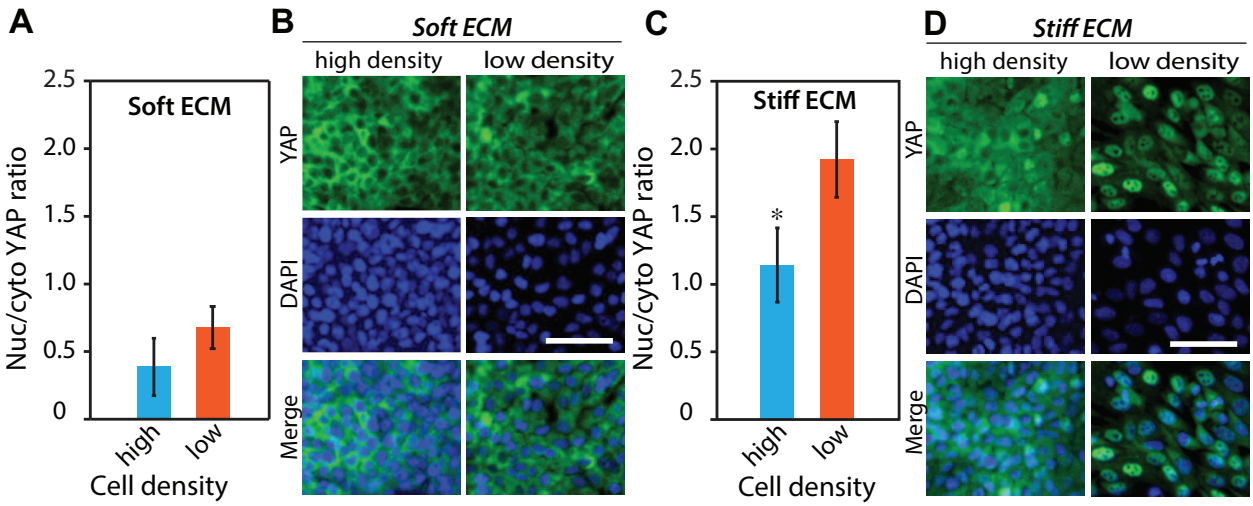

Figure 3.2: **Regulation of YAP activity by cell density.** (A) On soft ECM, nuclear/-cytoplasmic ratio of YAP expression in cells within the low-density ($cells/cm^2$) or high-density ($cells/cm^2$) epithelial clusters. (C) On stiff ECM, nuclear/cytoplasmic ratio of YAP expression in cells within the low-density ($cells/cm^2$) or high-density ($cells/cm^2$) epithelial clusters. $^*p<0.05$ with respect to the low cell density case. N>30 cells per condition, from at least three separate experiments. Confocal immunofluorescence images of YAP expression (green) and nuclei (blue) for MCF-10A cell clusters of varying cell densities, cultured on (B) soft and (D) stiff substrates. Scale bar = 50 μm.

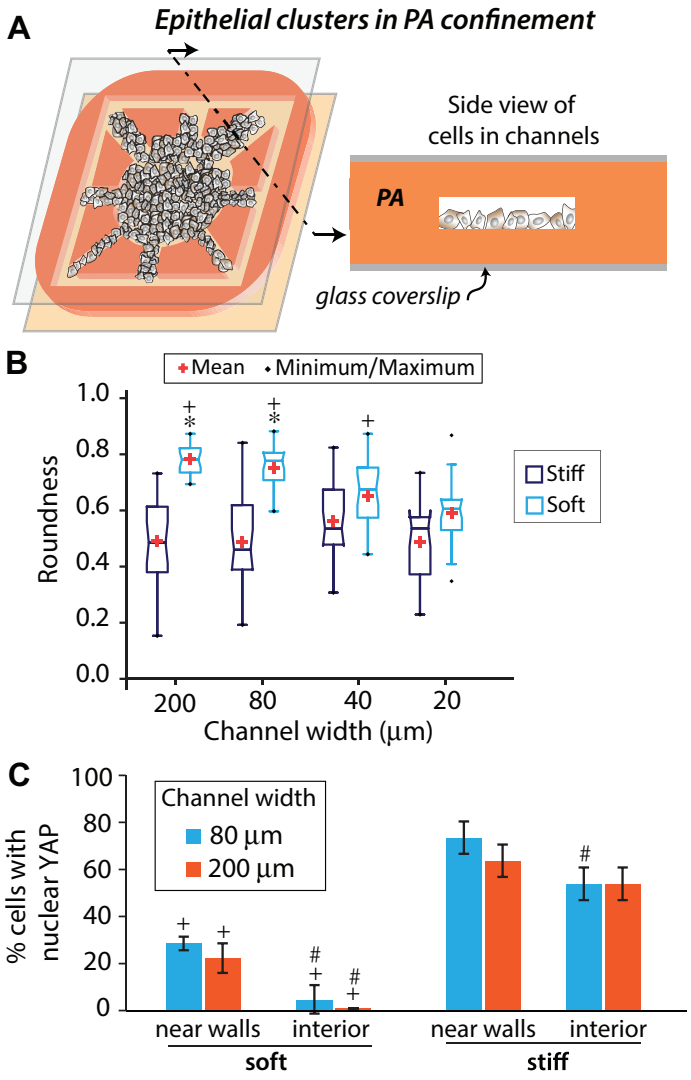

Figure 3.3: **Cell morphology and YAP activity in microchannels.** (A) Schematic describing epithelial cell clusters grown inside the polyacrylamide (PA)-microchannels based platform. (B) Cell roundness for single cells in epithelial clusters inside channels of varying widths made of soft and stiff substrates. $^{*}p<0.05$ with respect to stiff ECM. $^{+}p<0.05$ with respect to narrow (20μm) channels. N>20 cells per condition, from at least three separate experiments. (C) Percentage of cells with nuclear YAP localization in wide channels (80 or 200μm channel width), in regions close or away from the channel walls. $^{+}p<0.05$ with respect to stiff ECM. $^{\#}p<0.05$ with respect to 'near walls' condition. N>20 cells per condition, from at least three separate experiments.

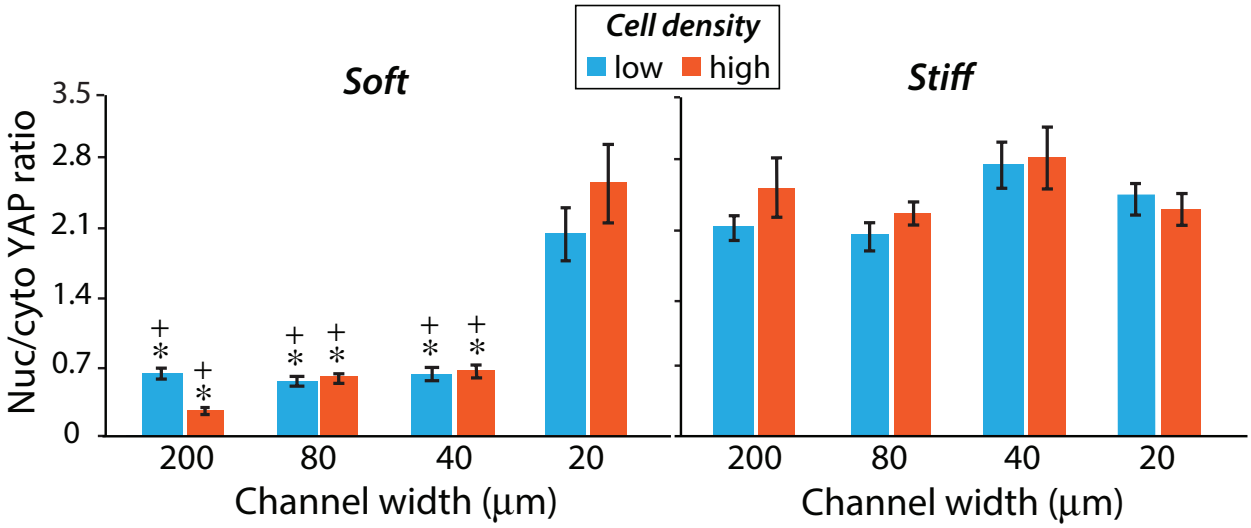

Figure 3.4: **YAP activity in cell clusters cultured in channels of varying width and stiffness.** Nuclear/cytoplasmic ratio of YAP expression in cells within the low- or high-density epithelial clusters cultured in channels of varying width made of soft (left) or stiff (right) PA gels. In soft channels, the average low and high cell densities are and $cells/cm^2$, respectively. In stiff channels, the average low and high cell densities are and $cells/cm^2$, respectively. $^{+}p<0.05$ with respect to stiff ECM. $^{*}p<0.05$ with respect to narrow (20 μm) channels. N>30 cells per condition, from at least three separate experiments.

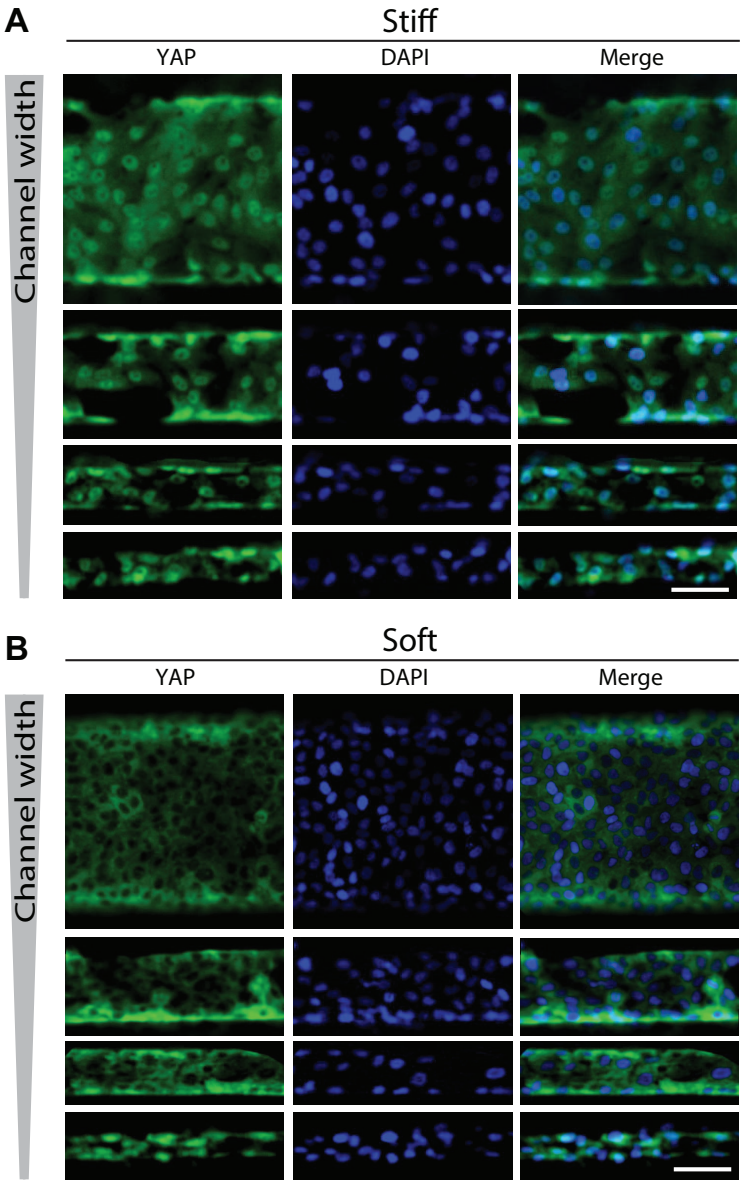

Figure 3.5: **Enhanced YAP nuclear localization in stiffer and narrower channels.** Representative immunofluorescence images of YAP (green), nuclei stained with DAPI (blue), and merged for epithelial cells embedded inside (A) stiff and (B) soft channels of varying width. Scale bar = 50 μm.

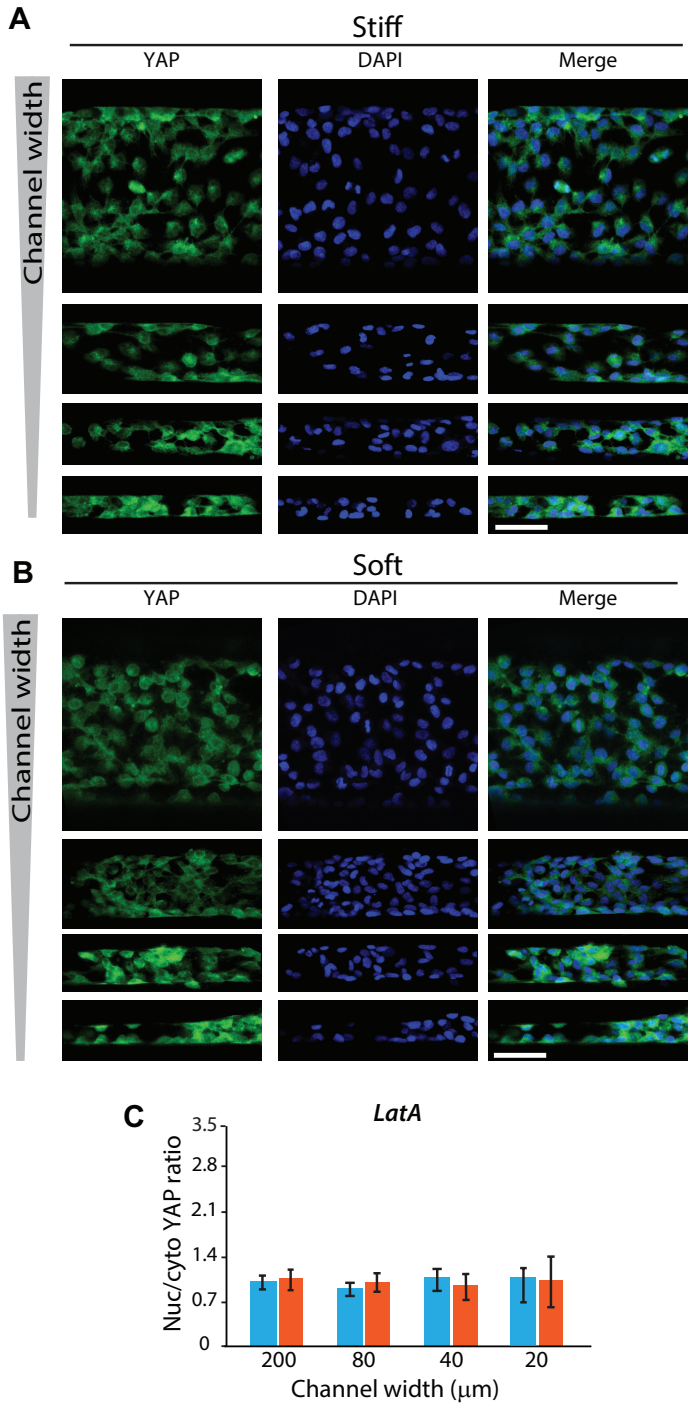

Figure 3.6: **Reduced YAP nuclear localization in stiffer and narrower channels after disrupting F-actin polymerization.** Representative immunofluorescence images of YAP (green), nuclei stained with DAPI (blue), and merged for LatA-treated epithelial cells embedded inside (A) stiff and (B) soft channels of varying width. Scale bar = 50 μm.

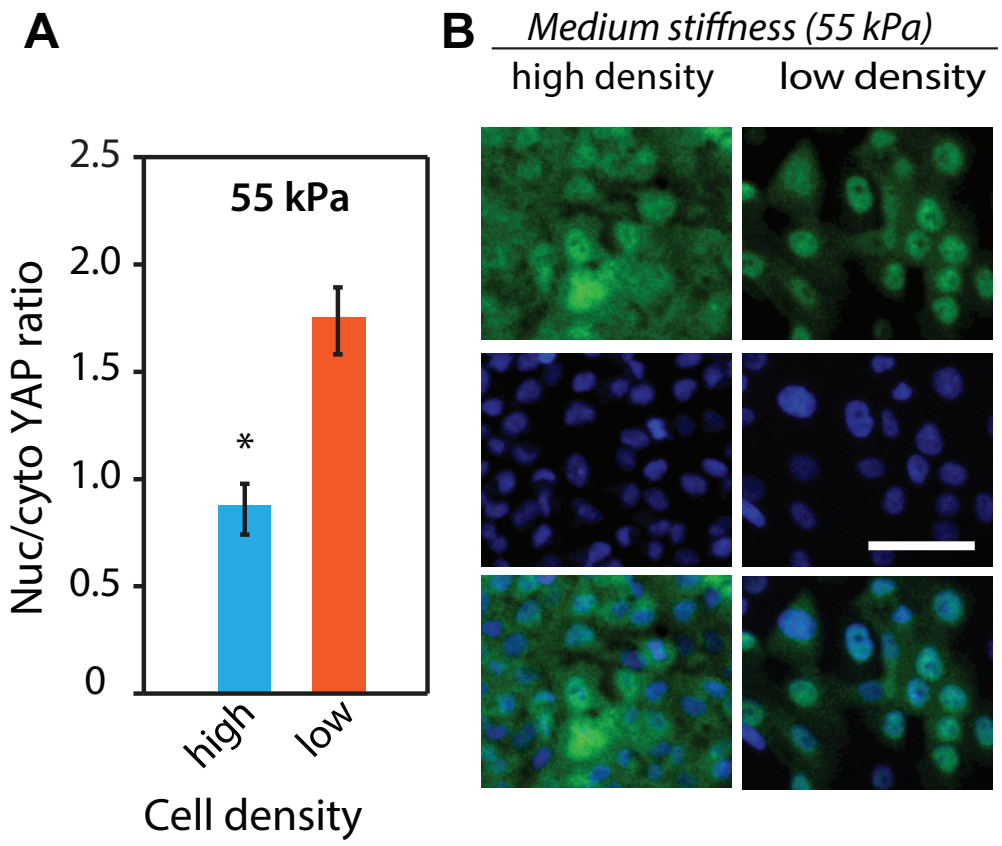

Figure 3.7: **Intermediate ECM stiffness preserves nuclear YAP.** (A) On intermediate ECM stiffness of 55kPa hydrogels, nuclear/cytoplasmic ratio of YAP expression in cells within the low or high density epithelial clusters. *$p<0.05$ with respect to the low cell density case. N>30 cells per condition, from at least three separate experiments. (B) Confocal immunofluorescence images of YAP expression (green) and nuclei (blue) for MCF-10A cell clusters cultured on medium stiffness (55kPa) substrates. Scale bar = 50 μm.

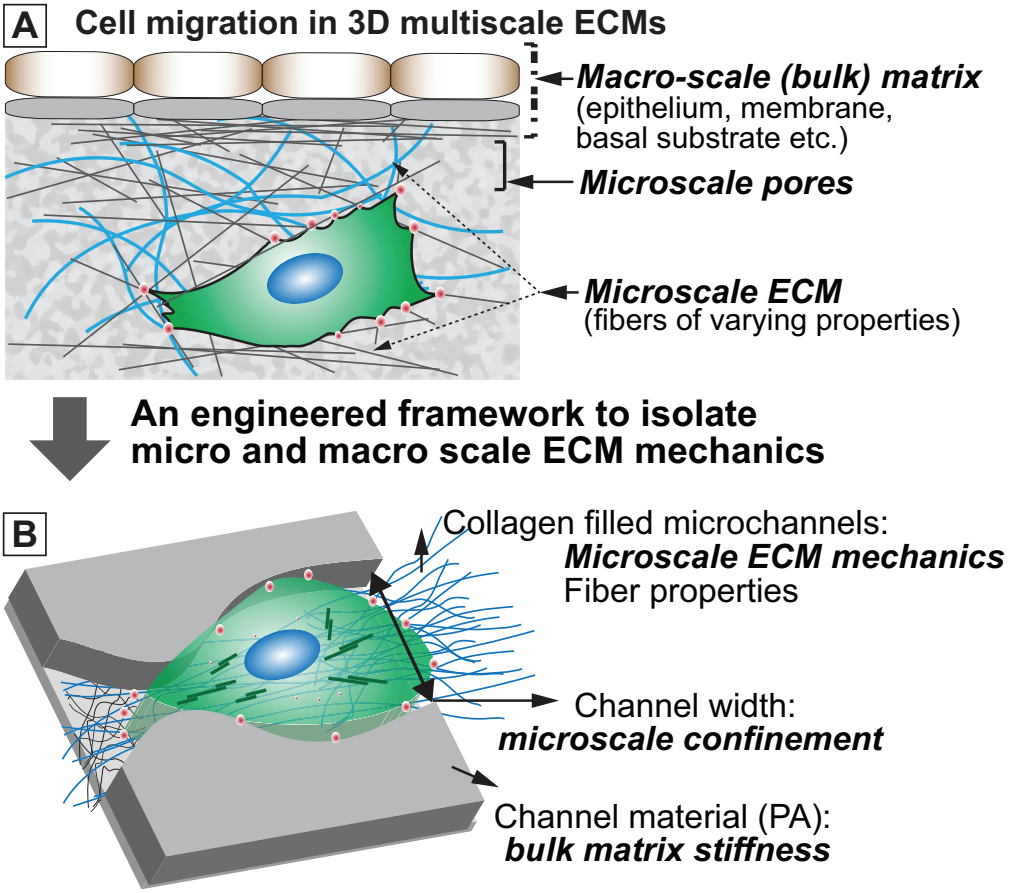

Figure 3.8: **Fabrication of collagen-filled PA-channels for analysis of single cell motility in confinement.** (A) Schematic of a cell surrounded by layered matrix comprising ECM fibers of varying architecture and density, and bulk matrix that constitutes epithelium and other stiffer layers of ECM. (B) A microchannels-based approach to systematically isolate various ECM parameters at both macro and micro scales.

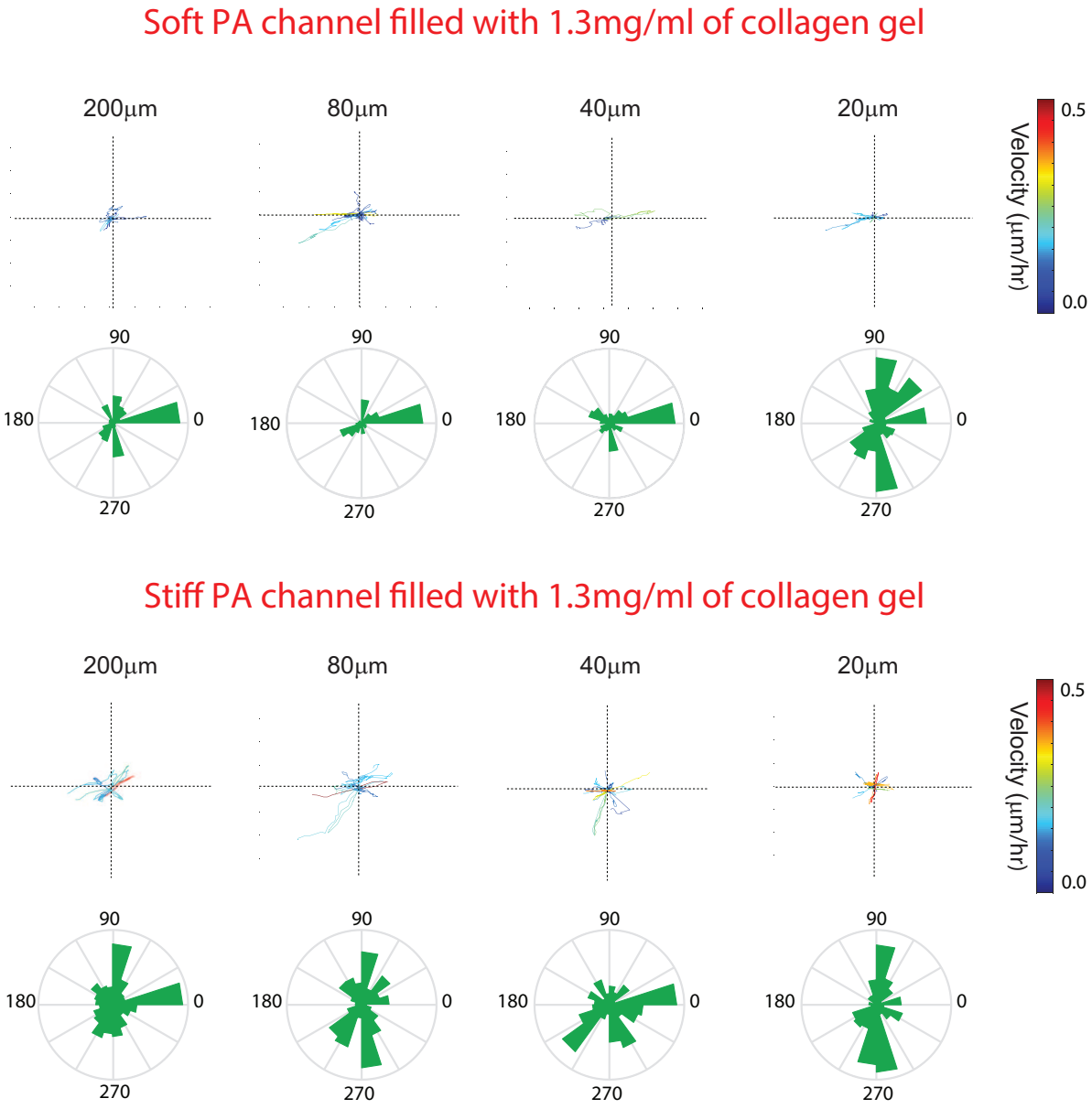

Figure 3.9: **Reduced sensitivity of NIH3T3 cells to bulk channel stiffness and confinement inside the dense collagen network.** Plots indicate single cell trajectories that is color coded according to migration speed, color scale bar represent the color coding scheme , for cells embedded in dense (1.3mg/ml) collagen network filled inside the soft PA channels with varying geometries (A) , and inside the dense collagen network layered on stiff PA-channels (C). Rose plots demonstrate the distribution of velocity angles for cells on soft PA-channels (B) and stiff PA-channels (D) filled with dense collagen solution.

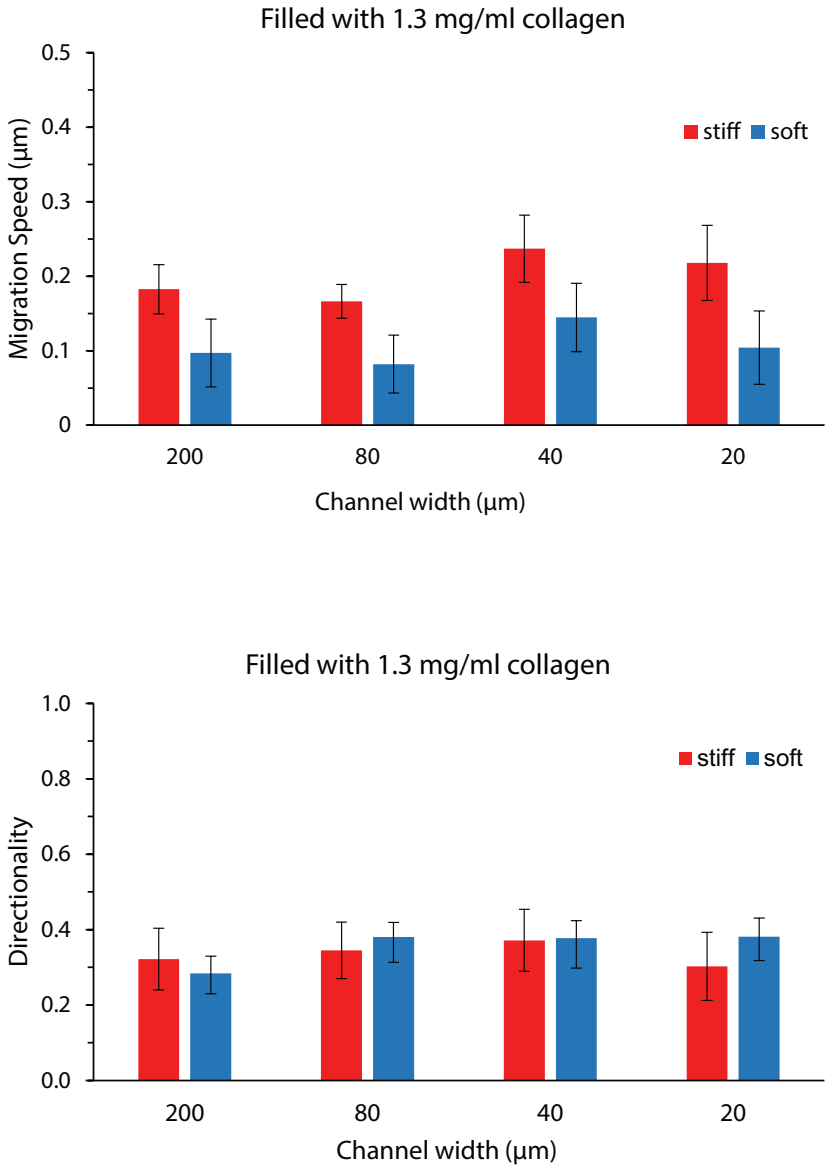

Figure 3.10: **Effect of macroscale ECM properties on migration for cells embedded inside dense collagen network.** Plots indicate average directionality (A) and migration speed (B) for NIH3T3 cells embedded in dense collagen gels filled either inside soft and stiff PA-channels. Average quantities obtained from analysis of at least 30 single cells. Error bar denotes standard deviation of mean.

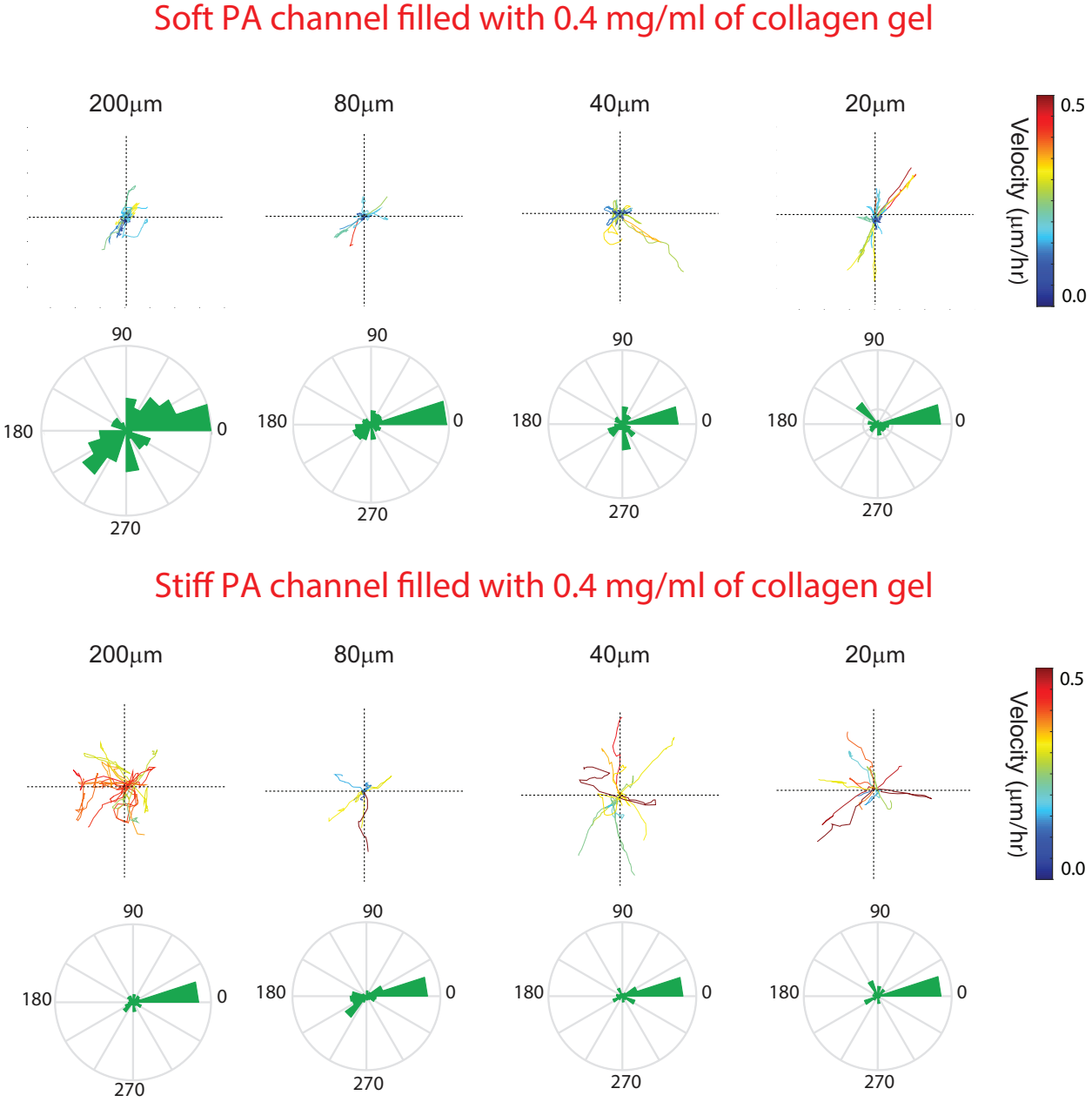

Figure 3.11: **Greater influence of channel stiffness and confinement on cell motility in low-density collagen.** Plots indicate single cell trajectories that is color coded according to migration speed, for cells embedded in low-density (0.4mg/ml) collagen injected inside the (A) soft PA channels, and (C) stiff PA -channels. Rose plot demonstrates the distribution of velocity angles for cells in (B) soft PA-channels and (D) stiff PA-channels filled with sparse collagen solution.

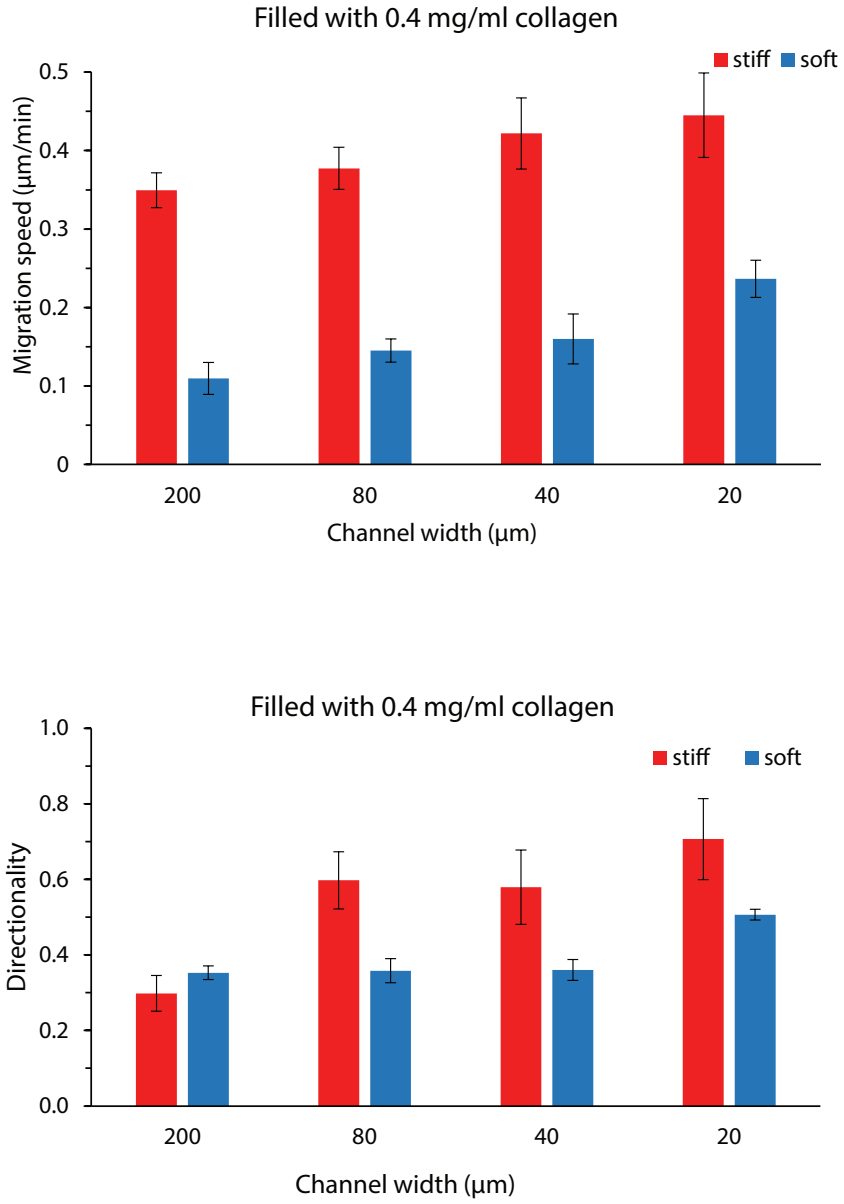

Figure 3.12: **Effect of channel stiffness and confinement on migration of cells embedded within low-density collagen.** Plots indicate average directionality and (A) and migration speed (B) for NIH3T3 cells embedded in low-density (0.4mg/ml) collagen-filled soft and stiff PA-channels. N>30. Error bar denotes standard deviation of mean.

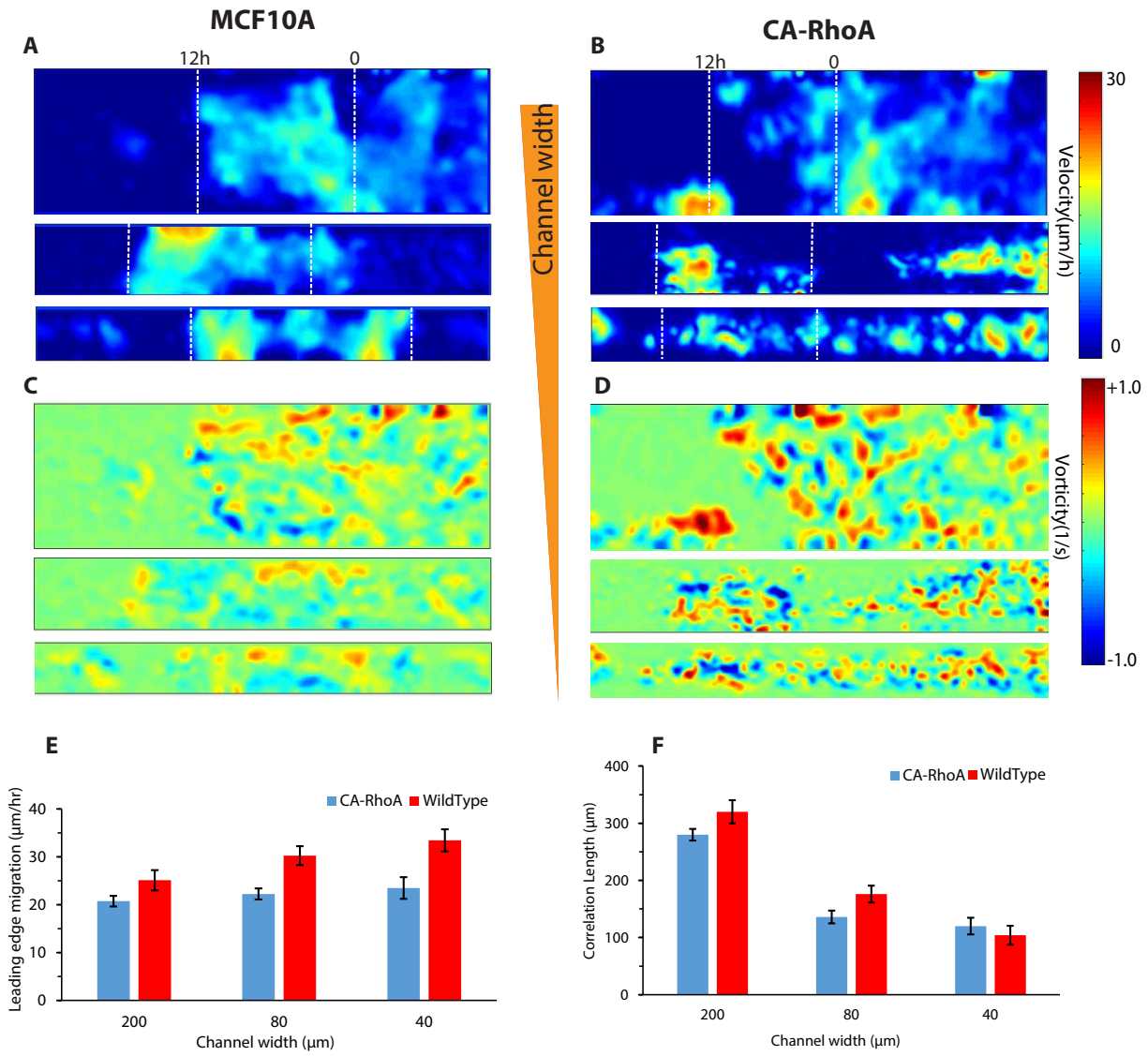

Figure 3.13: **Migration of epithelial sheet inside the micro-channels of varying width.** Heat map showing spatial distribution of velocity fields at a given time instant in 200 μm (Top), 80 μm (Middle), and 40 μm channels (Bottom) for MCF-10A cells (A) and CA-RhoA cells (B). Plots indicate heatmaps of vorticity magnitude for MCF10A (C) and CA-RhoA (D) cells migrating inside the 200 μm (top), 80 μm (middle), and 40 μm (bottom) microchannels. (E) Average velocity of monolayer leading front in microchannels of varying width for MCF10A and CA-RhoA cell sheet. (F) Average spatial correlation of velocity vectors inside channels of varying width for both of MCF10A and CA-RhoA cells.

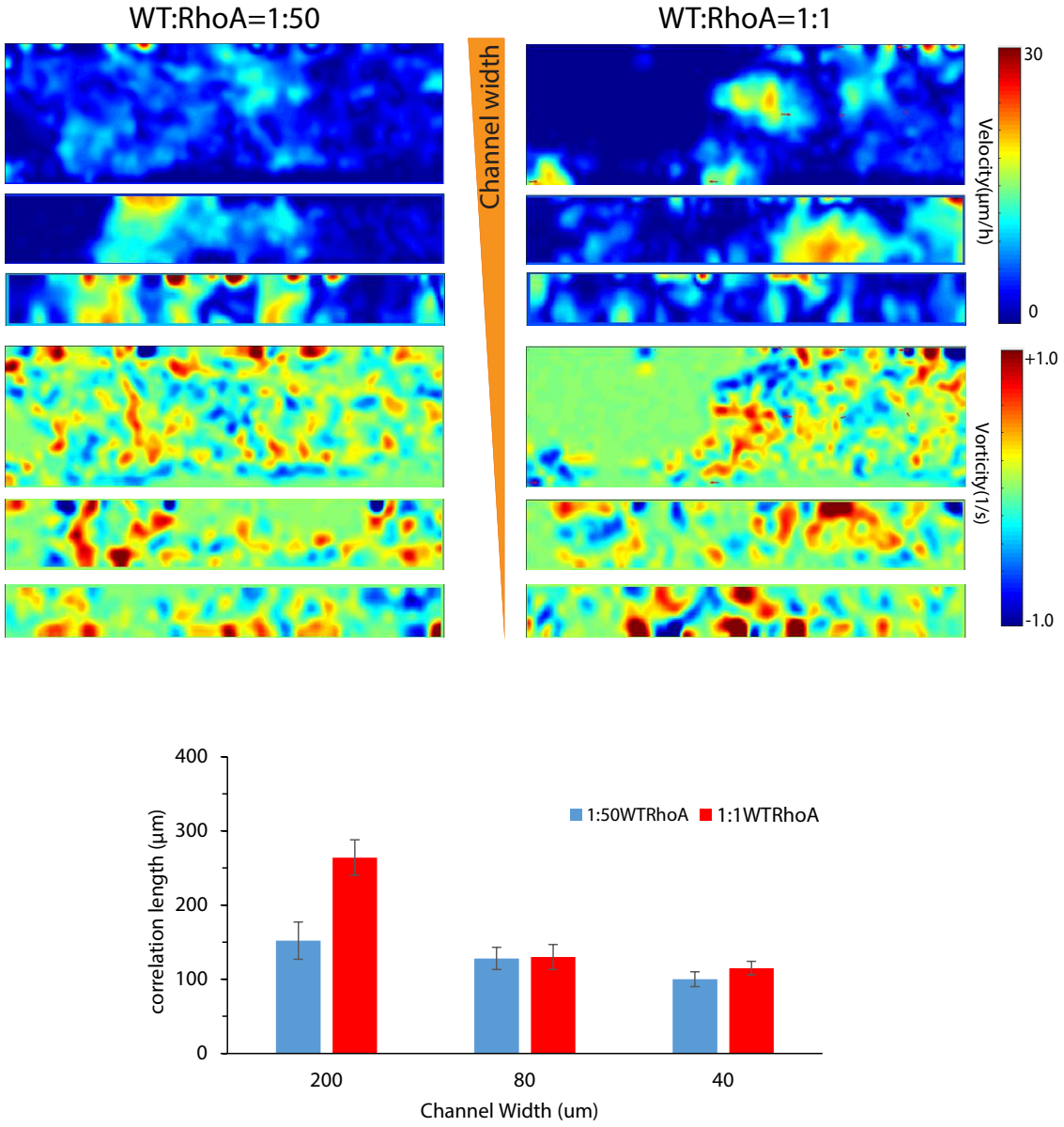

Figure 3.14: **Migration of mixed population of epithelial sheet inside the microchannels of varying width.** Heat map showing spatial distribution of velocity fields at a given time instant in 200 μm (Top), 80 μm (Middle), and 40 μm channels (Bottom) when MCF10A cells mixed with 50% (A) and 5% (B) of CA-RhoA. Plots indicate heatmaps of vorticity magnitude for MCF10A mixed with 50% (C)and 5% (D) of CA-RhoA cells when cell sheet is migrating inside the 200 μm (top), 80 μm (middle), and 40 μm (bottom) microchannels. (E) Average spatial correlation of velocity vectors inside channels of varying width for both types of mixed populations.

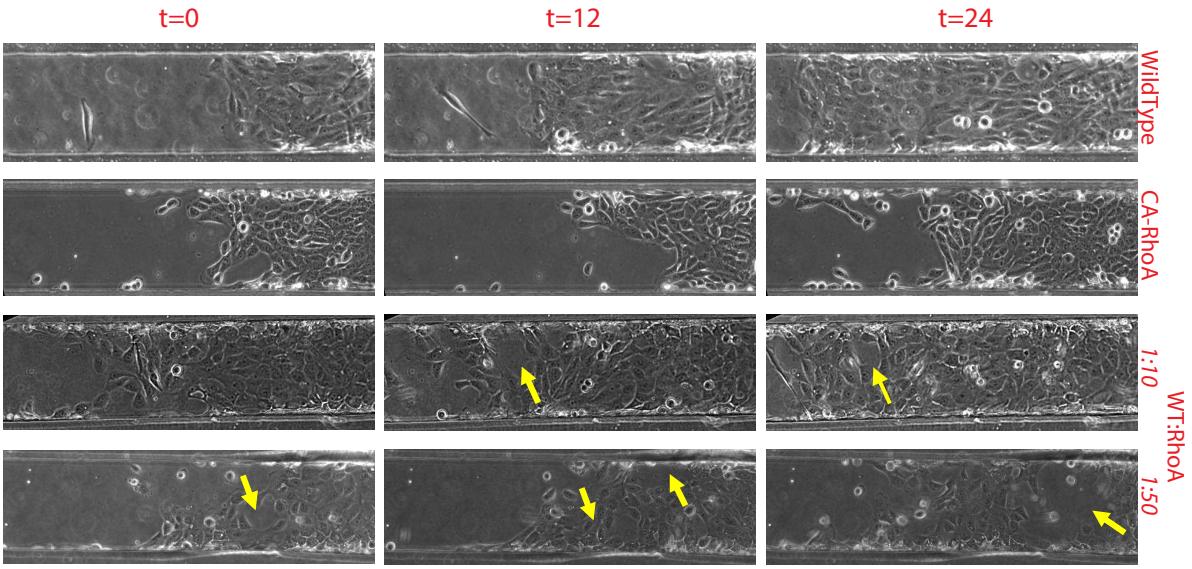

Figure 3.15: **Presence of low concentration of contractile cells leads to formation of discontinuity in the monolayer.** Phase contrast images of epithelial sheet at three different time instants (t=0; start of the migration, t=12hrs, and t=24hrs) for MCF10A cells, CA-RhoA cells, and for the mixed populations.

Chapter 4

Collectively migrating cells store mechanical memory of past matrix stiffness

4.1 Summary

During morphogenesis and cancer metastasis, grouped cells migrate through tissues of dissimilar stiffness. Although the influence of matrix stiffness on cellular mechanosensitivity and motility are well-recognized, it remains unknown whether these matrix-dependent cellular features persist after cells move to a new microenvironment. Here, we interrogate whether priming of epithelial cells by a given matrix stiffness influences their future collective migration on a different matrix – a property we refer to as the 'mechanical memory' of migratory cells. To prime cells on a defined matrix and track their collective migration onto

an adjoining secondary matrix of dissimilar stiffness, we develop a modular polyacrylamide substrate through step-by-step polymerization of different PA compositions. We report that epithelial cells primed on a stiff matrix migrate faster, display higher actomyosin expression, form larger focal adhesions, and retain nuclear YAP even after arriving onto a soft secondary matrix, as compared to their control behavior on a homogeneously soft matrix. Priming on a soft ECM causes a reverse effect. The depletion of YAP dramatically reduces this memory-dependent migration. Our results present a previously unidentified regulation of mechanosensitive collective cell migration by past matrix stiffness, in which mechanical memory depends on YAP activity.

4.2 Introduction

Mechanical properties of the extracellular matrix (ECM) influence phenotypic and genotypic cellular responses, which can impact cell differentiation, migration, and proliferation [4, 12, 37, 54]. In particular, matrix stiffness regulates cellular forces, adhesions, protrusions, and polarization through mechanotransductive signaling, all of which lead to mechanosensitive variations in migration phenotypes of both single and grouped cells [4, 20, 75, 76]. Physiologically, migratory cells do not continually interact with just one type of matrix. Instead, grouped cells migrate through mechanically heterogeneous matrices, forming the basis of fundamental biological processes including embryonic development, wound healing, regeneration, and cancer metastasis [77]. During embryonic development, a coordinated collective movement of epithelial cells across diverse microenvironments enables branching morphogenesis, a process necessary for organ formation [78, 79]. In cancer metastasis, the

mechanical properties of the primary tumor microenvironment are known to induce declustering [12, 57, 80] and outward migration [20, 81] of cancer cells into the mechanically dissimilar surrounding tissue, which represent the first steps of tumor invasion.

As cells pass through a tissue microenvironment, a distinct set of mechanosensitive signaling events occur [37], such as clustering of integrin-based adhesion proteins into focal adhesions [82], Rho-ROCK activation [83, 84], and nuclear localization of transcriptional regulators YAP and SNAIL1 [36, 85]. Recently, mechanical dosing of human mesenchymal stem cells on matrices of tunable stiffness has been found to regulate mechanical memory-dependent lineage commitment decisions, and this process is shown to depend on YAP activity [53]. To study cell migration on heterogeneous matrices, gel systems with gradient stiffness have be used to show durotaxis for single [86] and collective cells [76], and define specific roles of nonmuscle myosin-IIB [87] and microtubule organization [88] in cell polarization during spontaneous migration. However, it remains unknown whether the cells first primed on a given ECM for a defined duration retain their mechanosensitive signatures even after moving to a new microenvironment. We refer to this persistent influence of cellular mechanosensitivity on cell migration as the 'mechanical memory of migratory cells'. In this study, we asked – do collectively migrating cells remember their past matrix stiffness as they move across dissimilar microenvironments?

To test this question, we developed a modular polyacrylamide (mPA) substrate comprising contiguous primary and secondary ECM regions of independently defined stiffness. We find that a monolayer of cells primed on a stiff ECM migrated faster and in a more coordinated manner after arriving on a soft secondary ECM, as compared to those cultured on a homogeneously soft ECM. Nuclear translocation of YAP persisted even after cells arrived onto a softer secondary ECM and shRNA-mediated depletion of YAP dramatically blunted

this mechanical memory-dependent cell migration. Taken together, our results bring an additional dimension to the mechanosensitive migration of epithelial cells in response to only their immediate microenvironment. Mechanical memory in migratory cells may have a particular significance to cancer metastasis, where future invasion potential of escaped cancer cells may be predicted by exploiting their persistent dependency on the primary tumor microenvironment stiffness.

4.3 Results

4.3.1 Fabrication of dual-stiffness contiguous substrates.

To prime epithelial cells on a given ECM and track their subsequent collective migration onto an adjoining ECM of dissimilar stiffness, we fabricated a modular-PA (mPA) hydrogel substrate through step-by-step polymerization of two different PA compositions [89] (Fig. 4.1a). Through AFM-based mechanical characterization of these gels, as done previously [4, 90], we found that the soft and stiff regions have corresponding Young's moduli of approximately 0.5 and 50 kPa, respectively (Fig. 4.1b). These measurements also verified that the ECM stiffness in the primary and secondary ECM regions varied in a step manner, as intended. These stiffness values are not chosen to match any specific tissue context; rather, this range is designed to explore the biophysical effects of cellular priming across a steep change in matrix stiffness. Next, we designed a PDMS stencil for culturing an epithelial monolayer restricted within the central section of the mPA gel, which we will refer to as the 'primary' ECM. After priming the cell colony on the primary ECM for a prescribed duration,

the PDMS stencil was removed to enable collective migration of the cell sheet into the surrounding 'secondary' ECM of independently defined stiffness. We verified that the coating of collagen I on the PA gel did not vary with stiffness or the removal or PDMS stencil (Fig. 4.9). In this system, epithelial cells seamlessly move across a contiguous substrate composed of mechanically distinct regions, whose stiffness can be tuned over two orders of magnitude. Thus, we are able to study the effect of past ECM stiffness on future cell behavior without having to detach and re-culture cells on a new substrate. Comparison of cell behavior on a given secondary ECM with respect to varying priming ECM stiffness would reveal whether migratory epithelial cells store mechanical memory of their past mechano-regulated state.

4.3.2 Leading edge migration depends on the past ECM stiffness.

To assess the effect of past ECM stiffness on collective cell migration, we cultured MCF10A human mammary epithelial cells on primary ECM stiffness (P) for 3 days and then allowed the cells to migrate onto a secondary ECM (stiffness 'S'). We performed time-lapse microscopy for an additional 2 days, i.e., between days 4-5 from the time of initial culture, and manually traced the leading edge over time, as illustrated in Fig. 4.2a. On substrates with homogeneous stiffness (P=S), the average leading edge migration on stiff ECM (50 kPa) was 30µm/h, which was three times higher than its value on the soft ECM (0.5 kPa) (Fig. 4.2b). This stiffness-dependent collective cell migration speed is consistent with previous studies [75, 76]. When the cell monolayer was first primed on a stiff primary ECM (P=50 kPa), the leading edge migration speed measured on the adjacent soft secondary ECM was ~ 2.5 times higher than the control case of homogeneously soft ECM (Fig. 4.2b). This enhanced leading edge migration could be attributed to the stiffness-dependent mechano-activated state of cells attained due to stiff priming, which we define as the mechanical memory of collectively

migrating cells. We also found that the soft-primed cells migrated $\sim 40\%$ slower than those primed on a stiff ECM (Fig. 4.2b).

To test whether the duration of priming on the primary ECM influenced the memory-dependent migration, we measured migration speed after priming for 1 or 2 days. We found that the influence of the primary ECM stiffness reduced with shorter priming duration (Fig. 4.2c). Given that longer priming led to more pronounced mechanical memory-dependent collective migration, all results presented in this manuscript will correspond to a 3-day priming regimen, followed by 2 days of migration on the secondary ECM. All measurements are conducted on the secondary ECM, unless specified otherwise.

We also measured leading-edge migration speed for MCF7 breast cancer cells and A431 human epidermoid carcinoma cells. While MCF7s were slower and A431s were faster compared to MCF10As, both of them exhibited robust mechanical memory-dependent migration (Figs. 4.2b, 4.10).

4.3.3 Stiffer primary ECM predicts more correlated cell migration.

Using particle image velocimetry (PIV) analysis of phase contrast images of the migrating cell sheet over time [91], we examined cellular motions within the epithelial monolayer (Fig. 4.3a). After arriving on a soft secondary ECM, stiff-priming led to high velocity magnitudes of the leading-edge cells, as compared to the soft primary ECM. Conversely, soft-priming significantly reduced the cell velocities. We noted that cells behind the leading edge had lower velocity magnitudes in all cases. By plotting single cell trajectories over a 12 hour period,

we confirmed faster velocities of cells at the leading edge compared to the ones within the monolayer (Fig. 4.11).

We found that the correlation length, defined as the distance of correlation among velocity vectors of neighboring cells [92], for cells migrating on a homogeneously stiff ECM was ∼0.25 mm, which is ∼25% higher than its value measured on a purely soft ECM (Fig. 4.3c). Thus, higher ECM stiffness enables larger portions of the cell sheet to migrate in a coordinated fashion, which is consistent with previous findings [75]. The stiff-primed cells migrated on a soft secondary ECM with 0.25mm correlation length, the same as the value measured on a homogeneously stiff ECM. In comparison, soft-primed cells migrated with a lower correlation length of 0.2mm on a stiff secondary ECM. The order parameter of the collective migration, defined as the angle between the velocity vectors and the direction of leading edge migration, on a homogeneously stiff ECM was more than twice its value on a soft ECM (Figs. 4.3d, 4.12), indicating a more ordered collective migration on stiffer ECM [75]. The order parameter of stiff-primed cells remained high (0.6) on the soft secondary ECM. To assess the temporal progression of collective cell motility onto the secondary ECM, we selected four representative videos of collective cell migration for each condition and plotted how a column of cells traversed over a 12 h period (Fig. 4.3b). Cells maintained their velocity magnitudes and order parameter over time, i.e., pixel intensities rarely varied over this 12 h period and distance (Fig. 4.3b).

To further expand the temporal variation of migration speed across numerous samples, we averaged leading-edge migration speed at given time points and plotted these values over 4 days of migration after the 3-day priming (Fig. 4.3e). We found that the stiff-primed monolayers maintained at least 2 times higher speed on a soft secondary ECM (compared to purely soft ECM) for at least 3 days. This memory-based advantage in the migration

speed of stiff-primed cells started to subside afterwards (Fig. 4.3e). Thus, the presented effects of mechanical memory correspond to a phenotype maintenance within a temporal boundary, which is measured here as 3 days of collective migration in the secondary ECM.

4.3.4 Higher actin/pMLC expression and adhesions due to stiffer priming.

Since cell-ECM adhesions and actomyosin machinery are crucial for generating forces and driving cell motility [4, 75, 93], we examined whether their subcellular expressions within individual cells near the leading-edge of the monolayer depend on the priming stiffness. To this end, we stained and imaged for F-actin and phosphorylated myosin light chain (pMLC) in cells after their migration across the secondary ECM. We found that actin fiber alignment (from phalloidin images), pMLC expression, and number of focal adhesion (FAs) (paxillin images) in cells on homogeneously stiff ECM were significantly higher than their average values measured on a soft ECM (Fig. 4.4, 4.13). After stiff-priming, cells on a soft ECM exhibited larger FAs ($\sim$4 times), pMLC expression ($\sim$2.5 times) and actin alignment ($\sim$1.6 times) compared to the control case of homogeneously soft ECM (Fig. 4.4b-d). These results indicated that stiff-priming allowed the cells to maintain enhanced actomyosin machinery even after their traversal onto a soft secondary ECM. Conversely, the actin alignment and pMLC expression were reduced significantly after soft-priming.

To examine whether stiffness-sensitive cell spreading in the primary ECM could influence the leading-edge migration, we calculated cell areas across the monolayer. Notably, in all four matrix conditions, cell spreading reduced with distance from the leading edge, which led to a stiffness-insensitive spreading in the rear part of the monolayer (Fig. 4.4e) and

priming-dependent spreading near the leading-edge. Thus, cell spreading in the primary region cannot influence the leading-edge migration computed in the secondary region.

4.3.5 Alternate hypotheses for memory-dependent migration due to cell proliferation and signal transmission.

Although the results in Figs. 1-4 clearly show the influence of past ECM stiffness on cellular features in the secondary ECM, we examined several alternative hypotheses other than the proposed 'memory-storing' abilities of migratory epithelial cells can explain the observed behavior. First, we asked whether mechano-sensitive cell proliferation due to the stiffer primary ECM in the rear of the monolayer could influence leading edge migration. After inhibiting cell proliferation (thymidine treatment; see Methods and Fig. 4.14), cell migration speeds increased due to increased spreading, yet the trend of mechanical memory-dependent migration held true (Fig. 4.5a-b). In some conditions, we observed higher migration speed after proliferation inhibition, which may be attributed to increased cell spreading (Fig. 4.5c).

Second, to attenuate inter-cellular force transmission, we repeated migration measurements in the presence of a calcium chelator (4mM EGTA), as used previously for this purpose [94,95], which disrupts cell-cell communication (as shown through E-cadherin images in Fig. 4.5f). As a result, some cells break away from the monolayer. Overall, we found that the memory-dependent migration of the leading edge was preserved despite the loss of cell-cell communication (Fig. 4.5d-e).

Finally, to eliminate any possible communication between the primary and secondary regions, we physically removed the entire primary region along with the attached cells before measuring migration in the secondary ECM (1 day after complete priming). We found that

the memory-dependent migration persisted in this system (Fig. 4.5g-h). These results, along with the ones presented above, confirm that the memory-dependent migration observed in the secondary ECM is independent of a direct communication with the primary ECM. Instead, the priming-dependent signals are likely stored within the cells and continue to dictate collective migration in the future.

4.3.6 Migratory cells store mechanical memory of past ECM stiffness through YAP activity.

The observed memory-dependent collective cell migration indicates that the priming-dependent mechano-regulated state of cells may persist onto the new ECM. Given that nuclear translocation of YAP has been identified as a sensor of ECM stiffness [36, 49, 96] , we determined YAP subcellular localization within MCF10A cells as they migrated across ECMs of dissimilar stiffness. We quantified nuclear-to-cytoplasmic ratio of YAP fluorescent intensity in at least 40 cells from multiple fields. Consistent with previous findings [53], YAP expression was predominantly nuclear on homogeneously stiff ECM and cytoplasmic on homogeneously soft ECM (Fig. 4.6). However, nuclear YAP localization of stiff-primed cells when measured in soft secondary ECM was more than four times its value on homogeneously soft ECM (Fig. 4.6b). Thus, nuclear accumulation of YAP due to the stiffer past ECM persisted even after the cells migrated onto the adjoining softer region. Conversely, soft-primed cells on stiff secondary ECM showed less than 1/3rd nuclear YAP, compared to the homogeneously stiff ECM (Fig. 4.6c). We repeated these measurements in MCF7 and A431 cells (Figs. 4.6b-c, 4.15) and found that both these cancer cell lines followed a similar dependence of subcellular YAP localization on the past matrix stiffness. Thus, cellular mechano-sensation

of ECM stiffness through subcellular YAP localization could be a key mechanism for storing mechanical memory in migratory cells.

4.3.7 Inhibition of mechanical memory-based cell migration through YAP depletion.

To further examine whether YAP activity is a requirement for memory-dependent migration, we performed shRNA-mediated depletion of YAP in MCF10A cells (YAP-KD) (Fig. 4.7b), as described previously [85, 97]. We found that the leading-edge migration speed of stiff-primed YAP-KD cells was ∼15 μm/h on a soft secondary ECM, which was similar to the control case of a homogeneously soft ECMs (Fig. 4.7a,c). Even after priming on a soft ECM, YAP-KD cells migrated fast (∼30 μm/h) on a stiff secondary ECM, matching with the control case of a homogeneously stiff ECM. Thus, after YAP depletion, cells were unable to exploit prior priming. Surprisingly, the YAP-depleted cells on homogeneously stiff ECM were almost twice as fast compared to those on homogeneously soft ECM (Fig. 4.7a,c). Through PIV analysis of cellular motions within the monolayer, we also found that the cells within the monolayer migrated in a memory-independent manner, with greater correlation and in a more ordered fashion on a stiffer ECM regardless of the primary ECM stiffness (Figs. 4.7d-e and Fig. 4.16).

Given that YAP is a classic mechano-sensor [36], the observed ECM stiffness-dependent migration of YAP-depleted cells was unexpected. To understand the potential mechanism through which these YAP-KD cells continue to sense their immediate matrix stiffness, we imaged for focal adhesions because they directly connect the cells to the matrix. Indeed, we found that the average FA size of YAP-KD cells on stiff secondary ECM was more than 5

times higher compared to the values on the soft secondary ECM, regardless of primary ECM stiffness (Fig. 4.7a,h). We also found similar mechanosensitive but memory-independent trends for actin fiber alignment, and pMLC expression (Fig. 4.7a,f,g, 4.17). These results demonstrate that YAP-KD cells are unable store a mechanical memory of past stiffness due to hampered YAP activity, but continue to sense the immediate matrix stiffness through focal adhesions.

4.4 Discussion

Plasticity in motile cells is manifested by variable modes of migration depending on the surrounding microenvironment [98]. In particular, cancer cells are uniquely equipped to exploit their plasticity to drive tumor invasion through distinct tissues. It has recently been identified that human mesenchymal stem cells store memory of their past exposure to matrix stiffness [53]. However, in migratory cells, it has remained a mystery whether their mechanics-regulated state persists even after they move to a new environment. If the mechanical properties of the tumor microenvironment are found to mechanically "train" the escaping cells, impacting their future ability to metastasize, this could be a critical missing piece of the puzzling unpredictability of cancer adaptation. To address this important gap in our understanding, we asked whether collectively migrating cells retain a mechanical memory of their past ECM stiffness. Through measurements of collective cell migration across dual-stiffness substrates, we show that priming of an epithelial cell colony on a stiff ECM enhances its future collective migration even on a soft ECM. We also show that the enhanced migration of stiff-primed cells on soft ECM is not caused by the mechanosensitive differences in cell spreading, proliferation, or other mechanical signaling transmitted from

the back of the monolayer. Indeed, when the cell colony was only primed for one day, the stiff primary ECM in the back was not able to enhance migration of cells on the soft secondary ECM. Thus, the memory-dependent cell migration is orchestrated by preserving the priming-enabled mechano-activated state of the cells onto the secondary ECM. We found that less than 2 days of priming of cells on the primary ECM showed a substantially reduced mechanical memory-based migration. It is likely that the cells require 2-3 days to respond to matrix stiffness and accordingly localize YAP (nuclear or cytoplasmic). Indeed, our measurements of nuclear YAP localization within cells of a monolayer cultured on the stiff PA gel (50 kPa) at different time points reveal that YAP activation continues to rise over 3 days (Fig. 4.18). Furthermore, this time-sensitive storage of YAP-dependent memory within the cells might require a transcriptional program, which is consistent with previous studies on mechanical-memory dependent responses of stem cells [53].

Given that YAP is a classic transducer of ECM [36] and its known role in storing memory in stem cells [53], we measured its ability to retain information of past ECM stiffness in collectively migrating cells. We found that the stiffer priming predicted higher nuclear YAP localization – a sign of persistent mechano-regulated YAP activity. After YAP depletion, cell migration did not depend on past matrix stiffness, i.e., the mechanical memory was significantly diminished in these cells. According to our data, the YAP-depletion blunts mechanical memory without a significant loss of cellular mechanosensitivity to the immediate matrix stiffness.

Our results point to a conceptual framework of mechanical memory-dependent cell migration in which migration-related cellular forces may be independently influenced by two factors (Fig. 4.8). First, the priming-dependent YAP activity directly regulates actomyosin forces and migration (results from Figs. 4.4,4.6). In cancer associated fibroblasts (CAFs), YAP

activation has been shown to enhance and maintain a positive feedback loop with actomyosin contractility [54]. Similarly, fluid shear-dependent YAP activation has been shown to enhance protrusions required for migration [99]. Second, cells are able to sense immediate matrix stiffness through adhesions, despite YAP depletion (results from Fig. 4.7). Previously, we have shown that YAP-depleted CAFs maintain the mechano-sensitive SNAIL1 protein level [85], which indicates that the cells are able to adopt alternate YAP-independent pathways for sensing matrix stiffness.

In summary, our findings of the mechanical memory in migratory cells expand the basic understanding of cellular mechanotransduction, beyond the current framework of studying cell migration in the context of only the immediate microenvironment. The insight that stiffness of the past ECM can influence future collective migration opens the door to new hypotheses for a wide array of biological processes, wherever microenvironment-dependent cell motility plays a role, such as morphogenesis, wound healing, and cancer cell invasion. Given that our experiments were conducted with immortalized epithelial cells, the presented conclusions may not be directly applicable for mesenchymal-like cells in vivo. Furthermore, since our measurements were performed in an idealized model system of a homogeneous cell monolayer in contact with a 2D substrate, the conclusions drawn here may not be directly applicable for in vivo conditions of 3D microenvironments and heterogeneous cell populations. The knowledge of memory-storing abilities of invasive cancer cells and associated signaling targets may open new avenues for therapeutics and predictive modeling by exploiting their dependency on the primary tumor microenvironment and tuning their ability to adapt to foreign tissue environments.

4.5 Materials and Methods

4.5.1 Modular Polyacrylamide (mPA) Hydrogels.

Contiguous polyacrylamide gels with distinct modules were fabricated through a step-by-step polymerization of PA solutions of defined compositions. Precursor solutions containing the acrylamide:bisacrylamide (A:B)22 percentages of 4:0.2% or 12:0.6% were mixed with 0.5% Ammonium Persulphate (APS) and 0.05% Tetramethylethylenediamine (TEMED) [86]. Red fluorescent carboxylate-modified beads of 200-nm diameter were added at 0.1% concentration to the stiff PA precursor solution to identify the interface between dissimilar ECM modules. Next, a volume of PA precursor solution sufficient to achieve a gel thickness of 100μm was dispensed on the coverslip and covered with a glass slide of defined size to confine the spreading of the PA droplet in each module of the substrate. This step was repeated for all three modules (Fig. 4.1A) to fabricate the entire modular PA (mPA) hydrogel substrate. After polymerization, mPA gels were sterilized for 1 hour under UV light. Subsequently, PA gels were treated with 0.5mg/ml of sulfosuccinimidyl 6-(4'-azido-2'-nitrophenylamino) hexanoate (Sulfo-SANPAH) (Thermo Fisher Scientific) prepared in 50mM HEPES buffer (Santa Cruz Biotechnologies) and crosslinked to the mPA surface upon activation with 365 nm UV for 10 minutes. After extensive washing with 50 mM HEPES buffer, mPA gels incubated with 0.05 mg/ml of rat-tail collagen type I (Santa Cruz Biotechnologies) overnight at 4℃.

4.5.2 Mechanical Characterization of PA Hydrogels.

Atomic Force Microscopy (AFM) measurements of polyacrylamide gels were performed using an MFP-3D-BIO atomic force microscope (Asylum Research, Santa Barbara, CA). Olympus TR400PB AFM probes with an Au/Cr coated silicon nitride cantilever and pyramidal tip were used, with spring constants ranging from 20–30 pN/nm, as measured by thermal calibration. Force maps in square regions of 40 μm edge length, with 169 points per force map, were taken at equal spacing across the gels. Measurements were performed across at least 4 mm length on each side of the interface dividing the primary and secondary ECM regions, as shown in Fig 4.9. Elastic moduli were extracted from force curves using a modified Hertz model.38-40

4.5.3 Cell Culture and Collective Migration Assay.

Human mammary epithelial non-tumorigenic MCF10A cells were cultured in DMEM-F12 (GE Healthcare Life Sciences), supplemented with 5% horse serum (Invitrogen), 20 ng/mL epidermal growth factor (EGF, Miltenyi Biotec Inc), 0.5 mg/mL hydrocortisone (Sigma-Aldrich), 100 ng/mL cholera toxin (Sigma-Aldrich), 10 ug/mL insulin (Sigma-Aldrich), and 1% (v/v) penicillin-streptomycin (Sigma-Aldrich). Tumorigenic mammary epithelial MCF7 cells were grown in DMEM (Sigma-Aldrich) containing 10% fetal bovine serum (FBS), 1% (v/v) penicillin-streptomycin (Sigma-Aldrich), and 1% non-essential amino acids (0.1mM). Human epidermoid carcinoma A431 cells were grown in DMEM (Sigma-Aldrich) containing 10% fetal bovine serum (FBS), 1% (v/v) penicillin-streptomycin (Sigma-Aldrich), 1% sodium pyruvate (Sigma-Aldrich), 1% sodium bicarbonate (Sigma-Aldrich), and 1% non-essential amino acids (0.1mM). A PDMS stencil was designed and fabricated with a rectangular

opening in the center, restricting the culture of epithelial monolayer within the central module (primary ECM) of mPA substrate (Fig. 4.1A). PDMS stencils were air-dried, cleaned with 70% ethanol, and sterilized under UV light for 2 hours. Afterwards, stencils were passivated overnight, with a sterile solution of 1% Pluronic and 1% Bovine serum albumin (BSA) in Phosphate buffered saline (PBS) to avoid cell adhesion, and carefully positioned on the PA gels. Cell suspension with 2×104 cells was dispensed into the PDMS reservoir covering the primary ECM region and left to grow for a prescribed duration of preconditioning (1, 2, or 3 days) at 37℃ in a 5% CO2 humidified incubator. After this incubation period, the PDMS stencil was lifted off to allow cell sheet to migrate into the adjoining secondary ECM. Additional media was added to each well.

For proliferation inhibition experiments, cells were treated with 2mM thymidine (Sigma-Aldrich) after at least 6 hours of cell seeding, to allow adequate attachment of cells to the substrate. For ROCK inhibition, cells were treated with 40μM of Y-27632 dihydrochloride (TOCRIS) 3 days after cell seeding. To disturb the actin integrity and microtubule polarization cells were treated with 0.5μM of latrunculin A and Nocodazole (Sigma-Aldrich) for 1hr, after 3 days of priming. Afterwards, fresh media was added to cells and migration tracking were performed for two days. For calcium chelation experiments, cells were incubated with 4mM of EGTA (Sigma-Aldrich) after 3 days of priming. To inhibit myosin light kinase activity, cells were with 20μM of ML-7 (Sigma-Aldrich).

4.5.4 Live-cell Imaging.

Time-lapse microscopy was initiated 2 hours after removing the PDMS and time-lapse imaging was carried out in the phase contrast on an inverted microscope (Zeiss Cell Observer)

equipped with an incubator capable of maintaining an environment with 37℃ temperature and 5% CO_2 level. Images were acquired with a 10× objective. Two successive images of the same field were taken at 20 minutes time interval. Motion of the leading edge of the cell monolayer was manually tracked by recording the position of cell border using a homemade macro in ImageJ. Subsequently, coordinates of the leading edge were imported into a custom-made program in MATLAB and its advancement was calculated by averaging the distance of each point on the leading edge from the primary-secondary ECM interface. Leading edge speed was defined as the ratio of the leading edge advanced distance and the time course of migration. For single cell migration analysis, individual movies were imported to ImageJ software (National Institutes of Health), and single cell migration trajectories were extracted using the Manual Tracking plugin. Cell migration tracks were subsequently analyzed to obtain migration speed and velocity angle distribution. Migration speed was calculated as a ratio between the sum of distances traveled by the cell between each time point and the total time. For each time interval, we calculated the angle between instantaneous velocity vector and the x axis and plotted the angle distribution for the entire migration tracking period.

4.5.5 Particle Image Velocimetry (PIV) and Monolayer Dynamics.

PIV analyses were performed to quantify spatiotemporal velocity distribution of velocity magnitudes by implementing the PIVlab package in MATLAB.23 To reduce the systematic biases in subpixel resolution, we iteratively implemented PIV up to three passes of 64, 32, and 16 pixel windows with 50% overlap between adjacent windows. Displacement and velocity (displacement/time interval) vectors were calculated by comparing the displacement of a window between two successive images. The velocity field was expressed in μm/min.

PIV analysis yielded two components of velocity at each point (i,j), namely lateral (u_{ij}, perpendicular to the direction of group migration) and axial (v_{ij}, along the direction of group migration). After obtaining the velocity vectors, cell alignment and cell-cell coordination were evaluated in terms of order parameter and correlation length [88]. The order parameter was defined as the cosine of the angle that the velocity vector makes with the principal direction of migration. The order parameter varies from +1 (for velocity vectors parallel to the strip and directed along the direction of migration of the cell sheet) to -1 (for vectors that are directed opposite to the direction of migration of the cell front) through 0 (for vectors aligning perpendicular to the direction of the monolayer migration). Correlation lengths were calculated according to the method described earlier [92]. To demonstrate the time evolution of monolayer motion, we plotted kymographs of velocity magnitude and order parameter. After obtaining the velocity vectors for every pixel of the monolayer at a given time instant, kymographs were computed by averaging the velocity magnitude and order parameter of individual velocity vectors in x direction over the y coordinates in every time point for time period of 12 hours after monolayer crossed the interface.

4.5.6 Quantitative Image Analysis.

Captured z-stacks were imported to ImageJ (NIH) as LSM files, and the stacks were projected with the maximum intensity setting. To quantify the subcellular YAP activity, the mean fluorescence intensity of YAP was measured in the nucleus and the cytoplasm. Afterwards, the nuclear-to-cytoplasmic ratio of YAP intensity was computed and plotted to compare YAP localization across experimental conditions. At least 50 cells were randomly selected for analysis from 10-15 field of views selected from three independent experiments. To quantify pMLC intensity, the mean protein intensity per cell in a given region of interest

(ROI) was calculated after subtracting the background signal (corresponding to the intensity of the negative control) from the total intensity in the z-stack (sum over all pixels of slices) and normalized to the number of cells in the corresponding region. The number of cells in a given ROI obtained by manually counting cell nuclei in the maximum projected DAPI image. To compare between different experimental conditions, pMLC intensity per cell values were normalized to the values obtained for cells cultured on control stiff substrates. To analyze actin fiber orientation, the resulting z-projected image of phalloidin (sum over all pixels of slices) for each cell was analyzed using OrientationJ algorithm in ImageJ. For each cell, the degree of stress fiber alignment was calculated in terms of coherency in ImageJ, which varies between 0, indicating isotropic distribution, and 1, indicating highly aligned structures. Subsequently, the average fiber alignment was obtained by normalizing to the fiber alignment value obtained for cells cultured on stiff control substrates. The mean spreading areas of cells located at different distances with respect to the leading edge on various substrates were measured using ImageJ software by manually drawing the border of cell from phalloidin images and evaluating the resulting cell areas. At least 40 cells were analyzed from three independent experiments for each experimental condition. To measure the size of focal adhesion (FA) areas, confocal z-stack images of paxillin staining were acquired. The z-projected images were subsequently binarized based on a manually selected threshold level that enabled better visualization of all FAs containing paxillin. FA surface area was measured from binarized images using ImageJ. To obtain an average FA area, at least 15 cells were analyzed for each experimental condition.

4.5.7 shRNA Knockdown.

To deplete YAP, the lentiviral pFLRu vector containing either Scramble (shSCRM) or anti-YAP shRNA (shYAP), and puromycin resistance was used.27 HEK293T cells were cultured in DMEM (Gibco) supplemented with 10% heat-inactivated fetal bovine serum (FBS), 200 μML-glutamine (Cellgro), and penicillin-streptomycin. HEK293T cells were transfected with lentiviral DNA using the TransIT LT1 transfection reagent per manufacturer protocol (Mirus). Virus was harvested from 293T media 48 hours after transfection and used to transduce MCF10A cells. Puromycin (Sigma-Aldrich) was used in cell selection and maintenance at a concentration of 1.5 μg/mL.

4.5.8 Western Blotting.

Cells were lysed in RIPA buffer (50 mM Tris, pH 8.0, 150 mM NaCl, 1% NP-40, 0.5% sodium deoxycholate, 0.1% SDS) supplemented with 200 nM phenylmethylsulfonyl fluoride (PMSF), 2 μg/ml aprotinin/leupeptin, 2 μM pepstatin A, 1 mM Na3VO4, and 2 mM NaF. The lysates were cleared by centrifugation at 12,000 rpm at 4C for 10 min, and the concentrations were determined by Bradford assay (Bio-Rad). Equal amounts of protein were boiled in SDS sample buffer for 10min, resolved by SDS 10%-PAGE, and transferred to polyvinylidene difluoride (PVDF) membranes (Millipore) in transfer buffer (25 mM Tris, 192 mM glycine, 5% methanol). The membranes were blocked with TBST (25 mM Tris, pH 7.4, 150 mM NaCl, 2 mM KCl, 0.5% Tween 20) containing 5% skim milk powder or bovine serum albumin (BSA) and probed overnight with the indicated primary antibodies. Bound antibodies were detected by horseradish peroxidase (HRP)-conjugated secondary antibodies and developed with SuperSignal West Pico and/or West Femto enhanced chemiluminescence (ECL)

(Pierce). Images were collected on a Bio-Rad ChemiDoc XRS+ and analyzed using ImageJ software (NIH). The following antibodies were used: rabbit anti-YAP/TAZ (Cell Signaling Technology, D24E4, mAb#8418; 1:1000), mouse anti-Actin (Sigma, A5316; 1:25,000).

4.5.9 Statistical Analysis.

Unless specified otherwise, results are reported as the mean ± Standard Error (SE). To identify the significant differences between two experimental conditions, an F-test was performed to determine whether equal variance could be assumed. Next, Student's t-test was used to determine significant differences between two groups. All statistical analyses were performed using the Data Analysis toolbox in Microsoft Excel. Differences were considered to be significant for $P<0.05$.

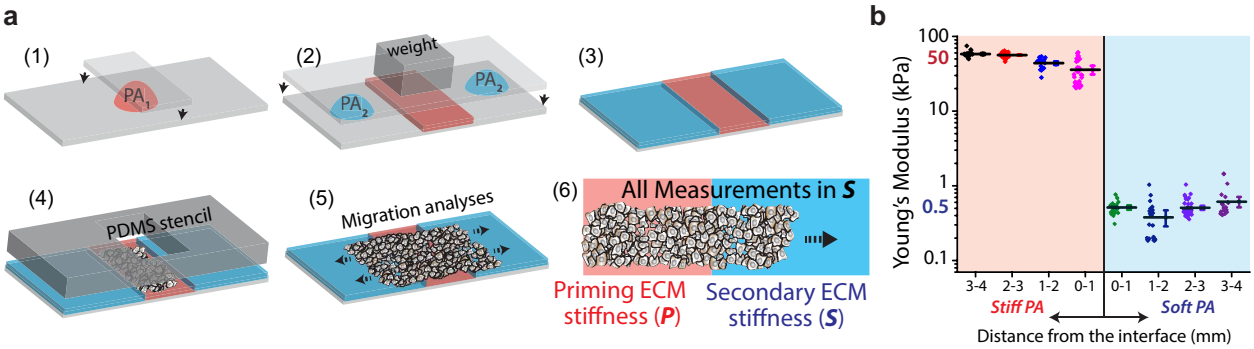

Figure 4.1: **Contiguous substrate with regions of dissimilar stiffness.** (a) Schematic describing the fabrication steps of mPA substrates of heterogeneous stiffness through modular polymerization of PA solutions of distinct compositions, resulting in dissimilar ECM stiffness in adjoining primary and secondary regions. (b) Atomic Force Microscopy (AFM) measurements of Young's Modulus of PA gels plotted in logarithmic scale at different locations within a substrate with dissimilar primary and secondary ECM regions. Stiffness values are averaged over 1mm length intervals and plotted along with scattered data points and error bars (SEM). N>150. Data is included from at least 3 different PA gels, in which the left side was intended to be stiff (acrylamide/bisacrylamide=12/0.6%) and right side as soft (acrylamide/bisacrylamide=4/0.2%) matrix.

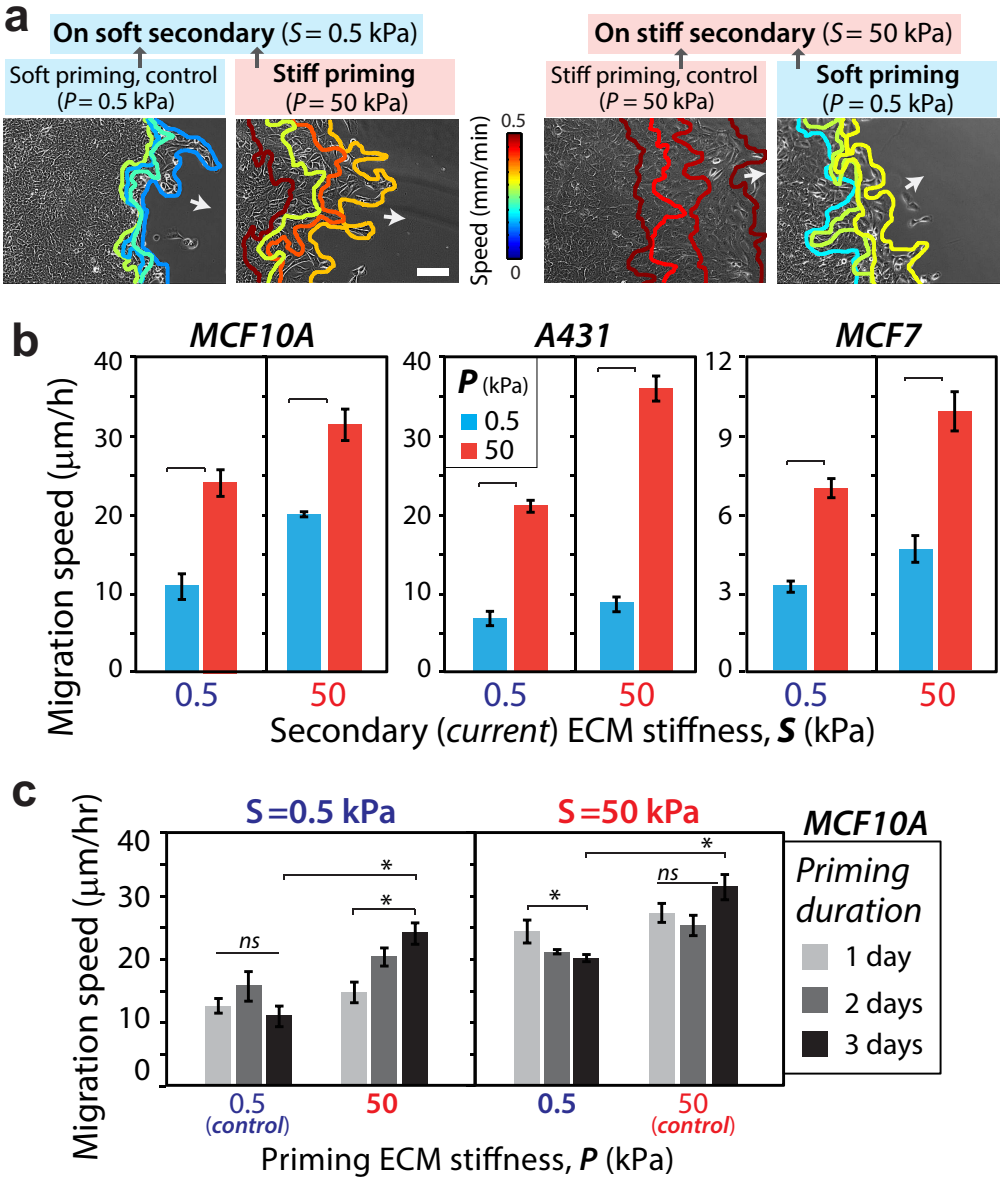

Figure 4.2: **Collective cell migration speed depends on priming by the past ECM stiffness.** (a) Representative leading-edge tracks of monolayers of MCF10A cells recorded for 12 hours (3 h interval) in the secondary ECM after 3-day priming, with color-coding for migration speed. Arrows indicate direction of migration. Scale bar = 100 μm. (b) Average leading-edge migration speed for MCF10A, A431, and MCF7 cells migrating on secondary ECM (S=0.5, 50 kPa) after defined priming (P=0.5, 50 kPa). Horizontal square brackets denote statistical significance ($p<0.05$). N>15. (c) Average leading-edge migration speed for MCF10A cells after 1, 2, or 3 days of priming. *$p<0.05$, with horizontal square brackets denoting statistical significance ($p<0.05$). ns=no significant difference. Error bars = SEM. N>10.

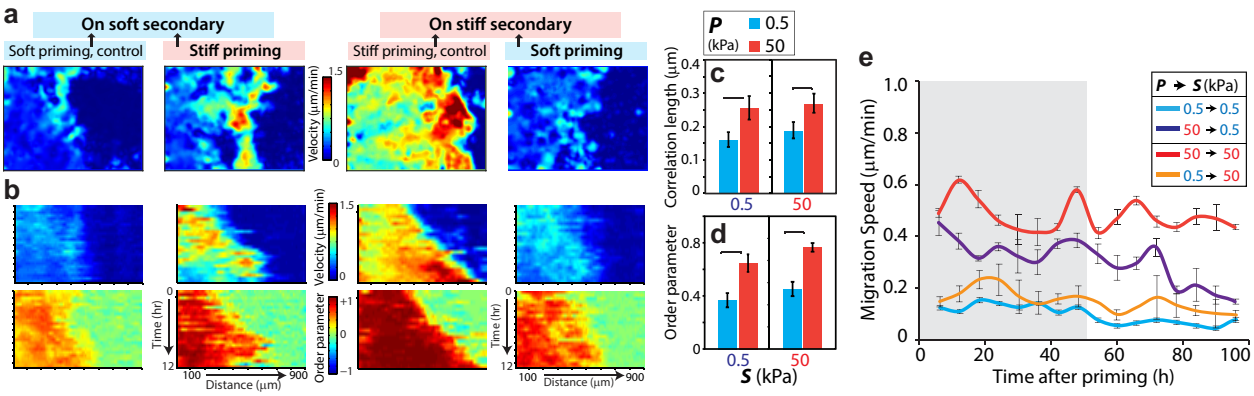

Figure 4.3: **Monolayer dynamics and temporal variation of memory-dependent migration.** (a) Heatmap showing the spatial distribution of velocity magnitude at a given time instant for MCF10A cell monolayer migration. (b) Position-time kymographs of velocity magnitude and order parameter obtained from PIV analysis demonstrate the time evolution of monolayer motion. Kymographs were computed by averaging the velocity magnitude and order parameter of individual velocity vectors in the x-direction over the y-coordinate for every time point. Average (c) correlation length and (d) order parameter of the velocity vectors. Horizontal square brackets denote statistical significance ($p<0.05$). $N>15$. (e) Plot describes the leading-edge migration speed over time, tracked for 96 h in secondary ECM after 3-day priming of cell monolayer. All bar plots are averaged over quantities measured in the first 48h of migration (depicted by the shaded region), which corresponds to the period of maximal memory. $N>10$. Error bars = SEM.

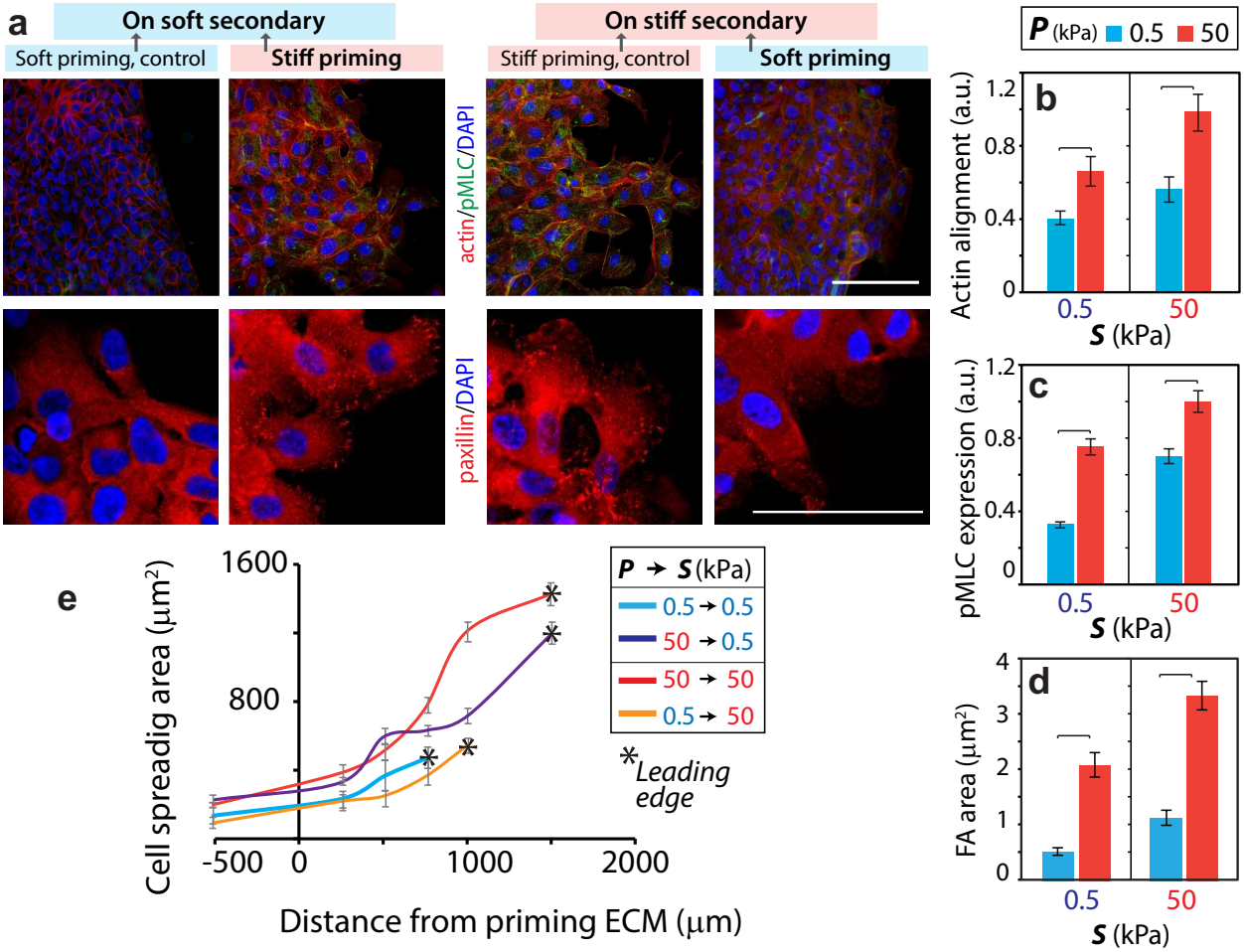

Figure 4.4: **Cytoskeletal machinery in memory-dependent migration.** (a) Immunofluorescent staining of pMLC (green), F-actin (phalloidin, red), and DAPI (blue) in top-panel and paxillin (red) and DAPI (blue) in bottom-panel for MCF10A cell monolayers on the secondary ECM after 2 days of migration (post-priming). Scale bar = 100 μm. Quantification of (b) actin fiber alignment, (c) normalized pMLC expression, and (d) FA area. N>40. (e) Variation of spreading area of single cells within the MCF10A cell monolayer relative to the distance from the leading edge showing stiffness-independent cell spreading in the primary ECM. N>25. Error bars = SEM.

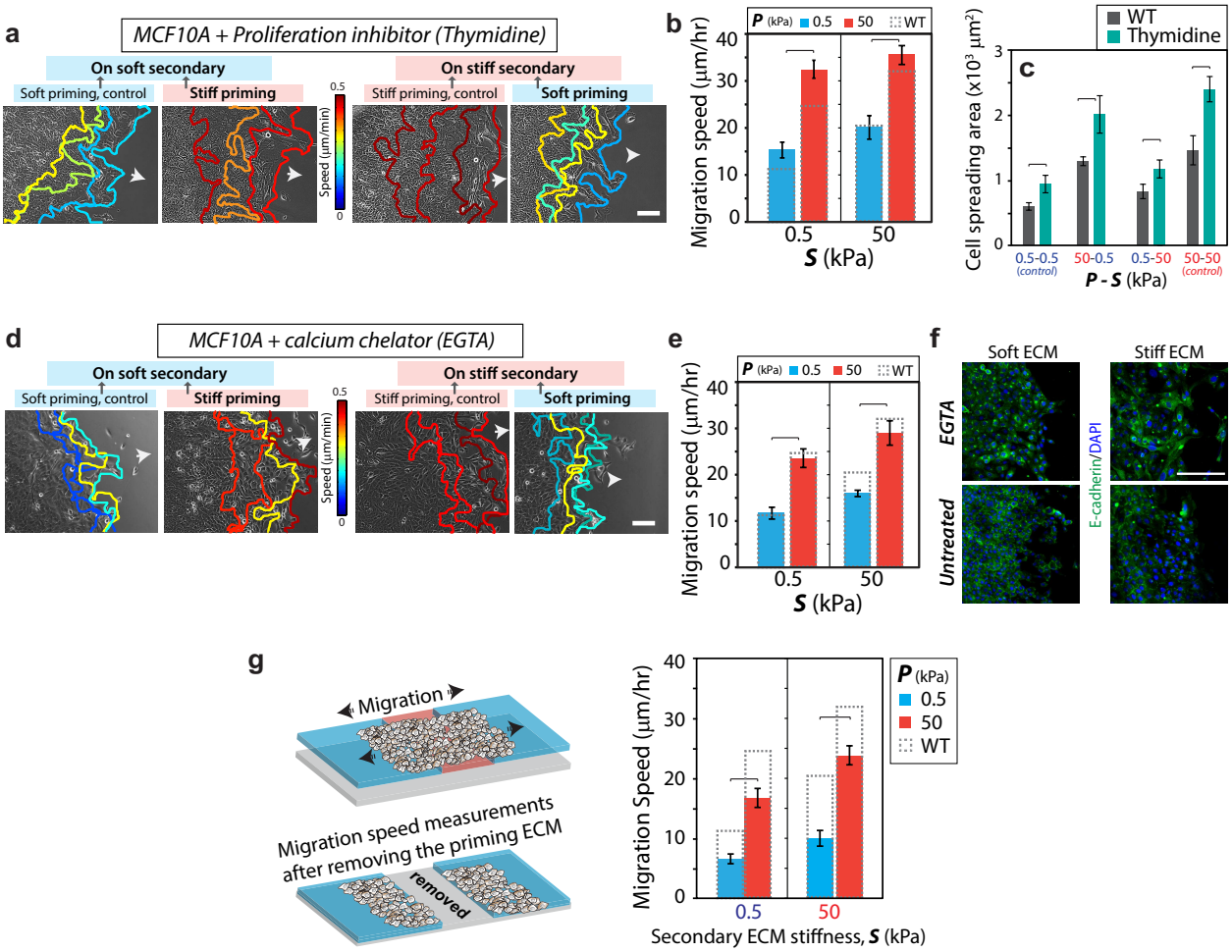

Figure 4.5: **Memory-dependent migration is not regulated by proliferation or long-distance signal transmission.** Representative leading-edge tracks of monolayers of MCF10A cells after treatment with (a) 2mM thymidine, a proliferation inhibitor, and (d) 4mM EGTA, a calcium chelator, recorded for 12 hours (3 h interval) in the secondary ECM, with color-coding for migration speed. Arrows indicate direction of migration. (b) Average leading edge migration speed for proliferation-inhibited cells. Columns with dashed outline represent the migration speed for control untreated MCF10A cells. N>15. (c) Average spreading area of individual cells in the secondary ECM with and without proliferation inhibition. N>30. (e) Average leading edge migration speed for EGTA-treated cells. N>15. (f) Immunofluorescent staining for E-cadherin (green) and DAPI (blue) in untreated and EGTA-treated MCF10A cells showing dysfunctional cell-cell junctions after EGTA treatment. Scale bars = 100 μm. (g) After 3-day priming and additional 1 day of migration in the secondary ECM, the primary ECM region is entirely removed. Leading-edge migration speed in the secondary ECM (right panel) shows preservation of memory-dependent migration despite a complete loss of communication with the primary region. N>15. Horizontal brackets denote statistical significance, $p<0.05$. Error bars = SEM.

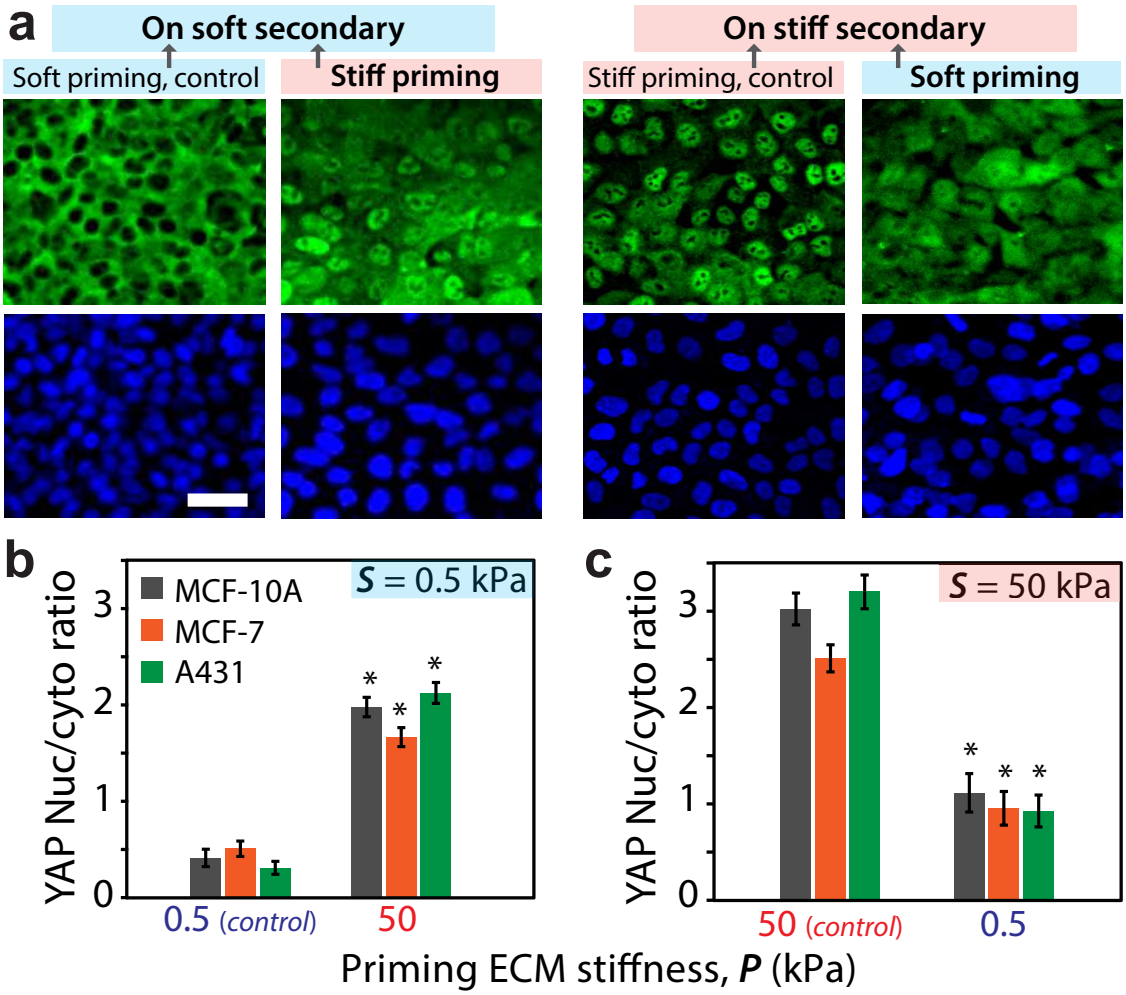

Figure 4.6: **YAP activity depends on past ECM stiffness.** (a) Immunofluorescent staining of MCF10A cells for YAP (green) and DAPI (blue) illustrating the subcellular localization of YAP for the monolayer migrating on secondary ECM, after priming. Scale bar = 50 μm. (b,c) Average nuclear-to-cytoplasmic ratio of the YAP fluorescent intensity for MCF10A, MCF7, and A431 cells within the monolayer. *p<0.05 with respect to control ECMs of homogeneous stiffness. Error bars = SEM. N>40.

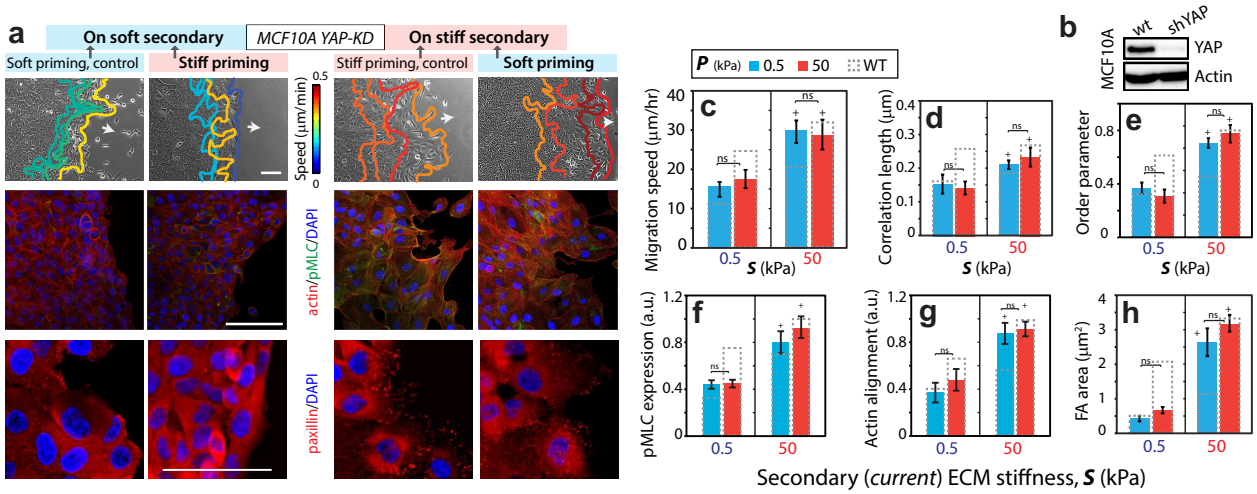

Figure 4.7: **Memory-independent collective migration of YAP-depleted MCF10A cells.** (a) Leading edge tracks of monolayer of YAP-depleted MCF10A cells are plotted at 3 h interval during their post-priming migration on secondary ECMs. Immunofluorescent staining for F-actin (red), pMLC (green), paxillin (red), and DAPI (blue). Scale bars = 100 μm. (b) MCF10A cells expressing either shSCRM (wt) or shYAP RNAi were lysed and subjected to Western blotting with anti-YAP and anti-Actin antibodies. Average (c) leading edge migration speed, (d) correlation length, and (e) order parameter, N>15, and normalized (f) pMLC expression and (g) actin alignment, N>40, and (h) FA area, N>20, for varying ECM configurations. Columns with dashed outline represent corresponding values for wildtype MCF10A cells. Horizontal brackets denote statistical significance ($p<0.05$). ns=no significant difference. Error bars = SEM.

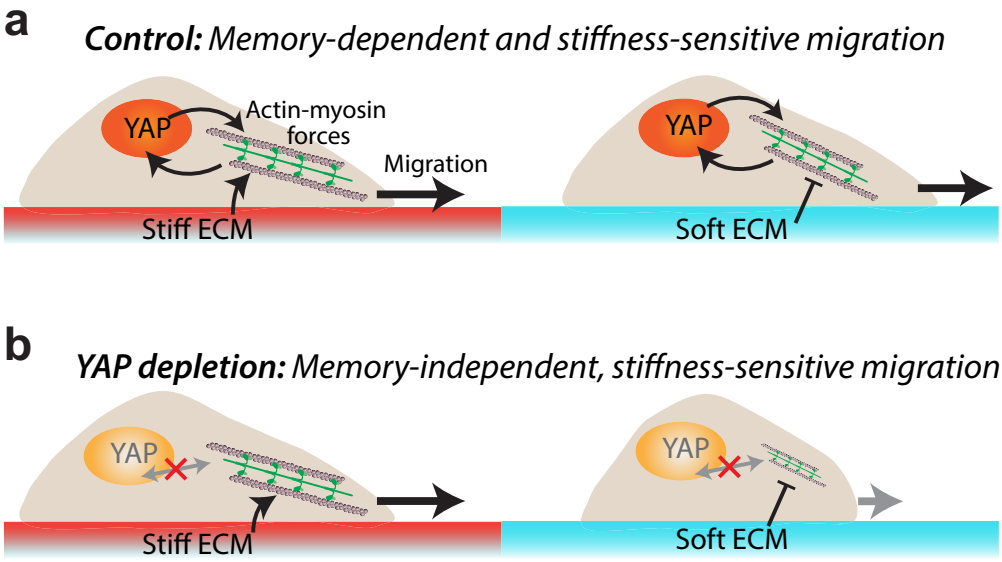

Figure 4.8: **Conceptual framework for memory regulation.** (a) Priming-dependent YAP activity regulates cellular forces and dictates the memory-dependent migration. (b) YAP-depletion abrogates memory, but direct FA-mediated contact with the immediate ECM preserve mechano-sensitivity.

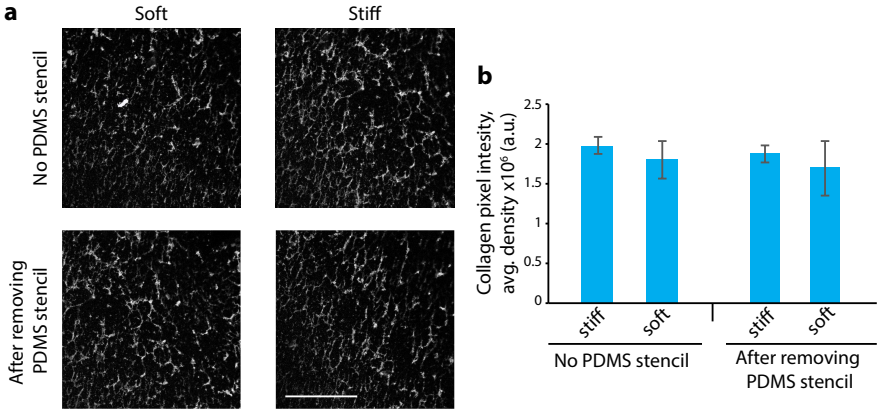

Figure 4.9: **Collagen I coating on soft and stiff PA gels.** Rat-tail collagen type I was labelled using Sulfo-Cyanine5 NHS ester. (a) Soft (0.5 kPa) and stiff (50 kPa) PA gels coated with 0.05 mg/ml of this labeled collagen I were imaged. Scale bar = 50 μm. (b) The integrated density of pixel intensity measured from these collagen images shows insignificant difference in soft and stiff gels. These measurements were repeated after removing the PDMS stencil, which shows robust collagen coating with or without PDMS interaction.

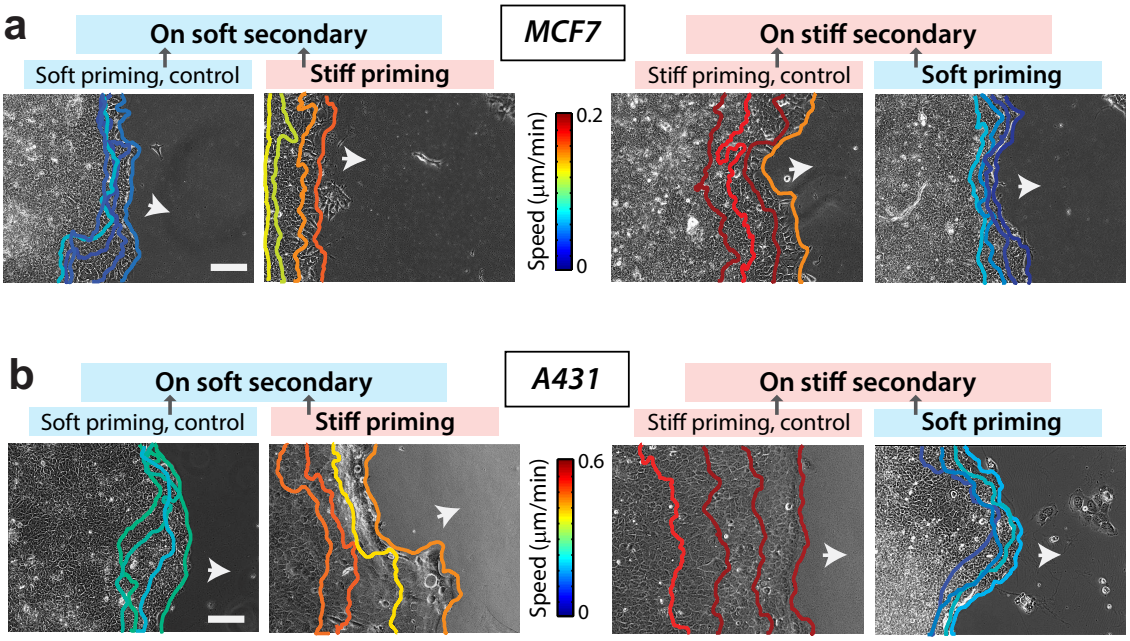

Figure 4.10: **Leading-edge tracks of representative monolayers of MCF7 and A431 cells.** Plots describing the leading-edge tracks of representative monolayers of (a) MCF7 and (b) A431 cells recorded for 12 hours after entering the secondary ECM; tracks color-coded based on the leading-edge migration speed. In each case, four representative leading-edge tracks at 3 h interval are plotted on soft or stiff secondary ECMs, which were previously primed on stiff or soft primary ECMs. Arrows indicate the general direction of migration. Scale bar = 100 μm.

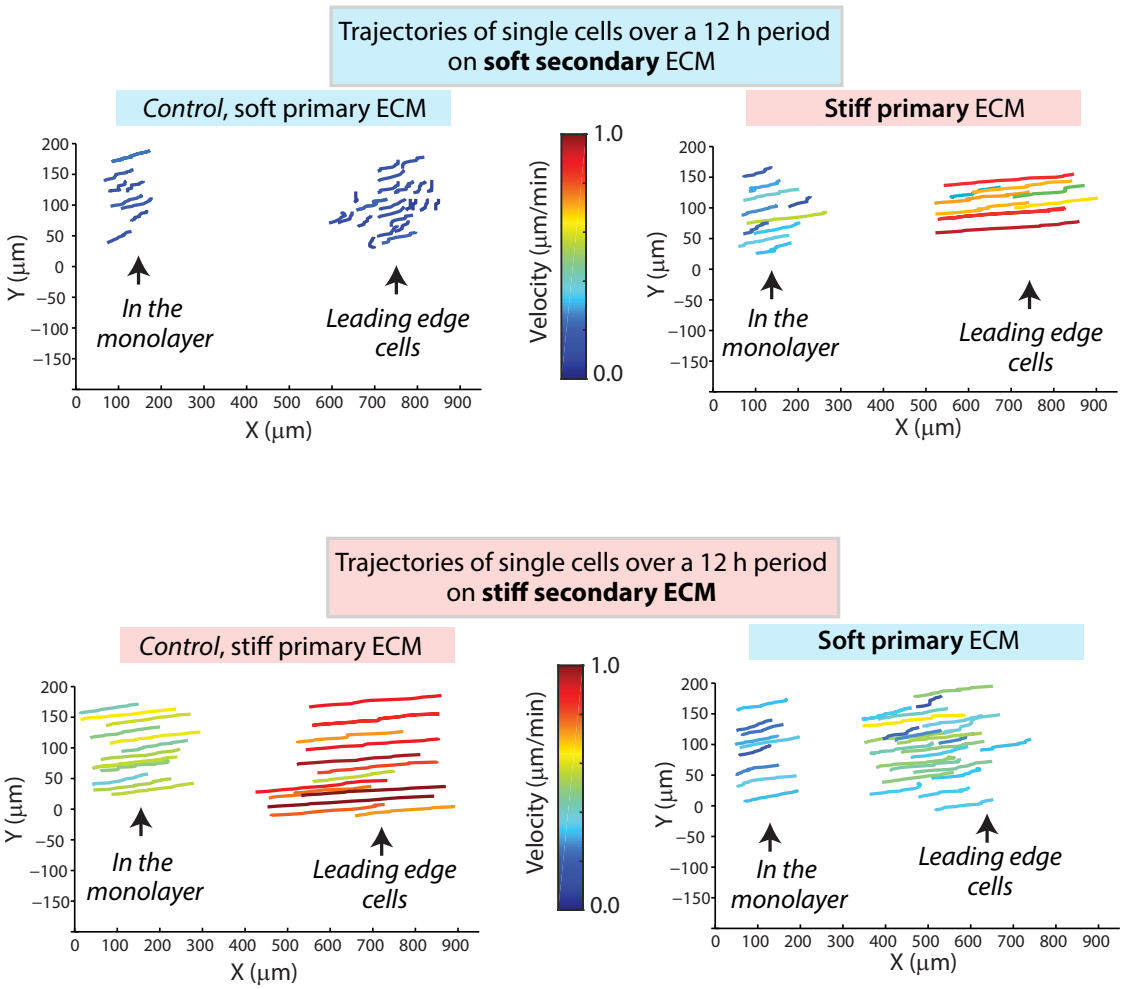

Figure 4.11: **Single cell trajectories within the migrating monolayer.** Trajectories of single cells located at the leading edge and inside (at least 200 μm behind the leading edge) the monolayer of cells migrating on soft (top) or stiff (bottom) secondary ECM, after priming on soft or stiff primary ECMs. Tracks were color coded according to migration speed for each cell.

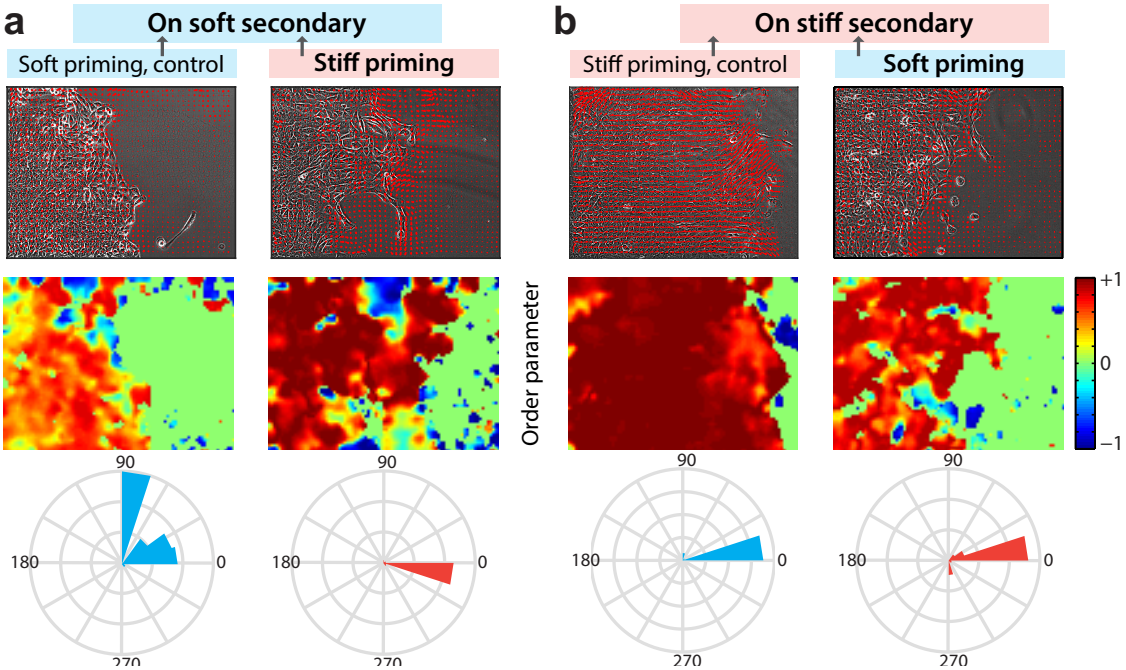

Figure 4.12: **Alignment of single cell movement within the monolayer depends on primary ECM stiffness.** Heatmap of order parameter (top row), vector field describing the direction of velocity vectors (middle row), and rose plot (bottom row) demonstrating the distribution of the angle between the instantaneous velocity vector and the x-axis, which were obtained by analyzing the trajectories of single cells for MCF-10A monolayer migrating on (a) soft and (b) stiff secondary ECM after being primed on soft or stiff primary ECMs.

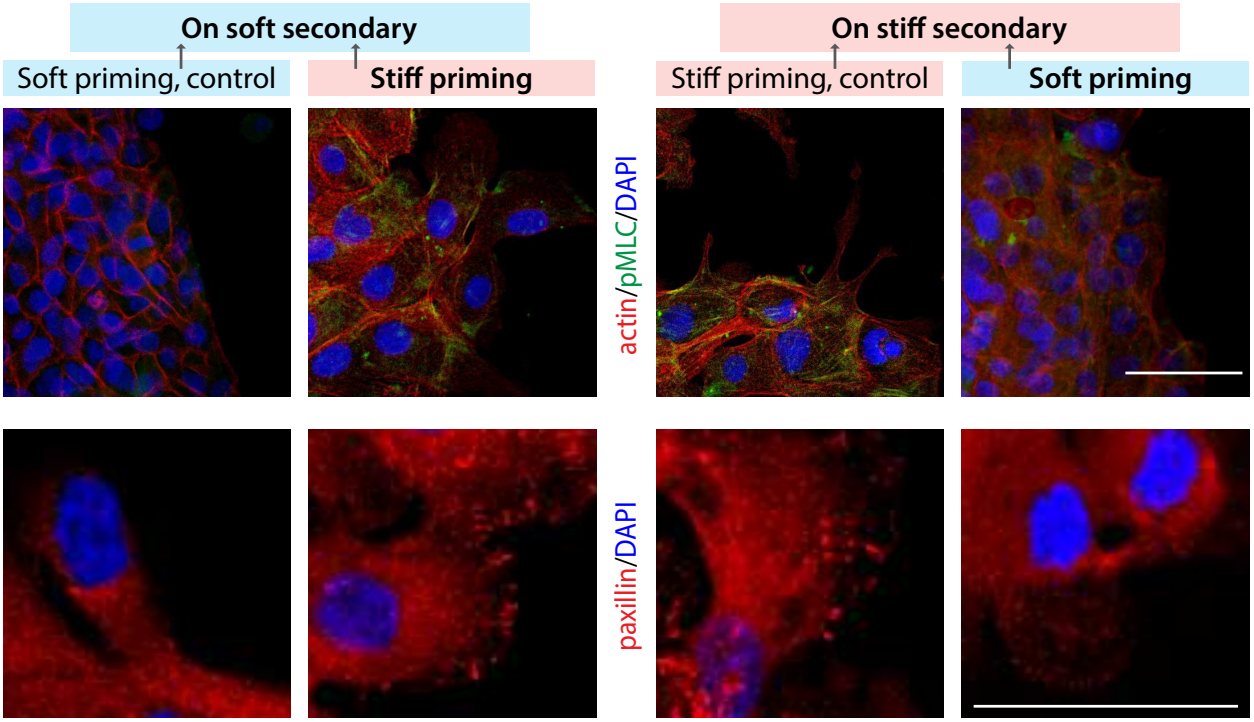

Figure 4.13: Immunofluorescent staining of pMLC (green), F-actin (phalloidin, red), and DAPI (blue) in top-panel and paxillin (red) and DAPI (blue) in bottom-panel for MCF10A cell monolayers on the secondary ECM after 2 days of migration (post-priming). Repeated from Figure 4 with higher resolution to better visualize actin fibers and punctate focal adhesions. Scale bar = 50 μm.

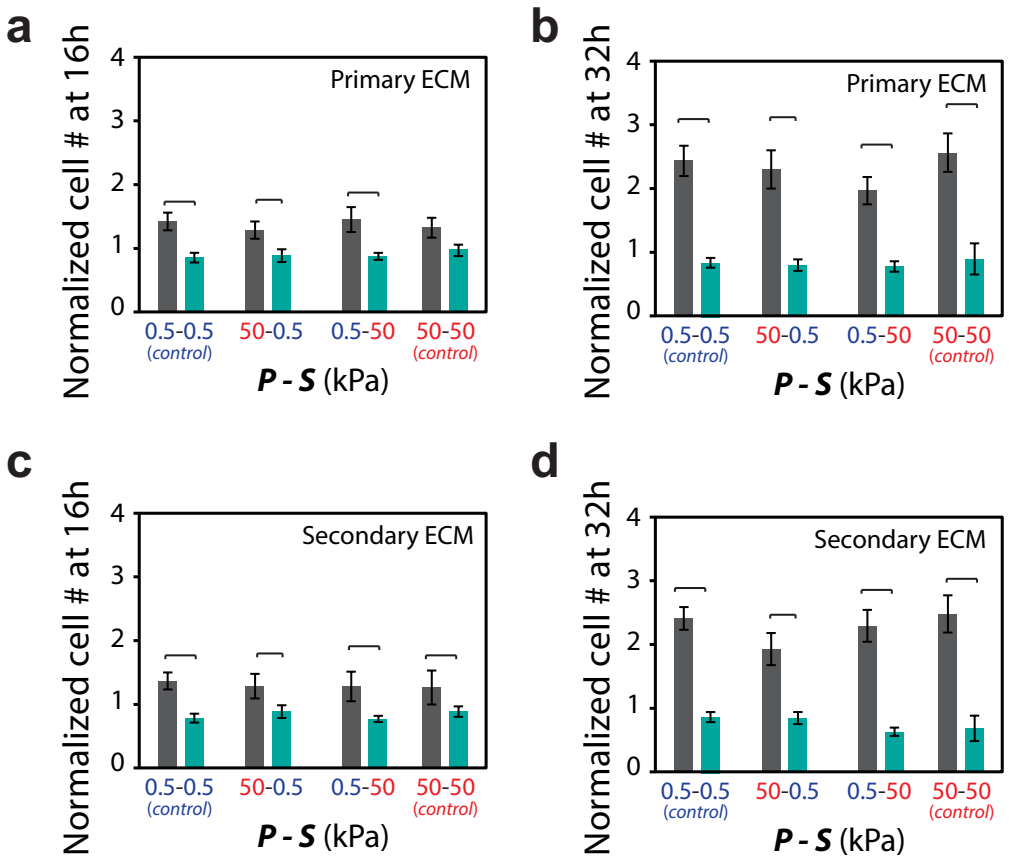

Figure 4.14: **Number of cells after proliferation inhibition.** (a-d) Normalized number of cells within a defined region of interest in primary and secondary ECMs at time t=16h and t=32h from t=0, the start of migration (post-priming), for thymidine-treated and untreated cells. Normalization performed relative to the number of cells in the ROI at t=0. Horizontal brackets denote statistical significance ($P<0.05$). Error bars = SEM.

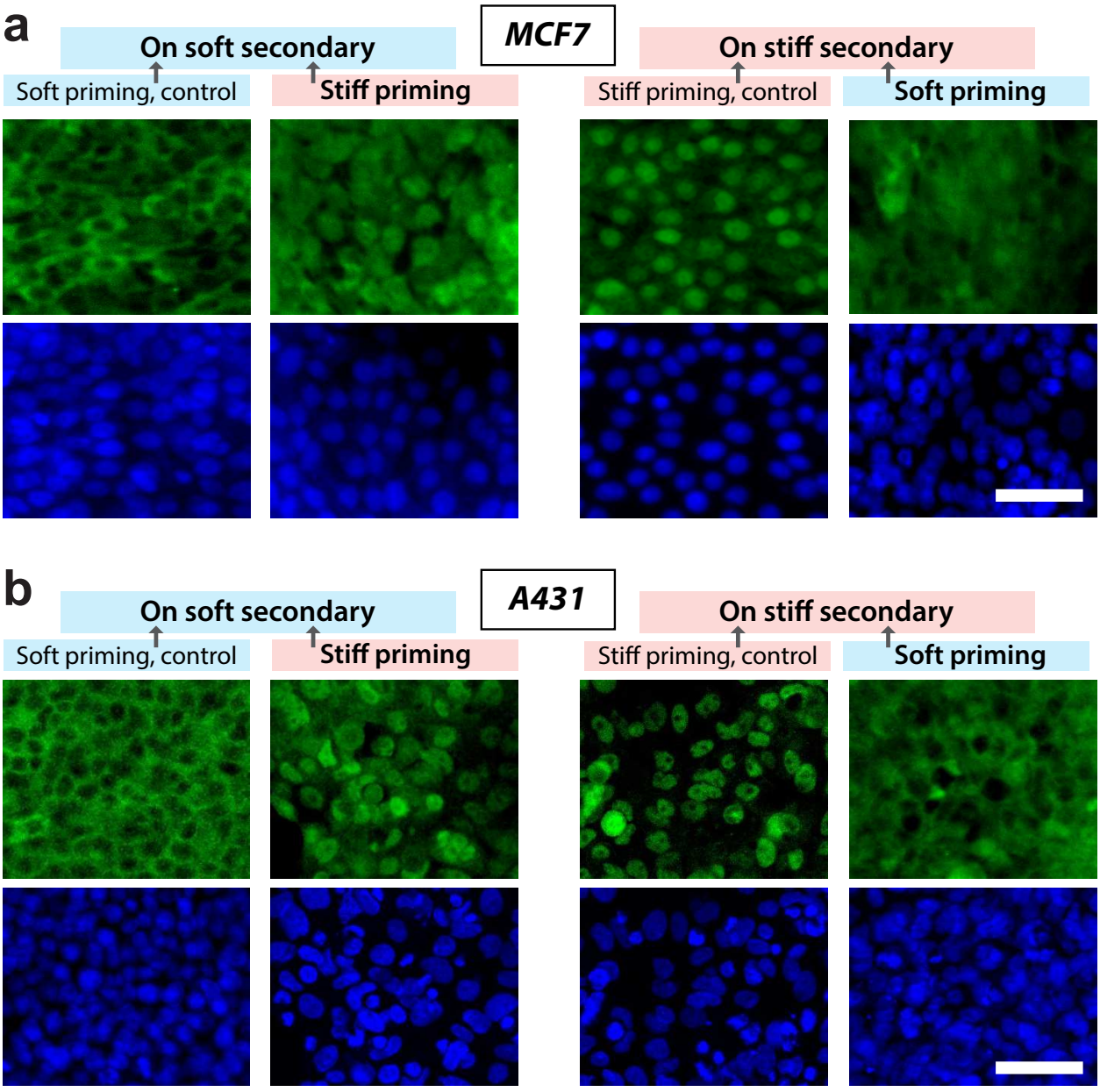

Figure 4.15: **Representative images of YAP expression in MCF7 and A431 cells.** Immunofluorescent staining of MCF-7 (a) and A431 (b) cells for YAP (green) and DAPI (blue), illustrates the subcellular localization of YAP for the monolayer migrating on soft and stiff secondary ECM, after priming on soft or stiff ECMs. Scale bar = 50 μm.

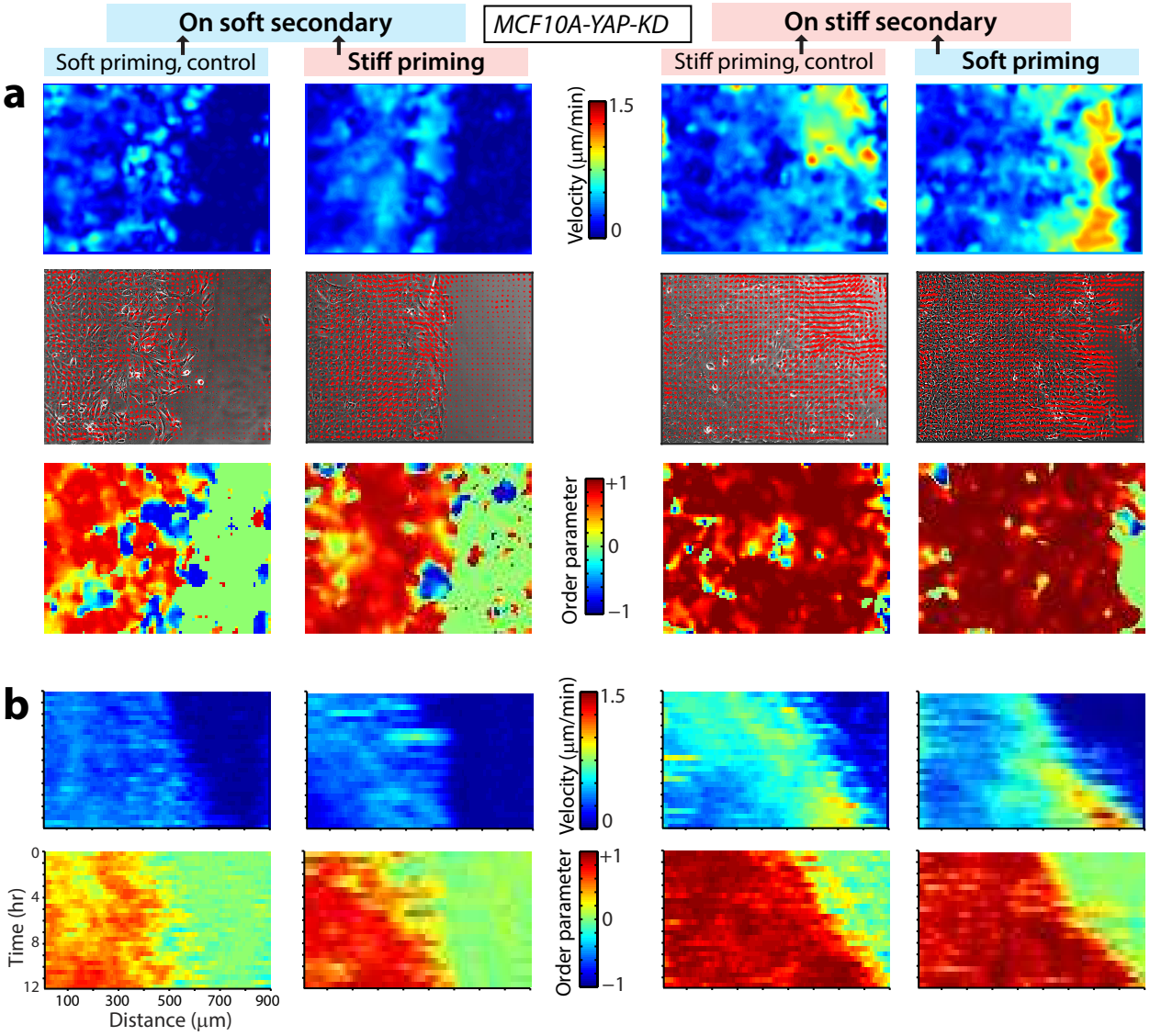

Figure 4.16: **Monolayer dynamics in YAP-depleted MCF10A cells.** (a) Heatmap showing the spatial distribution of velocity magnitude (top row), vector field describing the direction of velocity vectors (middle row), and order parameter (bottom row) at a given time instant for YAP-depleted MCF10A cell monolayer migrating on soft (left column) and stiff (right column) secondary ECMs, after priming on either stiff or soft primary ECMs. (b) Position-time kymographs of velocity magnitude and order parameter obtained from PIV analysis for corresponding ECM conditions described above to demonstrate the time evolution of monolayer motion. Kymographs were computed by averaging the velocity magnitude and order parameter of individual velocity vectors in the x direction over the y coordinate for every time point.

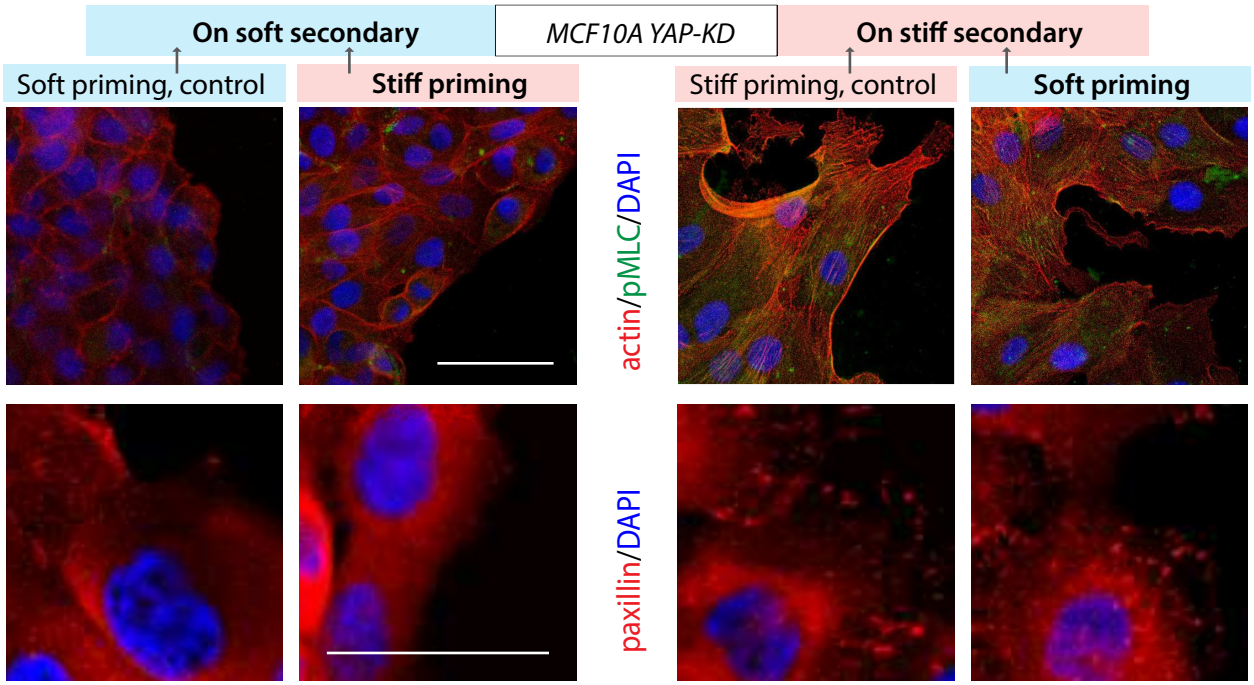

Figure 4.17: Immunofluorescent staining of pMLC (green), F-actin (phalloidin, red), and DAPI (blue) in top-panel and paxillin (red) and DAPI (blue) in bottom-panel for YAP-depleted MCF10A cell monolayers on the secondary ECM after 2 days of migration (post-priming). Repeated from Figure 7 with higher resolution to better visualize actin fibers and punctate focal adhesions. Scale bar = 50 μm.

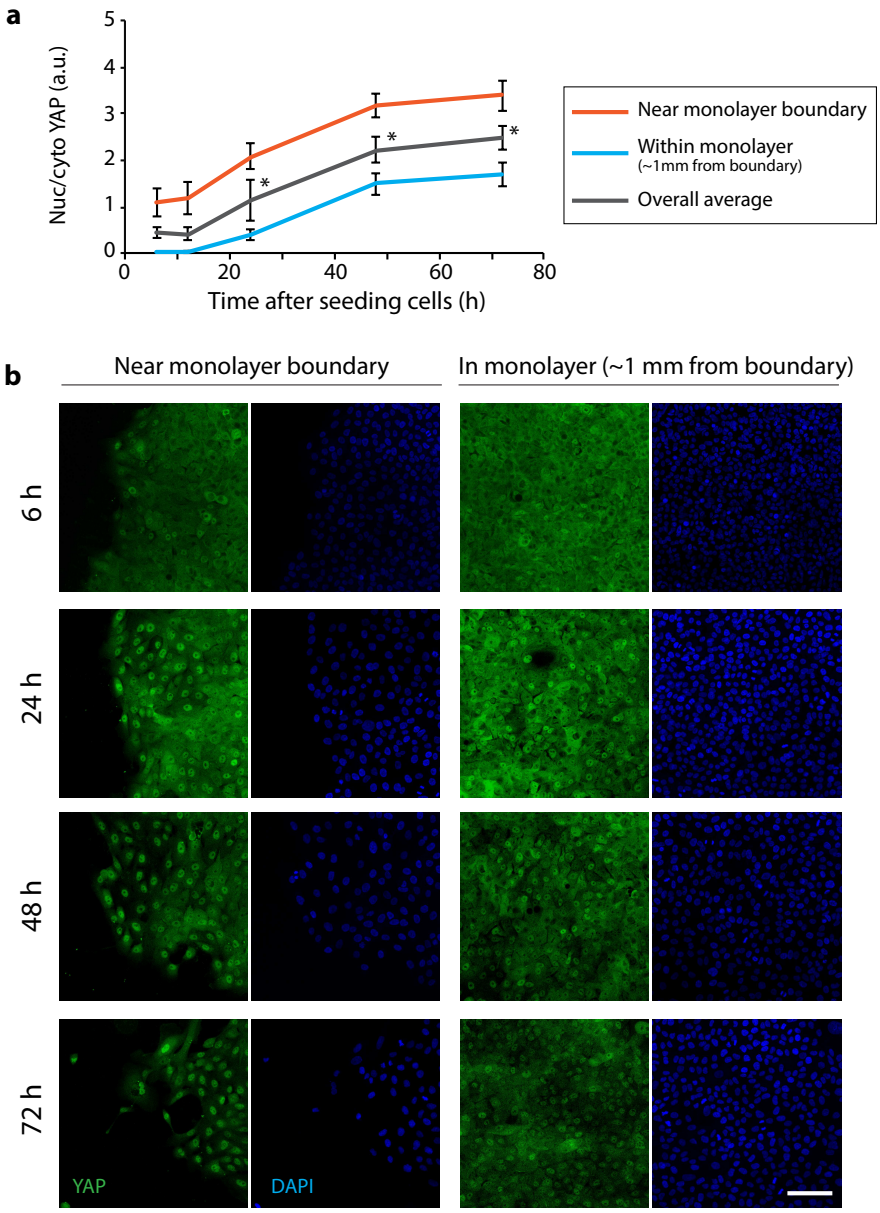

Figure 4.18: **Time progression of YAP nuclear localization on stiff ECM.** (a) Average nuclear-to-cytoplasmic ratio of the YAP fluorescent intensity for MCF10A cells cultured on stiff ECM (50kPa) located near the monolayer boundary (within 0.4mm; blue line), within the monolayer (1mm away from the monolayer boundary; red line), and overall average (regardless of location relative to the monolayer boundary; gray line) as a function of time after cell seeding. Mean values were obtained by analyzing > 40 cells from > 4 different fields of views from >2 experiments. $^*p < 0.05$ with respect to the 6h data point. Error bars=SEM. (b) Immunofluorescent staining of MCF10A cells for YAP (green) and DAPI (blue) illustrating the nuclear localization of YAP for the monolayer cultured on stiff ECM, fixed at 6, 24, 48 and 72 h after seeding. Scale bar = 100 μm.

Bibliography

[1] Jean Paul Thiery, Hervé Acloque, Ruby YJ Huang, and M Angela Nieto. Epithelial-mesenchymal transitions in development and disease. *cell*, 139(5):871–890, 2009.

[2] Jing Yang and Robert A Weinberg. Epithelial-mesenchymal transition: at the crossroads of development and tumor metastasis. *Developmental cell*, 14(6):818–829, 2008.

[3] Amit Pathak and Sanjay Kumar. Biophysical regulation of tumor cell invasion: moving beyond matrix stiffness. *Integrative Biology*, 3(4):267–278, 2011.

[4] Amit Pathak and Sanjay Kumar. Independent regulation of tumor cell migration by matrix stiffness and confinement. *Proceedings of the National Academy of Sciences*, 109(26):10334–10339, 2012.

[5] Peter Friedl, Erik Sahai, Stephen Weiss, and Kenneth M Yamada. New dimensions in cell migration. *Nature reviews Molecular cell biology*, 13(11):743–747, 2012.

[6] Martin A Schwartz and Christopher S Chen. Deconstructing dimensionality. *Science*, 339(6118):402–404, 2013.

[7] Seunghan Oh, Karla S Brammer, YS Julie Li, Dayu Teng, Adam J Engler, Shu Chien, and Sungho Jin. Stem cell fate dictated solely by altered nanotube dimension. *Proceedings of the National Academy of Sciences*, 106(7):2130–2135, 2009.

[8] Eric M Balzer, Ziqiu Tong, Colin D Paul, Wei-Chien Hung, Kimberly M Stroka, Amanda E Boggs, Stuart S Martin, and Konstantinos Konstantopoulos. Physical confinement alters tumor cell adhesion and migration phenotypes. *The FASEB Journal*, 26(10):4045–4056, 2012.

[9] Casey M Kraning-Rush, Shawn P Carey, Marsha C Lampi, and Cynthia A Reinhart-King. Microfabricated collagen tracks facilitate single cell metastatic invasion in 3d. *Integrative Biology*, 5(3):606–616, 2013.

[10] Matthew J Paszek, Nastaran Zahir, Kandice R Johnson, Johnathon N Lakins, Gabriela I Rozenberg, Amit Gefen, Cynthia A Reinhart-King, Susan S Margulies, Micah Dembo,

David Boettiger, et al. Tensional homeostasis and the malignant phenotype. *Cancer cell*, 8(3):241–254, 2005.

[11] Kandice R Levental, Hongmei Yu, Laura Kass, Johnathon N Lakins, Mikala Egeblad, Janine T Erler, Sheri FT Fong, Katalin Csiszar, Amato Giaccia, Wolfgang Weninger, et al. Matrix crosslinking forces tumor progression by enhancing integrin signaling. *Cell*, 139(5):891–906, 2009.

[12] Spencer C Wei, Laurent Fattet, Jeff H Tsai, Yurong Guo, Vincent H Pai, Hannah E Majeski, Albert C Chen, Robert L Sah, Susan S Taylor, Adam J Engler, et al. Matrix stiffness drives epithelial-mesenchymal transition and tumour metastasis through a twist1-g3bp2 mechanotransduction pathway. *Nature cell biology*, 17(5):678–688, 2015.

[13] Amanda Lance, Chih-Chao Yang, Muthulekha Swamydas, Delphine Dean, Sandy Deitch, Karen JL Burg, and Didier Dréau. Increased extracellular matrix density decreases mcf10a breast cell acinus formation in 3d culture conditions. *Journal of tissue engineering and regenerative medicine*, 2013.

[14] Marilyn C Markowski, Ashley C Brown, and Thomas H Barker. Directing epithelial to mesenchymal transition through engineered microenvironments displaying orthogonal adhesive and mechanical cues. *Journal of biomedical materials research Part A*, 100(8):2119–2127, 2012.

[15] Ashley C Brown, Vincent F Fiore, Todd A Sulchek, and Thomas H Barker. Physical and chemical microenvironmental cues orthogonally control the degree and duration of fibrosis-associated epithelial-to-mesenchymal transitions. *The Journal of pathology*, 229(1):25–35, 2013.

[16] KangAe Lee, Qike K Chen, Cecillia Lui, Magdalena A Cichon, Derek C Radisky, and Celeste M Nelson. Matrix compliance regulates rac1b localization, nadph oxidase assembly, and epithelial–mesenchymal transition. *Molecular biology of the cell*, 23(20):4097–4108, 2012.

[17] Jennifer L Leight, Michele A Wozniak, Sophia Chen, Michelle L Lynch, and Christopher S Chen. Matrix rigidity regulates a switch between tgf-β1–induced apoptosis and epithelial–mesenchymal transition. *Molecular biology of the cell*, 23(5):781–791, 2012.

[18] Simone Spaderna, Otto Schmalhofer, Falk Hlubek, Geert Berx, Andreas Eger, Susanne Merkel, Andreas Jung, Thomas Kirchner, and Thomas Brabletz. A transient, emt-linked loss of basement membranes indicates metastasis and poor survival in colorectal cancer. *Gastroenterology*, 131(3):830–840, 2006.

[19] Koert P Dingemans. What's new in the ultrastructure of tumor invasion in vivo? *Pathology-Research and Practice*, 183(6):792–808, 1988.

[20] Amit Pathak and Sanjay Kumar. Transforming potential and matrix stiffness co-regulate confinement sensitivity of tumor cell migration. *Integrative Biology*, 5(8):1067–1075, 2013.

[21] Gema Moreno-Bueno, Héctor Peinado, Patricia Molina, David Olmeda, Eva Cubillo, Vanesa Santos, José Palacios, Francisco Portillo, and Amparo Cano. The morphological and molecular features of the epithelial-to-mesenchymal transition. *Nature protocols*, 4(11):1591–1613, 2009.

[22] Jules J Berman. Tumor classification: molecular analysis meets aristotle. *BMC cancer*, 4(1):10, 2004.

[23] Theresa A Ulrich, Elena M de Juan Pardo, and Sanjay Kumar. The mechanical rigidity of the extracellular matrix regulates the structure, motility, and proliferation of glioma cells. *Cancer research*, 69(10):4167–4174, 2009.

[24] David Sarrió, Socorro María Rodriguez-Pinilla, David Hardisson, Amparo Cano, Gema Moreno-Bueno, and José Palacios. Epithelial-mesenchymal transition in breast cancer relates to the basal-like phenotype. *Cancer research*, 68(4):989–997, 2008.

[25] Jun Oyanagi, Takashi Ogawa, Hiroki Sato, Shouichi Higashi, and Kaoru Miyazaki. Epithelial-mesenchymal transition stimulates human cancer cells to extend microtubule-based invasive protrusions and suppresses cell growth in collagen gel. *PLoS One*, 7(12):e53209, 2012.

[26] Yukiko Nakaya, Erike W Sukowati, Yuping Wu, and Guojun Sheng. Rhoa and microtubule dynamics control cell–basement membrane interaction in emt during gastrulation. *Nature cell biology*, 10(7):765–775, 2008.

[27] Benjamin Geiger, Joachim P Spatz, and Alexander D Bershadsky. Environmental sensing through focal adhesions. *Nature reviews Molecular cell biology*, 10(1):21–33, 2009.

[28] Daniel Choquet, Dan P Felsenfeld, and Michael P Sheetz. Extracellular matrix rigidity causes strengthening of integrin–cytoskeleton linkages. *Cell*, 88(1):39–48, 1997.

[29] Sharmistha Saha, Xinrui Duan, Laying Wu, Pang-Kuo Lo, Hexin Chen, and Qian Wang. Electrospun fibrous scaffolds promote breast cancer cell alignment and epithelial-mesenchymal transition. *Langmuir*, 28(4):2028, 2012.

[30] Bartley J Gill, Don L Gibbons, Laila C Roudsari, Jennifer E Saik, Zain H Rizvi, Jonathon D Roybal, Jonathan M Kurie, and Jennifer L West. A synthetic matrix with independently tunable biochemistry and mechanical properties to study epithelial morphogenesis and emt in a lung adenocarcinoma model. *Cancer research*, 72(22):6013–6023, 2012.

[31] Laura Foroni, Francesco Vasuri, Sabrina Valente, Chiara Gualandi, Maria Letizia Focarete, Giacomo Caprara, Mariastella Scandola, Antonia D'Errico-Grigioni, and Gianandrea Pasquinelli. The role of 3d microenvironmental organization in mcf-7 epithelial–mesenchymal transition after 7 culture days. *Experimental cell research*, 319(10):1515–1522, 2013.

[32] Venkat Maruthamuthu and Margaret L Gardel. Protrusive activity guides changes in cell-cell tension during epithelial cell scattering. *Biophysical journal*, 107(3):555–563, 2014.

[33] Clifford P Brangwynne, Frederick C MacKintosh, Sanjay Kumar, Nicholas A Geisse, Jennifer Talbot, L Mahadevan, Kevin K Parker, Donald E Ingber, and David A Weitz. Microtubules can bear enhanced compressive loads in living cells because of lateral reinforcement. *J Cell Biol*, 173(5):733–741, 2006.

[34] Sangmyung Rhee, Hongmei Jiang, Chin-Han Ho, and Frederick Grinnell. Microtubule function in fibroblast spreading is modulated according to the tension state of cell–matrix interactions. *Proceedings of the National Academy of Sciences*, 104(13):5425–5430, 2007.

[35] Patricia T Yam, Cyrus A Wilson, Lin Ji, Benedict Hebert, Erin L Barnhart, Natalie A Dye, Paul W Wiseman, Gaudenz Danuser, and Julie A Theriot. Actin–myosin network reorganization breaks symmetry at the cell rear to spontaneously initiate polarized cell motility. *J Cell Biol*, 178(7):1207–1221, 2007.

[36] Sirio Dupont, Leonardo Morsut, Mariaceleste Aragona, Elena Enzo, Stefano Giulitti, Michelangelo Cordenonsi, Francesca Zanconato, Jimmy Le Digabel, Mattia Forcato, Silvio Bicciato, et al. Role of yap/taz in mechanotransduction. *Nature*, 474(7350):179–183, 2011.

[37] Dennis E Discher, Paul Janmey, and Yu-li Wang. Tissue cells feel and respond to the stiffness of their substrate. *Science*, 310(5751):1139–1143, 2005.

[38] Jayanta Debnath, Senthil K Muthuswamy, and Joan S Brugge. Morphogenesis and oncogenesis of mcf-10a mammary epithelial acini grown in three-dimensional basement membrane cultures. *Methods*, 30(3):256–268, 2003.

[39] Eloísa Díaz-Francés and Francisco J Rubio. On the existence of a normal approximation to the distribution of the ratio of two independent normal random variables. *Statistical Papers*, pages 1–15, 2013.

[40] Shelly R Peyton and Andrew J Putnam. Extracellular matrix rigidity governs smooth muscle cell motility in a biphasic fashion. *Journal of cellular physiology*, 204(1):198–209, 2005.

[41] Alejo E Rodríguez-Fraticelli and Fernando Martín-Belmonte. Mechanical control of epithelial lumen formation. *Small GTPases*, 4(2):136–140, 2013.

[42] Alexandre Saez, Marion Ghibaudo, Axel Buguin, Pascal Silberzan, and Benoît Ladoux. Rigidity-driven growth and migration of epithelial cells on microstructured anisotropic substrates. *Proceedings of the National Academy of Sciences*, 104(20):8281–8286, 2007.

[43] Julia E Sero, Heba Zuhair Sailem, Rico Chandra Ardy, Hannah Almuttaqi, Tongli Zhang, and Chris Bakal. Cell shape and the microenvironment regulate nuclear translocation of nf-κb in breast epithelial and tumor cells. *Molecular systems biology*, 11(3):790, 2015.

[44] Jin Hao, Yueling Zhang, Yating Wang, Rui Ye, Jingyi Qiu, Zhihe Zhao, and Juan Li. Role of extracellular matrix and yap/taz in cell fate determination. *Cellular signalling*, 26(2):186–191, 2014.

[45] Dawang Zhou, Claudius Conrad, Fan Xia, Ji-Sun Park, Bernhard Payer, Yi Yin, Gregory Y Lauwers, Wolfgang Thasler, Jeannie T Lee, Joseph Avruch, et al. Mst1 and mst2 maintain hepatocyte quiescence and suppress hepatocellular carcinoma development through inactivation of the yap1 oncogene. *Cancer cell*, 16(5):425–438, 2009.

[46] Bin Zhao, Xiaomu Wei, Weiquan Li, Ryan S Udan, Qian Yang, Joungmok Kim, Joe Xie, Tsuneo Ikenoue, Jindan Yu, Li Li, et al. Inactivation of yap oncoprotein by the hippo pathway is involved in cell contact inhibition and tissue growth control. *Genes & development*, 21(21):2747–2761, 2007.

[47] Toshiro Moroishi, Carsten Gram Hansen, and Kun-Liang Guan. The emerging roles of yap and taz in cancer. *Nature reviews Cancer*, 15(2):73–79, 2015.

[48] Bin Zhao, Li Li, Qunying Lei, and Kun-Liang Guan. The hippo–yap pathway in organ size control and tumorigenesis: an updated version. *Genes & development*, 24(9):862–874, 2010.

[49] Meng Sun, Fabian Spill, and Muhammad H Zaman. A computational model of yap/taz mechanosensing. *Biophysical journal*, 110(11):2540–2550, 2016.

[50] Sirio Dupont. Role of yap/taz in cell-matrix adhesion-mediated signalling and mechanotransduction. *Experimental cell research*, 343(1):42–53, 2016.

[51] Martina Fischer, Paul Rikeit, Petra Knaus, and Catherine Coirault. Yap-mediated mechanotransduction in skeletal muscle. *Frontiers in physiology*, 7:41, 2016.

[52] Boon Chuan Low, Catherine Qiurong Pan, GV Shivashankar, Alexander Bershadsky, Marius Sudol, and Michael Sheetz. Yap/taz as mechanosensors and mechanotransducers in regulating organ size and tumor growth. *FEBS letters*, 588(16):2663–2670, 2014.

[53] Chun Yang, Mark W Tibbitt, Lena Basta, and Kristi S Anseth. Mechanical memory and dosing influence stem cell fate. *Nature materials*, 13(6):645–652, 2014.

[54] Fernando Calvo, Nil Ege, Araceli Grande-Garcia, Steven Hooper, Robert P Jenkins, Shahid I Chaudhry, Kevin Harrington, Peter Williamson, Emad Moeendarbary, Guillaume Charras, et al. Mechanotransduction and yap-dependent matrix remodelling is required for the generation and maintenance of cancer-associated fibroblasts. *Nature cell biology*, 15(6):637–646, 2013.

[55] Fei Liu, David Lagares, Kyoung Moo Choi, Lauren Stopfer, Aleksandar Marinković, Vladimir Vrbanac, Clemens K Probst, Samantha E Hiemer, Thomas H Sisson, Jeffrey C Horowitz, et al. Mechanosignaling through yap and taz drive fibroblast activation and fibrosis. *American Journal of Physiology-Lung Cellular and Molecular Physiology*, pages ajplung–00300, 2014.

[56] Ken-Ichi Wada, Kazuyoshi Itoga, Teruo Okano, Shigenobu Yonemura, and Hiroshi Sasaki. Hippo pathway regulation by cell morphology and stress fibers. *Development*, 138(18):3907–3914, 2011.

[57] Samila Nasrollahi and Amit Pathak. Topographic confinement of epithelial clusters induces epithelial-to-mesenchymal transition in compliant matrices. *Scientific reports*, 6:18831–18831, 2015.

[58] Arupratan Das, Robert S Fischer, Duojia Pan, and Clare M Waterman. Yap nuclear localization in the absence of cell-cell contact is mediated by a filamentous actin-dependent, myosin ii-and phospho-yap-independent pathway during extracellular matrix mechanosensing. *Journal of Biological Chemistry*, 291(12):6096–6110, 2016.

[59] Amit Pathak. Scattering of cell clusters in confinement. *Biophysical Journal*, 111(7):1496–1506, 2016.

[60] T Oka, AP Schmitt, and M Sudol. Opposing roles of angiomotin-like-1 and zona occludens-2 on pro-apoptotic function of yap. *Oncogene*, 31(1):128–134, 2012.

[61] Nam-Gyun Kim, Eunjin Koh, Xiao Chen, and Barry M Gumbiner. E-cadherin mediates contact inhibition of proliferation through hippo signaling-pathway components. *Proceedings of the National Academy of Sciences*, 108(29):11930–11935, 2011.

[62] Richard O Hynes. The extracellular matrix: not just pretty fibrils. *Science*, 326(5957):1216–1219, 2009.

[63] Ann TJ Beliën, Paolo A Paganetti, and Martin E Schwab. Membrane-type 1 matrix metalloprotease (mt1-mmp) enables invasive migration of glioma cells in central nervous system white matter. *The Journal of cell biology*, 144(2):373–384, 1999.

[64] ELISABETTA M CASPANI, Diego Echevarria, Klemens Rottner, and J Victor Small. Live imaging of glioblastoma cells in brain tissue shows requirement of actin bundles for migration. *Neuron glia biology*, 2(02):105–114, 2006.

[65] Eric C Holland. Glioblastoma multiforme: the terminator. *Proceedings of the National Academy of Sciences*, 97(12):6242–6244, 2000.

[66] Eileen Puklin-Faucher and Michael P Sheetz. The mechanical integrin cycle. *Journal of cell science*, 122(2):179–186, 2009.

[67] Kenneth M Yamada and Edna Cukierman. Modeling tissue morphogenesis and cancer in 3d. *Cell*, 130(4):601–610, 2007.

[68] Paolo P Provenzano, Kevin W Eliceiri, and Patricia J Keely. Shining new light on 3d cell motility and the metastatic process. *Trends in cell biology*, 19(11):638–648, 2009.

[69] Donald E Ingber. Mechanical control of tissue morphogenesis during embryological development. *International Journal of Developmental Biology*, 50(2-3):255–266, 2003.

[70] William P Daley and Kenneth M Yamada. Ecm-modulated cellular dynamics as a driving force for tissue morphogenesis. *Current opinion in genetics & development*, 23(4):408–414, 2013.

[71] Wendy V Ingman, Jeff Wyckoff, Valerie Gouon-Evans, John Condeelis, and Jeffrey W Pollard. Macrophages promote collagen fibrillogenesis around terminal end buds of the developing mammary gland. *Developmental dynamics*, 235(12):3222–3229, 2006.

[72] Pepper Schedin and Patricia J Keely. Mammary gland ecm remodeling, stiffness, and mechanosignaling in normal development and tumor progression. *Cold Spring Harbor perspectives in biology*, 3(1):a003228, 2011.

[73] Sanjay Kumar and Valerie M Weaver. Mechanics, malignancy, and metastasis: the force journey of a tumor cell. *Cancer and Metastasis Reviews*, 28(1-2):113–127, 2009.

[74] Sri Ram Krishna Vedula, Man Chun Leong, Tan Lei Lai, Pascal Hersen, Alexandre J Kabla, Chwee Teck Lim, and Benoît Ladoux. Emerging modes of collective cell migration induced by geometrical constraints. *Proceedings of the National Academy of Sciences*, 109(32):12974–12979, 2012.

[75] Mei Rosa Ng, Achim Besser, Gaudenz Danuser, and Joan S Brugge. Substrate stiffness regulates cadherin-dependent collective migration through myosin-ii contractility. *J Cell Biol*, pages jcb–201207148, 2012.

[76] Raimon Sunyer, Vito Conte, Jorge Escribano, Alberto Elosegui-Artola, Anna Labernadie, Léo Valon, Daniel Navajas, José Manuel García-Aznar, José J Muñoz, Pere

Roca-Cusachs, et al. Collective cell durotaxis emerges from long-range intercellular force transmission. *Science*, 353(6304):1157–1161, 2016.

[77] Peter Friedl and Darren Gilmour. Collective cell migration in morphogenesis, regeneration and cancer. *Nature reviews Molecular cell biology*, 10(7):445–457, 2009.

[78] Victor D Varner and Celeste M Nelson. Cellular and physical mechanisms of branching morphogenesis. *Development*, 141(14):2750–2759, 2014.

[79] Andrew J Ewald, Audrey Brenot, Myhanh Duong, Bianca S Chan, and Zena Werb. Collective epithelial migration and cell rearrangements drive mammary branching morphogenesis. *Developmental cell*, 14(4):570–581, 2008.

[80] Peter Friedl and Stephanie Alexander. Cancer invasion and the microenvironment: plasticity and reciprocity. *Cell*, 147(5):992–1009, 2011.

[81] LE Dow, JS Kauffman, J Caddy, AS Peterson, SM Jane, SM Russell, and PO Humbert. The tumour-suppressor scribble dictates cell polarity during directed epithelial migration: regulation of rho gtpase recruitment to the leading edge. *Oncogene*, 26(16):2272–2282, 2007.

[82] Alice Nicolas, Benjamin Geiger, and Samuel A Safran. Cell mechanosensitivity controls the anisotropy of focal adhesions. *Proceedings of the National Academy of Sciences of the United States of America*, 101(34):12520–12525, 2004.

[83] Magdalena Chrzanowska-Wodnicka and Keith Burridge. Rho-stimulated contractility drives the formation of stress fibers and focal adhesions. *The Journal of cell biology*, 133(6):1403–1415, 1996.

[84] Myriam Reffay, Maria-Carla Parrini, Olivier Cochet-Escartin, Benoıt Ladoux, Axel Buguin, S Coscoy, François Amblard, Jacques Camonis, and Pascal Silberzan. Interplay of rhoa and mechanical forces in collective cell migration driven by leader cells. *Nature cell biology*, 16(3):217–223, 2014.

[85] Kun Zhang, Whitney R Grither, Samantha Van Hove, Hirak Biswas, Suzanne M Ponik, Kevin W Eliceiri, Patricia J Keely, and Gregory D Longmore. Mechanical signals regulate and activate snail1 protein to control the fibrogenic response of cancer-associated fibroblasts. *J Cell Sci*, 129(10):1989–2002, 2016.

[86] Chun-Min Lo, Hong-Bei Wang, Micah Dembo, and Yu-li Wang. Cell movement is guided by the rigidity of the substrate. *Biophysical journal*, 79(1):144–152, 2000.

[87] Matthew Raab, Joe Swift, PC Dave P Dingal, Palak Shah, Jae-Won Shin, and Dennis E Discher. Crawling from soft to stiff matrix polarizes the cytoskeleton and phosphoregulates myosin-ii heavy chain. *J Cell Biol*, 199(4):669–683, 2012.

[88] Matthew Raab and Dennis E Discher. Matrix rigidity regulates the microtubule network polarization in migration. *Cytoskeleton*, 2016.

[89] Robert S Fischer, Kenneth A Myers, Margaret L Gardel, and Clare M Waterman. Stiffness-controlled three-dimensional extracellular matrices for high-resolution imaging of cell behavior. *Nature protocols*, 7(11):2056–2066, 2012.

[90] Joanna L MacKay and Sanjay Kumar. Measuring the elastic properties of living cells with atomic force microscopy indentation. *Cell Imaging Techniques: Methods and Protocols*, pages 313–329, 2013.

[91] William Thielicke and Eize Stamhuis. Pivlab–towards user-friendly, affordable and accurate digital particle image velocimetry in matlab. *Journal of Open Research Software*, 2(1), 2014.

[92] Tamal Das, Kai Safferling, Sebastian Rausch, Niels Grabe, Heike Boehm, and Joachim P Spatz. A molecular mechanotransduction pathway regulates collective migration of epithelial cells. *Nature cell biology*, 17(3):276–287, 2015.

[93] Anne J Ridley, Martin A Schwartz, Keith Burridge, Richard A Firtel, Mark H Ginsberg, Gary Borisy, J Thomas Parsons, and Alan Rick Horwitz. Cell migration: integrating signals from front to back. *Science*, 302(5651):1704–1709, 2003.

[94] Dhananjay T Tambe, C Corey Hardin, Thomas E Angelini, Kavitha Rajendran, Chan Young Park, Xavier Serra-Picamal, Enhua H Zhou, Muhammad H Zaman, James P Butler, David A Weitz, et al. Collective cell guidance by cooperative intercellular forces. *Nature materials*, 10(6):469, 2011.

[95] Cédric Plutoni, Elsa Bazellieres, Maïlys Le Borgne-Rochet, Franck Comunale, Agusti Brugues, Martial Séveno, Damien Planchon, Sylvie Thuault, Nathalie Morin, Stéphane Bodin, et al. P-cadherin promotes collective cell migration via a cdc42-mediated increase in mechanical forces. *J Cell Biol*, 212(2):199–217, 2016.

[96] Veronica A Codelia, Gongping Sun, and Kenneth D Irvine. Regulation of yap by mechanical strain through jnk and hippo signaling. *Current Biology*, 24(17):2012–2017, 2014.

[97] Yunfeng Feng, Linghu Nie, Meghna Das Thakur, Qin Su, Zhenfen Chi, Yongliang Zhao, and Gregory D Longmore. A multifunctional lentiviral-based gene knockdown with concurrent rescue that controls for off-target effects of rnai. *Genomics, proteomics & bioinformatics*, 8(4):238–245, 2010.

[98] Peter Friedl and Katarina Wolf. Plasticity of cell migration: a multiscale tuning model. *The Journal of cell biology*, pages jcb–200909003, 2009.

[99] Hyun Jung Lee, Miguel F Diaz, Katherine M Price, Joyce A Ozuna, Songlin Zhang, Eva M Sevick-Muraca, John P Hagan, and Pamela L Wenzel. Fluid shear stress activates yap1 to promote cancer cell motility. *Nature Communications*, 8, 2017.